A BIOLOGICAL CONTEXT FOR THETA-FREQUENCY NEURONAL RESONANCE: A COMPARATIVE STUDY BETWEEN CORTICAL AMYGDALA AND HIPPOCAMPAL NEURONS

Tesis

Entregada A La
Universidad De Chile
En Cumplimiento Parcial De Los Requisitos
Para Optar Al Grado De

Doctor en Ciencias con Mención en Biología Molecular, Celular Y Neurociencias

Facultad De Ciencias

Por

Jorge Alejandro Vera Buschmann

Octubre, 2014

Director de Tesis:

Dra. Magdalena Sanhueza Tohá

FACULTAD DE CIENCIAS

UNIVERSIDAD DE CHILE

INFORME DE APROBACION

TESIS DE DOCTORADO

Se informa a la Escuela de Postgrado de la Facultad de Ciencias que la Tesis de Doctorado presentada por el candidato

Jorge Alejandro Vera Buschmann

Ha sido aprobada por la comisión de Evaluación de la tesis como requisito para optar al grado de Doctor en Ciencias con mención en Biología Molecular Celular y Neurociencias, en el examen de Defensa Privada de Tesis rendido el día 23 de Octubre de 2014.

Director de Tesis:

Dra. Magdalena Sanhueza .....

Comisión de Evaluación de la Tesis

Dr. Juan Carlos Letelier .....

Dra. Cecilia Vergara .....

Dr. Pedro Maldonado .....

Dr. Fernando Torrealba .....

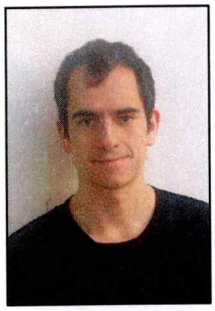

Nací en Santiago el 31 de diciembre de 1982, el año 1990 nos mudamos a Chillán. Es bueno crecer en provincia. Volvimos a Santiago el año 1999. Entre los años 2002 y 2014, después de doce años he obtenido el pregrado, Magister y Doctorado en la Facultad de ciencias de la Universidad de Chile. Quizás ya la conozco demasiado, pero aún me quedaré 3 años más.

Acknowledgments

Thanks to all the people involved in this investigation: Ulises Pereira, Bryan Reynaert, Alfonzo Deichler, Macarena Faunes, Daniela Astudillo, Pablo Lois and Professors Jorge Mpodozis, Julio Alcayaga and Juan Bacigalupo.

Special thanks to Professors of the committee who reviewed this thesis: Dr. Cecilia Vergara, Dr. Pedro Maldonado, Dr. Fernando Torrealba and Dr. Juan Carlos Letelier.

Thanks to all the partners I have met during this long staying in the laboratory of Cell Physiology.

Last but not least, thanks to my dear thesis Director, and now colleague, Dr. Magdalena Sanhueza.

Index of contents

Title ..... *I*
Dedication ..... *II*
Acknowledgments ..... *III*
Index of contents ..... *IV*
Index of figures ..... *VI*
List of abbreviations ..... *VIII*
Abstract ..... *IX*
Chapter 1. INTRODUCTION *1*
1.1 Neurocentric view of brain activity *1*
1.2 Neuronal resonance and the theta-frequency range *4*
1.3 Cell types displaying theta resonance *6*
1.4 Relating theta-neuronal resonance with brain activity at theta range *7*
1.5 Proposed functional significance of neuronal resonance: translation of sub threshold frequency preference to the spiking regime *8*
1.6 Neuronal resonance in the context of an intact brain I: the active network state and the attenuation of intrinsic frequency preference *9*
1.7 Neuronal resonance in the context of an intact brain II: the active neuron state and the modulation of intrinsic frequency preference *10*
1.8 Resonant neurons in the cortical amygdala: a privileged model to study resonance implications *10*
1.9 Thesis proposal *12*
1.10 Hypothesis *14*
1.11 Objectives *15*
Chapter 2. METHODS *16*
2.1 Ethical approval *16*
2.2 Slice preparation *16*
2.3 Electrophysiological recordings *17*
2.4 Recording solutions *17*
2.5 Liquid junction potentials *18*
2.6 ZAP stimulation and analysis *18*
2.7 Quantification of resonance *10*
2.8 Firing probability measurements *21*
2.9 Dynamic clamp *21*
2.10 Changes in R_{in} *21*
2.11 Models for I_{NaP} and I_M *22*
2.12 High conductance state *23*
2.13 Linearized RLC circuit *24*
2.14 Characterization of neuronal morphology *25*
2.15 Neural tracing experiments *25*
2.16 Drugs *25*
Chapter 3. RESULTS *27*
3.1 Cellular mechanism for subthreshold resonance and selective firing in layer II neurons from the anterior nucleus of the cortical amygdala *28*
3.1.1 Abstract *28*
3.1.2 Introduction *30*
3.1.3 Results *34*
3.1.4 Discussion *57*
3.1.5 References *68*

3.2 Electrophysiological and morphological characterization of resonant and non-resonant neurons from layer II of the anterior nucleus of the cortical amygdala 73
3.2.1 Abstract 73
3.2.2 Introduction 75
3.2.3 Results 78
3.2.4 Discussion 115
3.2.5 References 118
3.3 Mechanism for perithreshold resonance in pyramidal neurons from CA1 hippocampus 122
3.3.1 Abstract 122
3.3.2 Introduction 124
3.3.3 Results 128
3.3.4 Discussion 151
3.3.5 References 155
3.4 Neuronal resonance in a network context: Impact of the high conductance state 159
3.4.1 Abstract 159
3.4.2 Introduction 162
3.4.3 Results 166
3.4.4 Discussion 182
3.4.5 References 185
Chapter 4. DISCUSSION ***188***
4.1 How general are properties of theta-resonant neurons? 189
4.2 Resonant neurons translate their frequency preference to spiking regime using different mechanisms 191
4.3 The impact of theta-resonance under in vivo-like conditions and the effect of R_{in} 192
Chapter 5. CONCLUSION ***195***
References 196
Supplementary figures 201

Index of figures

Figure 1. Resonant and non-resonant layer II ACo neurons..... 35
Figure 2. Q value and peak frequency distributions confirm the existence of resonant and non-resonant subpopulations of neurons..... 39
Figure 3. *INaP* plays a critical amplifying role in resonance but is not involved in band- pass filtering..... 42
Figure 4. Resonance blockade by external Cs^+..... 45
Figure 5. Subthreshold resonance depends on I_h in the whole subthreshold range; I_M also contributes in a subset of neurons at depolarized potentials..... 47
Figure 6. Voltage-clamp experiments confirmed the presence of I_h and I_{NaP}. 52
Figure 7. Resonant neurons from ACo translate their subthreshold frequency preference to spiking regime..... 55
Figure 8. Characterization of subthreshold frequency preference in a subset of ACo neurons..... 79
Figure 9. Characterization of firing frequency curve and spike threshold for resonant and non-resonant neurons..... 84
Figure 10. Relating subthreshold frequency preference to firing pattern..... 88
Figure 11. Medium duration after-hyperpolarization (AHPm) and resonance in ACo layer II neurons..... 91
Figure 12. Cytoarchitecture of the anterior cortical amygdala nucleous (ACo) separating resonant and non-resonant neurons..... 96
Figure 13. Confirming anatomical projections from the olfactory bulb. Axons from the olfactory bulb project to the anterior cortical amygdala..... 100
Figure 14. Characterization of spontaneous synaptic activity of layer II ACo neurons..... 103
Figure 15. Characterization of evoked synaptic activity of layer II ACo neurons..... 106
Figure 16. Characterization of evoked synaptic responses of ACo neurons under theta rhythmic stimulation of layer Ia..... 109
Figure 17. Characterization of evoked synaptic responses of ACo neurons under theta-gamma rhythmic stimulation of layer Ia..... 112
Figure 18. Differential response of ACo neurons to theta or theta-gamma stimulation..... 114
Figure 19. CA1 pyramidal neurons display two different behaviors under perithreshold oscillatory stimulation..... 130
Figure 20. Different perithreshold behavior of CA1 pyramidal neurons is maintained under firing regime..... 131
Figure 21. Non-resonant CA1 pyramidal neurons display M-resonance in presence of TTX. 134
Figure 22. Voltage-clamp measurement of I_{NaP} and I_M..... 137
Figure 23. Pharmacologic reduction of I_{NaP} produces a switch from non-resonant to resonant behavior in CA1 pyramidal neurons..... 142
Figure 24. Dynamic-clamp reduction of I_{NaP} or increase of I_M produces a switch from non-resonant to resonant behavior in CA1 pyramidal neurons..... 146
Figure 25. RLC circuit theory predicts a modulation of resonance by input resistance changes..... 167
Figure 26. Exploring the effect of R_{in} changes on subthreshold resonance in a hippocampal CA1 neuron..... 170
Figure 27. The virtual increase or reduction of R_{in} modulates subthreshold resonance in hippocampal CA1 neuron..... 172

Figure 28. Resonant frequency (f_R) is inversely correlated with R_{in}: comparison between different types of neurons of the rat brain..... *174*
Figure 29. The modulation of subthreshold resonance by changes in R_{in} is expressed under spiking regime in ACo neurons..... *176*
Figure 30. Resonant ACo neurons preserve their firing at preferred frequency under recreated high-conductance state. *179*
Figure S1. Blockade of Ih-resonance and spikes confirms the lack of the Im-dependent mechanism in an ACo neuron. *201*
Figure S2. CA1 pyramidal neurons show a strong I_M-dependent resonance at supra- threshold potentials in TTX..... *202*
Figure S3. Protocol for I_M recording in ACo neuron gives no XE991 sensitive currents..... *203*
Figure S4. Exploration of resonance in confirmed semilunar and pyramidal neurons from piriform cortex..... *204*

List of abbreviations

Aco	Anterior nucleous of the cortical amygdala
ACSF	Artificial cerebrospinal fluid
APV	Aminophosphonovaleric acid
CNQX	6-cyano-7-nitroquinoxaline-2,3-dione
FFT	Fast Fourier transform
f_R	Resonant frequency
G	Conductance
HCS	High conductance state
L	Inductance
lACSF	Low sodium ACSF
LJP	Liquid junction potential
MetOH	Methanol
MOB	Main olfactory bulbe
PBS	Phosphate buffer solution
PC	Piriform cortex
PFA	Paraformaldehyde
PTX	Picrotoxin
Q	Resonance strength
Q'	Apparent Q
RC	Resistance and capacitor
R_{in}	Membrane input resistance
RLC	Resistance, Inductor and capacitance
RTXI	Real time experiments interfase
TBS	Tris buffer solution
TTX	Tetrodotoxin
ZAP	Impedance amplitude profile
Z_{max}	Peak impedance

Abstract

Neurons from different memory-related mammalian brain regions display intrinsic maximal subthreshold voltage responses to oscillatory stimulation at theta frequencies (4-12 Hz; theta resonance). This may contribute to tune and stabilize network oscillatory activity. However, the drop in input resistance (R_{in}) produced by synaptic bombardment in active networks predicts a loss of resonance impact on neuronal processing. To investigate whether resonance drives rhythmic spiking in active networks we performed a comparative study of two resonant neuron populations with different R_{in}, pyramidal neuron from CA1 hippocampus (CA1P, ~60 MΩ) and neurons from the anterior nucleous of the cortical amygdala (ACoN, ~160 MΩ) using rat brain slices, whole-cell recordings and dynamic clamp. A hyperpolarization-activated cationic current (I_h) contributed to subthreshold resonance in both neuronal groups. Favored by the high R_{in}, I_h also filtered perithreshold voltage oscillations in ACoN, thus allowing the translation of resonance to spiking regimes even under recreated synaptic bombardment. In turn, CA1P neurons displayed a tunable mechanism for resonance translation to spiking based on relative levels of a muscarine-sensitive potassium current (I_M) and a persistent sodium current (I_{NaP}). Notably, we confirmed the prediction of RLC-filter theory that changes in R_{in} due to synaptic bombardment modulate resonance frequency and strength. CA1P have five-fold more I_{NaP} than ACoN, increasing perithreshold impedance and thus compensating the low R_{in}. Therefore, neurons with opposed R_{in} values implement different strategies to effectively translate their frequency preference to spiking regimes.

We present a novel aspect of neuronal resonance, consisting of a dynamic tunable mechanism for intrinsic frequency preference that depends on the level of network activity.

Chapter 1

INTRODUCTION

1.1 Neurocentric view of brain activity

Our conception of the world corresponds to an internal representation that emerges as a consequence of brain activity influenced by sensory inputs (von der Malsburg et al., 2010; Sporns, 2011). Brain activity is carried out by billions of neurons that are continuously performing a fundamental process consisting on receiving stimuli, processing them in a complex space- and time-dependent manner. Subsequently, using an electric language based on the firing of action potentials, communicating the processed signals to downstream neurons (Sporns, 2011). This essential property of neurons which relies in their excitable nature (Mccormick, 1998), generates complex patterns of activity as cells interact among them in local circuits and also in the entire brain. This activity, in interplay with peripheral and autonomous nervous system ultimately generate the animal behavior (Buzsáki, 2006; Sporns, 2011). This fascinating process demands a very precise temporal coordination of neuronal activity across several spatial scales, ranging from local circuits (microns to millimeters) to the distance separating different brain regions (centimeters) (von der Malsburg et al., 2010). This

exact timing of neuronal activity depends on the ability of neurons to transit from subthreshold to suprathreshold potentials. Despite the wealth of information regarding the mechanism of action potential generation and propagation and also about synaptic transmission, little is known on the intrinsic excitability properties of neurons that influence whether and how they fire or not an action potential (Ratté et al., 2013); more precisely, the question that requires further attention is which is the specific dynamics of neurons when they approach perithreshold potentials (near threshold) and engage towards two complete different outcomes: remain silent or transit toward an active state generating action potentials. This step of transition is even more complex if is considered that the brain works based on oscillatory activity in frequency ranges that span from fractions to hundreds of cycles per second (Penttonen and Buzsáki, 2003). The oscillatory nature of brain activity is expressed at the neuronal level as rhythmic synaptic activity that arrives to neurons and drives subthreshold oscillations of the membrane potential in the perithreshold range (Kamondi et al., 1998; Richardson et al., 2008). Together with this oscillatory incursions towards action potential threshold, neuronal activity possesses a natural noisy component that makes even more complex the process of firing or not an action potential (Faisal et al., 2008). The understanding of the intrinsic (built-in) neuronal mechanisms involved in the control of sub- and perithreshold responses is fundamental to comprehend their contribution to brain function at both normal and pathologic conditions (Beck and Yaari, 2008; Ratté et al., 2013).

The traditional and rather simplistic view of this process of transition of neurons from resting to an active state, is that neurons receive synaptic activity and respond in one of

two different ways: as integrators, summing incoming stimuli until reaching spike threshold, or as coincidence detectors that attain spike threshold when synaptic inputs coincide in a rather short time window (Prescott et al., 2008). To unravel the way neurons process synaptic inputs and fire action potentials (also called *spikes* given the way they look at the oscilloscope) would have a tremendous implication for understanding the language that brain uses to operate, the so called neuronal code (Sejnowski, 1995). When neurons act as integrators, they respond according to the firing frequency of presynaptic neurons, thus they are well suited for a code dependent on the firing rate of neurons, called rate code (Prescott et al., 2006). On the other hand, when neurons act as coincidence detectors they respond better to synchronous synaptic inputs generating a neural code where information is conveyed by the precise timing of spikes, which is a spike-time code (Prescott et al., 2006). The actual behavior of cortical neurons lies between these two forms of neuronal processing, and remarkably, neurons can switch dynamically between integrators or coincidence detectors according to the level of synaptic inputs or modification of their intrinsic properties (Ratté et al., 2013). This makes it possible that neurons multiplex both codes, transmitting information based in their firing rate and, at the same time, also codify information in the specific timing of action potentials (Ratté et al., 2013).

When the voltage response of neurons is investigated in the frequency domain instead of time domain, which means evaluating their voltage response as a function of the frequency of stimulation, another classification of neurons in two types emerges: resonators and non-resonators, with resonant neurons favoring oscillatory activity at

specific frequency ranges, whereas non-resonant neurons do not (Hutcheon and Yarom, 2000).

1.2 Neuronal resonance and the theta-frequency range

When neurons are stimulated at subthreshold potentials with an oscillatory current of increasing frequency, most cells respond with decreasing amplitude as stimulation frequency increases (Hutcheon and Yarom, 2000). This is produced because for fast oscillations the cell membrane, which acts as a capacitor, does not have enough time to be charged, resulting in a filtering of high-frequency oscillations. The common way to analyze frequency dependence of neurons is by measuring their impedance profile, which is the ratio of the fast Fourier transform of the membrane potential (the output) to the injected current (the input), which represents a generalization of the input resistance of the neurons for an oscillatory regime and is a function of the frequency of stimulation. The impedance profile of a non-resonant neuron decays monotonically from their maximum value near 0 Hz as frequency increases (Hutcheon and Yarom, 2000).

A particular group of neurons classified as resonant, instead of filtering only high frequencies, they also filter low frequency oscillations, thus generating a maximal voltage response in between both filtered regions (Hutcheon and Yarom, 2000; Izhikevich, 2002). Theta-resonant neurons are those neurons that have a frequency preference for oscillatory stimulation in the theta rage (3-10 Hz). The attenuation of slow oscillations is produced by the presence of at least one voltage-sensitive current (called resonant current) that has the property of activating towards voltage ranges in the opposite direction to the current reversal potential. This develops a membrane current

that moves the potential towards values that gate its deactivation, generating a feedback loop of activation/deactivation that attenuates voltages oscillations slower than the activation time constant of the particular current (Hutcheon and Yarom, 2000).

The mechanism of resonance is easier to explain using as example the hyperpolarization-activated cationic current, I_h (Robinson and Siegelbaum, 2003). This current has been widely identified as the mechanism of theta-resonance in many mammalian neurons (Hu et al., 2002; Ulrich, 2002; Erchova et al., 2004; Wang et al., 2006). This is a mixed K^+ and Na^+ current, is mostly closed at resting potential and activates with voltages more hyperpolarized than -70 mV (Robinson and Siegelbaum, 2003). Given its voltage range of activation, I_h corresponds to net inward current that reverses near -40 mV, thus having a depolarizing effect. When neurons are hyperpolarized below -70 mV, I_h is activated and moves back the membrane voltage, depolarizing the cell towards its reversal potential with the consequent current deactivation (the feedback loop) (Hutcheon and Yarom, 2000). Given that the activation time constant (τ) of I_h is of the order of tens of milliseconds, voltage oscillations at frequencies below 8-10 Hz (with period below $1/2\pi\tau$) will allow I_h activation or deactivation with the consequent attenuation in the response (Hutcheon and Yarom, 2000). Another current described as producing theta-resonance is the muscarine-sensitive K^+ current, I_M (Hu et al., 2002). Its mechanism of action is similar to I_h, with the difference that it is a hyperpolarizing outward K^+ current, and its voltage sensitivity produces it activation at potentials above -60 mV, in opposed direction than I_h (Brown, 1988; Shah et al., 2002).

According to the activation time constant of the resonant current involved, neurons may have a peak voltage response at different frequency ranges, including theta (4-12 Hz) and gamma (30-60 Hz) ranges (Hutcheon and Yarom, 2000).

In addition to frequency preference, resonant neurons display other remarkable characteristics. In whole cell experiments as well as when neuronal membrane is modeled by an equivalent RC circuit, it is obtained that under oscillatory stimulation the voltage response always follows the oscillatory activity with a phase lag that increases with frequency. It turns out that resonant neurons have a lower phase shift compared to non-resonant neurons, and even can have zero or positive phase shift in the lower frequency range (Narayanan and Johnston, 2008). This means that resonant neurons may follow oscillatory inputs with less lag than non-resonant neurons, thus favoring a faster and tightly coordinated oscillatory activity at network level.

1.3 Cell types displaying theta-resonance

Despite the high neuronal diversity presented in the mammalian brain it is possible to group neurons in specific cell types which are characteristic of each brain region (Contreras, 2004). In turn, each brain region contains a subset of particular cell types that accomplish specific functions in the neuronal network (Klausberger and Somogyi, 2008). The definition of a cell type is given by a rather arbitrary set of features like cellular morphology, electrophysiological properties, neuropeptide profile, among others (Spruston and McBain, 2007). Theta resonance has been described in two well-characterized cell types, pyramidal neurons from CA1 hippocampus (Hu et al., 2002), and layer II stellate cells of entorhinal cortex (Erchova et al., 2004). Each of these cell

types has a characteristic set of intrinsic properties that sets their input-output curve and action potential threshold, an also display a representative synaptic connectivity (Spruston and McBain, 2007; Canto et al., 2008). In terms of morphology pyramidal neurons from CA1 and stellate cells are very similar inside each group and share other similarities between groups. Both cell types have the soma and dendritic projections in the same cortical layers into their respective regions. The shape and extension of their dendritic projections is very similar within each type, with stellate cells displaying a denser spiny dendritic branch (Klink and Alonso, 1997), while CA1 neurons have a more pronounced apical dendrite that project secondary and tertiary dendrites in a conic shape (Spruston and McBain, 2007). They share many characteristics that allow an easy recognition of them. Certainly, both of these resonant neuronal types are intertwined with several other neuronal types in their respective brain regions, CA1 pyramidal neurons share their layer with more than 25 different types of interneurons (Klausberger and Somogyi, 2008), while stellate neurons coexist with pyramidal neurons and interneurons (Canto, Wouterlood, & Witter, 2008).

1.4 Relating theta-neuronal resonance with brain activity at theta range

The importance of the fact that theta-resonance is expressed in specific cell types comes from the possible relationship that may exist at the cellular level between structure and function (Somogyi and Klausberger, 2005). It is particularly interesting that both the hippocampus and entorhinal cortex are part of the parahippocampal formation where multisensory information is processed allowing the construction of a map of the external world (Fyhn et al., 2004; Buzsáki and Moser, 2013). This brain region displays a strong

theta activity during several behavioral activities that require its function like navigation or memory-related tasks (Buzsáki, 2005; Hasselmo, 2005; Buzsáki and Moser, 2013). Most important, both resonant cell types have been characterized as key neuronal correlates for the construction of the internal map, with CA1 pyramidal neurons encoding a specific location in the external world and are thus called "place cells" (O'Keefe and Recce, 1993), and stellate cells coding for a spatial grid pattern, constituting the "grid cells" (Hafting et al., 2005).

The emergence of place and grid cells is a process related to theta-frequency activity, however it is not clear whether intrinsic theta-resonance contributes to the generation of that behavioral correlate, or if theta activity result only from synaptic activity or both.

1.5 Proposed functional significance of neuronal resonance: translation of sub threshold frequency preference to the spiking regime.

As neuronal resonance is a subthreshold phenomenon, filtered voltage oscillations need to interact with the mechanism of action potential generation in order to translate the frequency preference to a spiking regime and propagate electrical activity in a selective way.

In resonant neurons, subthreshold frequency preference may selectively translate to spiking patterns the incoming oscillatory inputs at the resonance frequency (Hutcheon and Yarom, 2000; Izhikevich, 2002). Resonance could thus constitute a band-pass filter mechanism for transmitting repetitive activity in a limited frequency range, which may critically contribute to orchestrate neuronal network rhythms (Llinás, 1988; Hutcheon and Yarom, 2000). Neuronal resonance in the theta-frequency range may participate in

the generation of the network theta waves observed during memory formation (Lisman, 2005), suggesting an involvement of this intrinsic property in learning. Accordingly, during network theta activity the induction of synaptic plasticity is facilitated (Huerta and Lisman, 1995)

1.6 Neuronal resonance in the context of an intact brain I: the active network state and the attenuation of intrinsic frequency preference.

It is speculated that resonance may contribute to tune and to stabilize oscillatory activity in neuronal networks (Hutcheon and Yarom, 2000), however, the context that resonant neurons face in an active network challenges this view. In active neuronal networks membrane input resistance, R_{in}, varies in a wide range depending on synaptic bombardment, showing up to an 80% decrease from its value in a silent network (Destexhe et al., 2003). This active network state has two implications for neuronal resonance. The first is that the decrease in R_{in} implies a general reduction of the impedance profile accompanied by lower resonance strength and the corresponding detriment of frequency preference. The second is the noise of the membrane potential produced by the bombardment of uncorrelated synaptic inputs (Destexhe et al., 2003). When a neuron is oscillating just below threshold the stochastic nature of noise may favor the generation of action potentials at frequencies away from the range of preference, producing an impairment of frequency selectivity (Ermentrout et al., 2008). Obviously, these considerations favor the impact of resonance when resonant neurons have a high R_{in}.

1.7 Neuronal resonance in the context of an intact brain II: the active network state and the modulation of intrinsic frequency preference.

On the other side, using an RLC (resistance, impedance, capacitance) equivalent circuit, which mimics the resonant behavior of neurons, it is possible to predict that not only resonance strength but also resonance frequency would depend on R_{in}. Since R_{in} decreases proportionally with increasing levels of synaptic bombardment, a prediction of the model is that the resonance frequency and strength will change in opposite directions after modifications in synaptic activity. Therefore, this may constitute a mechanism of modulation of intrinsic resonance by the level of network activity. Notably, the higher the R_{in} of the resonant neuron, the wider the range for modulation it will have.

1.8 Resonant neurons in the cortical amygdala: a privileged model to study resonance implications.

Previous work of the laboratory described a new group of theta resonant neurons that display a high R_{in}, with an average of 160 MΩ, near three times the value for hippocampal pyramidal cells (~60 MΩ) (PhD thesis M. Pezzoli). These neurons are part of the layer II of the anterior cortical amygdala nucleus (ACo) and represent at least one third of the whole neuronal population in this layer. The ACo is part of the olfactory circuit and given its direct connection with the olfactory bulb, ACo functions as a gate for olfactory activity propagation to the basolateral and centromedial amygdala, probably contributing to the processing of olfactory stimuli of biological relevance.

The mammalian olfactory circuit is characterized by a pronounced theta-frequency activity, which is behaviorally driven by sniffing (Kepecs et al., 2006). At

rest, sniffing frequency is around 2-4 Hz, while during exploration and odor recognition tasks, it increases to around 6-12 Hz, thus spanning all the theta range (Kepecs et al., 2007; Wesson et al., 2008; Doucette et al., 2011). Sniffing activity evokes phase-locked spiking in principal cells of the MOB and PC (Macrides and Chorover, 1972; Wilson, 2001; Cang and Isaacson, 2003) and correlated rhythmic activity in the hippocampus, a correlation that increases when the animal is evaluating the biological relevance of the stimulus (Macrides et al., 1982). In this context, it becomes relevant to characterize resonance in neurons from the olfactory amygdala, a possible locus of olfactory-related emotional learning.

Several studies have shown that the olfactory circuit operates based on oscillatory activity in the theta range (4-12 Hz), which is driven by the exploratory behavior of sniffing. Despite a lack of whole cell *in vivo* recording of ACo neurons, recordings from other olfactory structures like olfactory bulb and piriform cortex show that synaptic activity follows sniffing rhythmic activity. This evidence allows to propose that resonant neurons from ACo are selectively driven by rhythmic synaptic activity around their resonance frequency. Moreover, taking into account their high R_{in}, ACo neurons appear as a privileged model to evaluate the impact of the active network state on theta-resonance rhythmic processing.

Despite a robust description of subthreshold voltage response of ACo neurons, when this thesis work started it was not clearly understood what was the ionic current underlying theta-resonance and also it was ignored whether this resonant neurons belongs to a defined cell type as is the case for CA1 pyramidal neurons and stellate cells from entorhinal cortex (explained above).

1.9 Thesis proposal

The existence of theta-resonant neurons is very attractive as an intrinsic mechanism for neural processing considering that one of the most prominent characteristics of brain activity is their oscillatory nature, with particularly high power at theta and gamma frequency ranges (Hutcheon and Yarom, 2000; Buzsáki, 2006). The general property of resonant neurons is that, when receiving oscillatory stimuli, they respond with an increased subthreshold voltage response when stimulated at their frequency of preference (Hutcheon and Yarom, 2000). It is speculated that if oscillations are large enough to reach spike threshold they will translate their preferred frequency to a spiking regime, thus firing action potentials with a higher probability when stimulated at the preferred frequency (Hutcheon and Yarom, 2000; Hu et al., 2009). Computational models show that resonant neurons stabilize oscillatory activity at network levels (Buzsáki, 2006). However, until now there is a complete lack of detailed empirical evidence regarding a possible contribution of neuronal resonance to a differential perithreshold processing of oscillatory inputs, nor on a potential influence of neuronal resonance to oscillatory network activity. While the functional contribution of resonance has been usually assumed, it is not known if resonant neurons effectively translate their subthreshold frequency preference to a spiking regime. It is also ignored whether resonant neurons have the synaptic machinery to support incoming rhythmic inputs without suffering synaptic filtering or distortions due to facilitation or depression (Creager et al., 1980; Debanne et al., 1996) that may occlude the expression of frequency preference generated by intrinsic resonance. The main reason for this uncertainty is a methodological limitation to evaluate how resonant neurons process

rhythmic oscillatory inputs *in vivo*, thus hindering a more realistic evaluation of neuronal resonance in brain functioning.

rhythmic oscillatory inputs *in vivo*, thus hindering a more realistic evaluation of neuronal resonance in brain functioning.

1.10 Hypothesis

Subthreshold neuronal resonance constitutes a mechanism of intrinsic frequency preference that is translated to spiking regime and is preserved under *in vivo*-like conditions, thus shaping the activity of resonant neurons.

1.11 Objectives

General:

To investigate if resonant neurons translate their subthreshold frequency preference to a spiking regime in brain slices, determining the involved mechanisms, and to evaluate the impact of theta-resonance when *in vivo* conditions are mimicked.

Specific:

1. To characterize the electrophysiological and morphological properties of ACo neurons and their mechanism of resonance.
2. To investigate if subthreshold frequency preference is translated to the spiking regime in ACo and CA1 neurons and to determine the underlying mechanism.
3. To study the relationship between R_{in} and frequency preference in conditions that simulate the active network state.
4. To determine if the translation of resonance to spiking is preserved in the presence of realistic synaptic noise.

Chapter 2

METHODS

2.1 Ethical approval

Animal care and experimental procedures were approved by the Bio-Ethical Committee of the Faculty of Sciences, University of Chile, according to the ethical rules of the Biosafety Policy Manual of the National Fund for Scientific and Technological Development (FONDECYT).

2.2 Slice preparation

Male Sprague Dawley rats from 18 to 30 day-old. The animals were deeply anesthetized with ether and sacrificed by decapitation. The brain was rapidly removed and transferred to an ice-cold dissection solution containing (in mM): 206 sucrose, 2.8 KCl, 1 $MgCl_2$, 2 $MgSO_4$, 1 $CaCl_2$, 26 $NaHCO_3$, 1.125 NaH_2PO_4, 10 glucose and 0.4 ascorbic acid (equilibrated with 95% O_2 and 5% CO_2), pH 7.3. Coronal slices (400 μm) containing the ACo (Bregma -2.2 to -3.3; Paxinos et al., 1999) or hippocampus were obtained with a vibratome (Vibratome Sectioning System 102, Pelco). Slices were placed in a holding

chamber with standard artificial cerebro-spinal fluid (ACSF) and were left to recover during at least 1 h at 30°C before using them for recordings.

2.3 Electrophysiological recordings

Whole cell patch-clamp recordings were conducted under visual guidance by an upright microscope equipped with oblique infrared optics (Nikon Eclipse E600FN) equipped with DIC optic. Electrodes (3.5–4.5 MΩ) were fabricated from borosilicate glass capillary tubing (0.8 - 1.10 x 100 mm; Kimble Glass Inc) using a horizontal puller (Flaming/Brown P- 97, Sutter Instrument Co). Current-clamp and voltage-clamp recordings were made with an EPC-10 patch-clamp amplifier (Heka, Heidelberg, Germany), data were filtered at 16 kHz and acquired at 1 or 25 kHz using the Heka Pulse software. All experiment, with the exception of those where synapses activity was recorded, were performed in presence of 10 μM CNQX and 100 μM PTX to block AMPA-R and GABAa-R mediated currents. In a fraction of experiments 100 μM APV was added.

2.4 Recording solutions (in mM):

Artificial cerebro-spinal solution (ACSF): 124 NaCl, 2.8 KCl, 1.25 NaH_2PO_4, 26 $NaHCO_3$, 10 Glucose, 2 $MgCl_2$, 2 $CaCl_2$ and 0.4 ascorbic acid (equilibrated with 95% O_2 and 5% CO_2), pH 7.3 and 285-295 mOsm.

Low sodium artificial cerebro-spinal solution (lACSF): 38 NaCl, 80 NMDG, 80 HCl, 2.8 KCl, 1.25 NaH_2PO_4, 26 $NaHCO_3$, 10 Glucose, 2 $MgCl_2$, 2 $CaCl_2$ and 0.4 ascorbic acid (equilibrated with 95% O_2 and 5% CO_2), pH 7.3 and 285-295 mOsm.

Internal pipette solution was based in previous works reporting stability of recorded parameters (Xu et al., 2005; Kaczorowski et al., 2011): 123 K-Gluconate, 10 KCl, 4 Glucose, 1 EGTA, 10 HEPES, 2 Na_2ATP, 0.2 Na_3GTP, 10 phosphocreatine, 1 $MgCl_2$, 0.1 $CaCl_2$ and 0.1 % biocytine, pH 7.35 and 285-290 mOsm.

2.5 Liquid junction potential (LJP)

We measured the LJP between pipette solution and ACSF (~13 mV) and lACSF (~17.5 mV) according to the procedure described by Erwin Neher (Neher, 1992) and both were corrected during offline analyses.

2.6 ZAP stimulation and analysis

Voltage responses to an intracellularly injected pseudo-sinusoidal current of constant amplitude (10 pA) and linearly decreasing or increasing frequencies (ZAP stimuli; frequency interval: 0 - 15 or 20 Hz, 10 s duration) were recorded in current clamp conditions. The full stimulation protocol included a complete screening of the physiologically relevant subthreshold membrane potentials. For this, ZAP stimuli were superposed to a series of incremental 10 pA current steps of 11 s duration, from about – 50 pA until action potentials were triggered. In experiments with blockers of voltage-dependent channels the amplitude of ZAP stimuli was adjusted to maintain a peak to peak subthreshold voltage response comparable to the control condition (5-10 mV) and to favor the evaluation of perithreshold resonance in the absence of spikes. In all experiment the protocol was repeated 8 to 10 times in every neuron, for each condition.

The output isopotential subthreshold waves were averaged to proceed with the impedance analysis.

The impedance frequency profile (*Z(f)*) was obtained from the ratio of Fast Fourier Transforms (FFT) of output (voltage) and input (current) waves (*Z(f)=FFT[V(t)]/FFT[I(t)]*), using Igor Pro software version 6.3 (Wavemetrics, Inc., Lake Oswego, OR). The impedance is a complex quantity (*Z(f) = Z, Real + iZ, Imaginary*), where the real part (*Z, Real*) is the resistance and the imaginary part (*Z, Imaginary*), the reactance. For each given frequency, the complex impedance can be plotted as a vector whose magnitude and phase (*Φ(f)*; angle with the real axis) are, respectively given by the following expressions:

$$|Z(f)| = \sqrt{(Z,\mathrm{Re}al)^2 + (Z,\mathrm{Im}aginary)^2}$$

$$\Phi\ (f) = \tan^{-1}\left(\frac{Z,\mathrm{Im}aginary}{Z,\mathrm{Re}al}\right)$$

Throughout the text the term *impedance* will be used to refer to the magnitude of the impedance vector, unless otherwise stated. The impedance phase corresponds to the phase shift of the voltage wave relative to the current wave. Frequencies below 0.5 Hz were not plotted in the graphs for impedance and phase profiles, to avoid low frequency distortions. In some pharmacological experiments, the impedance profiles were normalized to the value at the maximal frequency, to allow easier discrimination of changes in curve shape from overall shifts that may occur after manipulations that modify membrane resistance. Off-line analyses and graphs were performed with Igor

Pro. Average results are expressed as mean ± SE. Student's-t test set at a level $p < 0.05$ was used as criterion of significance.

2.7 Quantification of resonance

Resonance is defined as the band-pass filter property of the impedance profile (Hutcheon and Yarom, 2000). The strength of resonance is usually quantified as the ratio between the maximal impedance (i.e. the impedance at the resonance frequency, $|Z(f_{res})|$) and the impedance at the lowest frequency ($|Z(0.5)|$). This ratio is called the Q factor or value and indicates the sharpness of the impedance curve around the resonance frequency. For a more precise determination of Q, the experimental data were fitted with a theoretical curve for the impedance (Erchova et al., 2004), obtained from the resolution of a phenomenological linearized membrane circuit model for resonance, in which the band-pass filter properties result from the addition of an inductive (L) branch to the electric circuit that models the passive membrane properties (RC circuit, consisting of a resistance and a capacitor in parallel, reproducing the low-pass membrane filtering) (Koch, 1984; Hutcheon and Yarom, 2000). The impedance of an RLC circuit has band-pass (resonating) properties and a characteristic phase profile that is different from the RC case (see examples and discussion below). The inductive branch that generates the high-pass filter component results from the influence of voltage-dependent currents called inductive currents. Here we chose $Q \geq 1.10$ as a quantitative criterion to differentiate resonant from non-resonant cells, thus the maximal impedance should be at least 10% higher than $|Z(0.5)|$. We set this criterion to guarantee that even

for noisy impedance profiles, the average of 10 points around the peak were statistically different from the average of the same number of points at the lowest frequency. For simplicity, this was considered as a general cutoff criterion for resonance in this paper and its accuracy is discussed in Results.

2.8 Firing probability measurements

Oscillatory voltage responses were quantized according to the period of each oscillation and the number of action potentials fired at a given frequency was divided by the number of periods.

2.9 Dynamic Clamp

For dynamic-clamp experiments, the current-clamp amplifier was driven by an analog signal from a dual core desktop computer running the Real-Time Linux Dynamic Clamp called Real-Time Experimental Interface, RTXI (Dorval et al., 2001; Bettencourt et al., 2008) using an update frequency of 25 KHz.

2.10 Changes in R_{in}

Increases (+G) or reduction (-G) in conductance were introduced via dynamic clamp using a leak current according to equation:

$$I_{leak} = G(V - E_{leak})$$

where V is the online recorded membrane potential, E_{leak} represent the reversal potential for the leak conductance and was set to -65 mV (Fernandez and White, 2010).

2.11 Models for I_{NaP} and I_M

Dynamic current used to decrease endogenous I_{NaP} or increase I_M were introduced via dynamic clamp using the following set of equations:

$$I_{NaP} = g_{NaP} w (V - E_{Na})$$

$$I_M = g_M r (V - E_K)$$

were g_{NaP} and g_M are the maximal conductances of the corresponding current, V is de online measured membrane potential, w and r are the state variables and E_{Na} and E_K are the reversal potential for Na^+ and K^+, respectively (Richardson et al., 2008). The dynamic of the state variables w and r were modeled according the equation (Hodgkin and Huxley, 1952):

$$\frac{dx_i}{dt} = \frac{x_{i\infty}(V) - x_i}{\tau_{xi}(V)}$$

were $x_{i\infty}$ are the steady-state values of x_i, and τ_{xi}, are the corresponding time constants.

The voltage dependence of the state variables at equilibrium was given by the equations:

$$w_\infty = \frac{1}{1 + e^{-(V+V_{0.5})/5}}$$

$$r_\infty = \frac{1}{1 + e^{(V+35)/10}}$$

were V is the online recorded membrane potential and $V_{0.5}$ is the potential for half activation of I_{NaP}. Here we set $V_{0.5}$ as -52 mV according to our voltage-clamp experiments.

The time constant for I_{NaP}, τ_{NaP} was set at 1 ms according to Vervaeke et al. (Vervaeke et al., 2006) and for I_M was modeled according to:

$$\tau_M = \frac{1000}{3.3(e^{(V+35)/40} + e^{-(V+35)/20})}$$

were V is the online recorded membrane potential.

2.12 High Conductance State

The high conductance was implemented as a point-conductance model in order to approximate synaptic background activity as described by Alain Destexhe et al. (Destexhe et al., 2001). The synaptic current, I_{syn}, was modeled as the sum of two independent conductances:

$$I_{Syn} = g_e(t)(V - E_e) + g_i(t)(V - E_i)$$

where $g_e(t)$ and $g_i(t)$ are time-dependent excitatory and inhibitory conductances, respectively; $E_e = 0$ mV and $E_i = -75$ mV are their respective reversal potentials. The conductances $g_e(t)$ and $g_i(t)$ were described by a one-variable stochastic process similar to the Ornstein-Uhlenbeck process:

$$\frac{dg_e(t)}{dt} = -\frac{1}{\tau_e}[g_e(t) - g_{e0}] + \sqrt{D_e}\chi_1(t)$$

$$\frac{dg_i(t)}{dt} = -\frac{1}{\tau_i}[g_i(t) - g_{i0}] + \sqrt{D_i}\chi_2(t)$$

where g_{e0} and g_{i0} are average conductances, τ_e and τ_i are time constants, D_e and D_i are noise diffusion coefficients, $\chi_1(t)$ and $\chi_2(t)$ are Gaussian white noise of zero mean and unit standard deviation.

The numerical scheme for integration of these stochastic differential equations takes advantage of the fact that these stochastic processes are Gaussian, which leads to an exact update rule (Gillespie, 1996):

$$g_e(t+h) = g_{e0}[g_e(t) - g_{e0}] \exp(-h/\tau_e) + A_e N_1(0,1)$$

$$g_i(t+h) = g_{i0}[g_i(t) - g_{i0}] \exp(-h/\tau_i) + A_i N_2(0,1)$$

where $N_1(0,1)$ and $N_2(0,1)$ are normal random numbers (zero mean, unit standard deviation) and A_e, A_i are amplitude coefficients given by:

$$A_e = \sqrt{\frac{D_e \tau_e}{2}\left[1 - \exp\left(\frac{-2h}{\tau_e}\right)\right]}$$

$$A_i = \sqrt{\frac{D_i \tau_i}{2}\left[1 - \exp\left(\frac{-2h}{\tau_i}\right)\right]}$$

This update rule provides a stable integration procedure for Gaussian stochastic models, which guarantees that the statistical properties of the variables $g_e(t)$ and $g_i(t)$ are not dependent on the integration step h.

2.13 Linearized RLC circuit

From the RLC circuit showed in Figure 25 and according to Erchova et al. 2004 (Erchova et al., 2004) the impedance profile, $Z(f)$, and the peak frequency, f_R, are given by equations:

$$Z(f) = \frac{1}{C}\sqrt{\frac{(2\pi f)^2 L^2 + {R_L}^2}{\left[\frac{L}{RC} + R_L\right]^2 (2\pi f)^2 + \left[\frac{1}{C}\left(1 + \frac{R_L}{R}\right) - (2\pi f)^2 L\right]^2}}$$

$$f_R = \frac{1}{2\pi}\sqrt{\left[\frac{1}{C^2 L^2} + \frac{2R_L}{CL^2}\left(\frac{R_L}{L} + \frac{1}{RC}\right)\right]^{\frac{1}{2}} - \frac{{R_L}^2}{L^2}}$$

were C is the conductance, R the resistance of the capacitive branch, L the inductor and R_L the resistance of the inductive branch.

2.14 Characterization of neuronal morphology

Recorded neurons were labeled with 0.1% biocytin in the pipette solutions. After recording slices were fixed overnight at 4°C in 4% PFA in PBS, and stored in PBS at 4°C up to 2 weeks. To reveal cell morphology slices were incubated in bleaching solution (TBS, 10% MetOH, 6% H_2O_2, 10 mins) and then in permeabilization solution (TBS, triton 1%, 1 hr). After permeabilization slices were incubated overnight at 4°C in solution AB of VECTASTAIN ABC system (www.vectorlabs.com) to further reveal neuronal morphology adding one drop of diaminobenzoic acid (DAB).

2.15 Neural tracing experiments

The rat was anesthetized with an initial dose of Ketamine (50 mg / kg IM) and Xylazine (10 mg / Kg IM). During operation the sedation was maintained by administering isoflurane gas (1%). Once anesthetized animal was mounted in a stereotaxic and an incision was made to expose the bregma and the region above the OB. We then followed stereotaxic coordinates (Paxinos & Watson, 2009) and did a craniotomy to expose the OB and cortex immediately dorsal to the OB. Once exposed the brain we did a neural tracer injection of Phaseolus Vulgaris Leucoagglutinin (PHA-L) using a protocol for iontophoresis. A glass pipette with an opening of 20 um was loaded with the tracer, and then was positioned using a hydraulic micromanipulator. The tracer was delivered using

iontophoresis protocol that posed a positive current of 8 uA at 6-second intervals (6 s On, 6 s off) for 20 min.

After completion of the iontophoresis, the pipette was removed, the opening of the skull was sealed with bone wax and the skin over the injection site was sutured. After recovering from anesthesia there was a survival time of seven days at the animal. During this time the rat was treated with analgesics and antibiotics to prevent infection and postoperative pain.

After the survival time the animal was deeply anesthetized with an overdose of ketamine / xylazine and perfused transcardially with saline, followed by 4% PFA solution. Then the brain was sectioned on a freezing microtome and the sections obtained were processed to rebel the result of migration of the tracer into the ACo.

2.16 Drugs

Drugs were bath applied at the following final concentrations: 10 μM 6-cyano-7-nitoquinoxaline-2,3-dione (CNQX; AMPA-type glutamate receptor antagonist), 100 μM d-2-amino-5- phosphonovaleric acid (APV; NMDA-type glutamate receptor antagonist), 100 μM picrotoxin (PTX; GABA-A receptor blocker), 1 μM tetrodotoxin (TTX; voltage-dependent Na^+ channel blocker), 10 μM XE991 (KCNQ channel blocker), 4.0 mM CsCl. 60 μM Phenytoin (I_{NaP} blocker). Drugs were obtained from Sigma, except for XE991 and ZD7288, purchased to Tocris, and TTX, that was obtained from Alomone Labs.

Chapter 3

RESULTS

This section is organized according to main results obtained. Based on published or redacted manuscripts, the results were grouped in four subsections, each of them covering in depth one or more specific aims of this thesis.

3.1 Cellular mechanism for subthreshold resonance and selective firing in layer II neurons from the anterior nucleus of the cortical amygdala

Most of the results presented in the following section are part of a manuscript written by Dr. Magdalena Sanhueza and Jorge Vera published in the Public Library of Scientific Information (Plos One) Journal: Vera J, Pezzoli M, Pereira U, Bacigalupo J, Sanhueza M (2014) **Electrical Resonance in the θ Frequency Range in Olfactory Amygdala Neurons**. PLoS ONE 9(1): e85826. doi:10.1371/journal.pone.0085826. All figures where made by Jorge Vera using his original data, with the exceptions of Figures 1, 2 and 4 that where made with data collected by Dr. Maurizio Pezzoli during his PhD thesis performed at the laboratory of Dr. Sanhueza.

In this subsection we present the first characterization of resonant neurons from anterior cortical amygdala, we describe the cellular mechanism present in these neurons that allow them to resonate and also demonstrate that the subthreshold frequency preference of these neurons translates to a spiking regime, thus suggesting that resonance may play a functional role as a mechanism for frequency selection under processing of oscillatory activity.

3.1.1 Abstract

The cortical amygdala receives direct olfactory inputs and is thought to participate in processing and learning of biologically relevant olfactory cues. As for

other brain structures implicated in learning, the principal neurons of the anterior cortical nucleus (ACo) exhibit intrinsic subthreshold membrane potential oscillations in the theta-frequency range. Here we show that nearly 50% of ACo layer II neurons also display electrical resonance, consisting of selective responsiveness to stimuli of a preferential frequency (2-6 Hz). Their impedance profile resembles an electrical band-pass filter with a peak at the preferred frequency, in contrast to the low-pass filter properties of other neurons. Most ACo resonant neurons displayed frequency preference along the whole subthreshold voltage range. We used pharmacological tools to identify the voltage-dependent conductances implicated in resonance. A hyperpolarization-activated cationic current depending on HCN channels underlies resonance at resting and hyperpolarized potentials; notably, this current also participates in resonance at depolarized subthreshold voltages. KV7/KCNQ K^+ channels also contribute to resonant behavior at depolarized potentials, but not in all resonant cells. Moreover, resonance was strongly attenuated after blockade of voltage-dependent persistent Na^+ channels, suggesting an amplifying role. Remarkably, resonant neurons presented a higher firing probability for stimuli of the preferred frequency. Our results provide a complete characterization of the resonant behavior of olfactory amygdala neurons and shed light on a putative mechanism for network activity coordination in the intact brain.

3.1.2 Introduction

The amygdala complex is a heterogeneous group of subcortical nuclei and cortical areas located in the temporal lobe of the brain (McDonald, 1998). This complex is involved in the processing of biologically relevant sensory stimuli and in the generation of the autonomic, motor and endocrine responses induced by these stimuli (Pitkänen et al., 1997; Swanson and Petrovich, 1998). Moreover, several lines of evidence indicate that the lateral and basolateral subcortical amygdala nuclei (also known as the basolateral complex) are implicated in forms of associative learning and emotional memory, particularly in the case of fear conditioning paradigms and emotional stress (Ledoux, 2000; Sah et al., 2003).

The wide representation and the particular organization of olfactory connections to the amygdala distinguish the olfactory system from other sensory modalities, making it a privileged model for the study of the encoding of biologically relevant stimuli and memory processes involving emotions. Surprisingly, this possibility has been scarcely explored so far. While inputs from most sensory systems enter the amygdala at the basolateral complex via the thalamus and neocortical regions, afferent connections from the main olfactory bulb (OB) directly target the amygdala at its cortical region. OB mitral and tufted cells project their axons through the lateral olfactory tract to the piriform cortex (PC) and the amygdaloid cortical nuclei (anterior cortical nucleus, ACo, and posterolateral cortical nucleus; (Paxinos et al., 1999)). These nuclei have a laminar configuration, with an external cell-sparse layer (layer I) that mainly contains axon collaterals from the olfactory tract and apical dendrites from the principal cells located in the more dense layer II (McDonald, 1998). This olfactory region has been poorly

investigated, but recent anatomical evidence suggests a role in innate odor preference (Sevelinges et al. 2004; Sanhueza and Bacigalupo, 2005). Moreover, a behavioral and electrophysiological study supports its participation in olfactory fear conditioning in rats, as after training the synaptic potentials evoked by lateral olfactory tract stimulation are persistently potentiated specifically in ACo (Sevelinges et al., 2004).

We previously showed that a significant fraction of principal neurons from ACo (68%) and the posterolateral cortical nucleus (20%) displays intrinsic subthreshold membrane potential oscillations (MPOs) upon depolarization by DC current injection, mainly in the θ-frequency range (3-12 Hz) (Sanhueza and Bacigalupo, 2005). Similar θ rhythmic properties have been described in neurons from brain regions implicated in learning, such as the basolateral amygdala (Pape et al., 1998b), the hippocampus (Leung and Yim, 1991) and the entorhinal cortex (EC) (Alonso and Llinás, 1989).

In addition to MPOs, neurons from memory-related brain regions like the hippocampus, the EC and the lateral amygdala display θ-frequency subthreshold resonance (Leung and Yu, 1998; Pape et al., 1998b; Haas and White, 2002). Electrical resonance is the property of certain neurons to respond with a maximal voltage signal to the injection of a fluctuating current of a specific frequency (the resonance frequency, f_R), in contrast to most neurons that do not exhibit a preferred stimulation frequency, functioning mainly as low-pass filters. Intrinsic pacemaker properties and resonance rely on voltage-dependent conductances (Llinás, 1988; Hutcheon and Yarom, 2000). Resonance is generated by voltage-dependent currents that dynamically oppose to voltage changes, with long activation/deactivation times relative to the membrane time

constant (Hutcheon and Yarom, 2000). For fluctuating stimuli with frequencies low enough to allow the activation of these currents, the voltage response will be attenuated. The coexistence of this high-pass filter mechanism and the low-pass filter generated by the membrane passive properties gives rise to the band-pass filtering that defines resonance. Two specific active currents that have been shown to participate in theta resonance are the hyperpolarization-activated K^+/Na^+ current I_h (Biel et al., 2009) and the slow outward rectifier K^+ current regulated by muscarinic receptors, I_M (Brown, 1988; Wang et al., 1998). Subthreshold resonance depending on either I_h or I_M has been reported in different regions of the rodent brain. I_h–dependent resonance is observed in rat subiculum and EC (Wang et al., 2006; Nolan et al., 2007; Boehlen et al., 2013). On the other hand, a resonance mechanism relying on I_M exists in frontal cortex neurons of guinea pig (Gutfreund et al., 1995), but not of rat, where it is mediated by I_h (Hutcheon et al., 1996). Similarly, different reports claim for the involvement of either I_h or I_M in basolateral amygdala theta-resonance (Pape and Driesang, 1998; Ehrlich et al., 2012). Finally, a dual mechanism exists in rat CA1 pyramidal neurons, where resonance at hyperpolarized potentials relies on I_h and at depolarized voltages, on I_M (Hu et al., 2002).

In resonant neurons, subthreshold frequency preference may selectively translate to spiking patterns incoming oscillatory inputs at the resonance frequency. It could thus constitute a band-pass filter mechanism for transmitting repetitive activity in a limited frequency range, which may critically contribute to orchestrate neuronal network rhythms (Llinás, 1988; Hutcheon and Yarom, 2000). Neuronal resonance in the theta-frequency range may participate in the generation of the network theta waves arising during memory formation, suggesting an involvement of this intrinsic property in

learning. Accordingly, during network theta activity the induction of synaptic plasticity is facilitated (Huerta and Lisman, 1995).

The mammalian olfactory circuit is characterized by a pronounced theta-frequency activity, which is behaviorally driven by sniffing (Kepecs et al., 2006). At rest, breathing frequency is around 2-4 Hz, while sniffing frequency during exploration and odor recognition tasks is around 6-12 Hz, thus rhythmic activity spans the whole theta range (Kepecs et al., 2007; Wesson et al., 2008; Doucette et al., 2011). Sniffing evokes phase-locked spiking in principal cells of the OB and PC (Macrides and Chorover, 1972; Wilson, 2001; Cang and Isaacson, 2003) and correlated rhythmic activity in the hippocampus, a correlation that increases when the animal is evaluating the biological significance of the stimulus (Macrides et al., 1982). In this context, it becomes relevant to assess the existence of theta-resonance in neurons from the olfactory amygdala, a possible locus of olfactory-related emotional learning.

To assess neuronal resonance in ACo, we used the standard impedance amplitude profile (ZAP) protocol (Puil et al., 1987; Hutcheon and Yarom, 2000), which consists in the injection of a sinusoidal current of constant amplitude and linearly changing frequency. By impedance analysis we were able to identify layer II ACo resonant neurons and determine their resonance frequencies. We identified the conductances involved in resonance generation at different voltage ranges and developed a comprehensive computational model that reproduces both subthreshold resonance and neuronal spiking behavior during ZAP stimulation.

3.1.3 Results

Resonant and non-resonant neurons in ACo

Inspection of neuronal output voltage waves to ZAP stimulation and their impedance profiles (see Methods) suggested the existence of two populations of ACo layer II cells with different subthreshold behaviors: resonant and non-resonant. Figures 1A-D and 1E-H show voltage waves and impedance analysis for two ACo neurons exemplifying resonant and non-resonant types, respectively. Panels 1A and 1E illustrate the voltage responses to ZAP stimuli applied superposed to DC current injections of different amplitudes. In the non-resonant cell, the maximal voltage response was attained at the lowest stimulus frequency (Fig.1E), as expected from general passive RC membrane properties acting as a low-pass filter (see impedance profiles in Figure 1F). In contrast, for the cell in 1A the highest voltage amplitude was reached at a narrow frequency interval within the range scanned by the ZAP stimulus (Fig. 1A), giving rise to band-pass filter profiles (Fig. 1B) that are indicative of resonant behavior. This suggests the existence in this neuron of voltage-dependent currents that decrease the ZAP-induced voltage fluctuations at low frequencies. Such resonant impedance profile can be described by an RLC equivalent circuit ((Erchova et al., 2004); see Methods). The degree of resonance (Q factor or value; see definition in Methods) and the resonance frequency (f_R) were measured by fitting to the experimental impedance profiles a theoretical curve obtained from this linearized model. The model has the advantage of being applicable even if the specific conductances involved in the generation of the resonant profile are not known, but it has other limitations that are

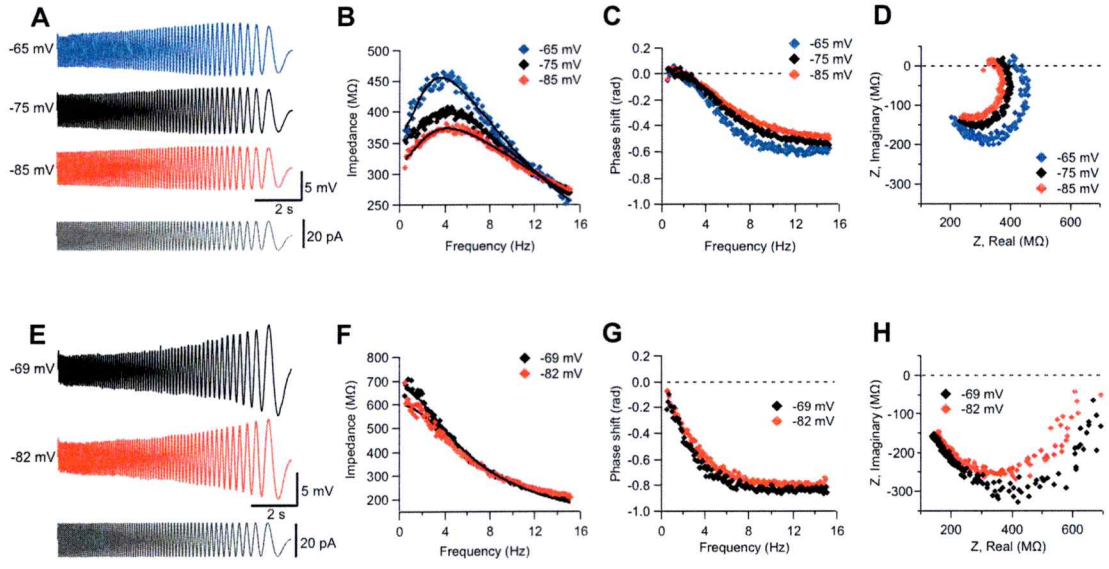

Figure 1. Resonant and non-resonant layer II ACo neurons. *A-D,* Voltage waveforms and impedance analysis from a representative resonant neuron. *A,* Voltage response to a 10 s ZAP stimulus (lower trace) of 10 pA amplitude and linearly decreasing frequency (15 – 0 Hz), at different membrane potentials. *B*, Resonant impedance profiles for data shown in A. Data were fitted by a theoretical curve obtained from the phenomenological RLC circuit model (lines; Q = 1.22, 1.12, 1.15 and f_R =3.6, 4.0, 4.2 Hz, for -65, -75 and -85 mV, respectively). *C,* Phase shift of the voltage waves relative to the injected current waves, as a function of frequency. *D,* Impedance vectors are represented as points in the complex plane. Here the distance to the origin corresponds to the impedance magnitude (plotted in B) and the angle with the real axis represents the phase shift or impedance phase (shown in C). Frequency increases in the clockwise direction. *E-H,* Same as A-D, for a non-resonant cell.

discussed below. Therefore, it was used here mainly as a tool to discriminate and quantify resonant behavior.

The representative resonant neuron in Figure 1A-D displays band-pass filter properties in the whole subthreshold voltage range. Least-square fits of impedance data to the theoretical curves are shown in Figure 1B (black lines). The Q values for -65, -75 and -85 mV were 1.22, 1.12 and 1.15, respectively, and f_R were 3.7, 4.1 and 4.2 Hz, respectively. On the other hand, the non-resonant neuron presented Q = 1.00 for all potentials recorded (only two of them are shown).

The impedance phase (or phase shift of the voltage wave with respect to the injected current wave), also has different frequency profiles for neurons described by RC (non-resonant) or RLC (resonant) electrical circuits (Koch, 1984; Hutcheon and Yarom, 2000). In the first case, the voltage always lags the current wave due to the membrane capacitive properties, and the phase increases monotonically with the oscillation frequency until reaching a plateau (Fig. 1G). In the second case, the slow inductive currents that oppose voltage changes at low frequencies reduce not only the amplitude of voltage deflections but also the time to reach peak values are reached, compared to the non-resonant profile. This is manifested as a reduction in the phase lag of the voltage wave relative to the injected current at low frequencies. On the other hand, at higher frequencies the capacitive component dominates (Fig. 1C; compare to Fig. 1G). At frequencies lower than f_R, the inductive properties may dominate over passive low-pass filter effects, thus generating positive phase values (the voltage wave precedes the current wave; see Discussion). For the resonant cell in Figure 1C this phenomenon is observed for frequencies lower than 2 Hz, while the reduction in voltage lag is already

apparent for frequencies around f_R (compare with Figure 1G). The complex representation of impedance, summarizing information of its magnitude and phase (see Methods), is shown in Figures 1D and H, for the different voltages. Here the impedance magnitude corresponds to the length of the vectors connecting the origin to each point. Positive ordinate values represent positive phase shifts of the output voltage with respect to the input wave (Fig. 1D).

According to our discrimination criterion ($Q \geq 1.10$), one half of the cells recorded in regular ACSF (79 out of 156; 51%) displayed resonance in at least one sub-range of voltage (see below) and were classified as resonant neurons. We found no statistically significant differences between the passive electrical properties of resonant and non-resonant cells; average results (from 10 neurons of each type) were, respectively, R_{in} = 280 ± 62 MΩ and 266 ± 81 MΩ (p = 0.79), C = 60 ± 22 pF and 79 ± 27 pF (p = 0.09), τ = 16 ± 5 ms and 20 ± 6 ms (p = 0.12), and V_r = 67.8 ± 4.6 mV and 65.2 ± 5.6 mV (p = 0.33). To confirm that resonance was caused by frequency-dependent filter membrane properties instead of other time-dependent processes, we applied ZAP stimuli of increasing and decreasing frequencies in 30 cells. The impedance profiles obtained were indistinguishable in both cases (not shown). We showed that resonance was an intrinsic property of neurons, not involving network effects in its generation mechanism, as it was still observed in the presence of the inhibitors of fast glutamatergic and GABAergic synaptic transmission mentioned above (39 out of 86 cells). We did not find qualitative differences in the resonant profiles for the two conditions.

We observed that the majority of cells displaying resonant behavior presented this property over the whole subthreshold voltage range, as in the example shown in Figure1. However, in several cases action potentials were triggered when exploring the depolarized voltage range. In other cases, the quantitative threshold criterion for resonance was not fulfilled both below and above the resting potential, even though a trend to display band-pass filter properties was often observed, as indicated by both the voltage waveform and impedance profile ($Q > 1.00$). Thus, instead of classifying neurons in terms of the voltages at which they did or did not display resonance we opted for a graphic representation of the voltage-dependent filter properties of the whole population of recorded neurons, including those classified as resonant and non-resonant; we made histograms of the Q values measured at different voltage ranges. The left panels of Figures 2A and B display the histograms for two voltage ranges (10 mV wide), centered at -85 and -65 mV, respectively. Cells displaying $Q \geq 1.10$ are shown in red and those with $Q < 1.10$, in black. The histograms show a large subpopulation of neurons clearly falling in the category of non-resonant cells with Q identical to 1.00, which means that the maximal impedance is observed exactly at the lowest frequency (0.5 Hz). This highly populated class of neurons is followed by a group of cells with $1.00 < Q < 1.05$, most probably belonging to the same non-resonant type as it is separated from a second clearly differentiated subpopulation of cells with Q values close to or higher than 1.10. Note that the histograms suggest that a few cases (7% and 9% of total, for -85 mV

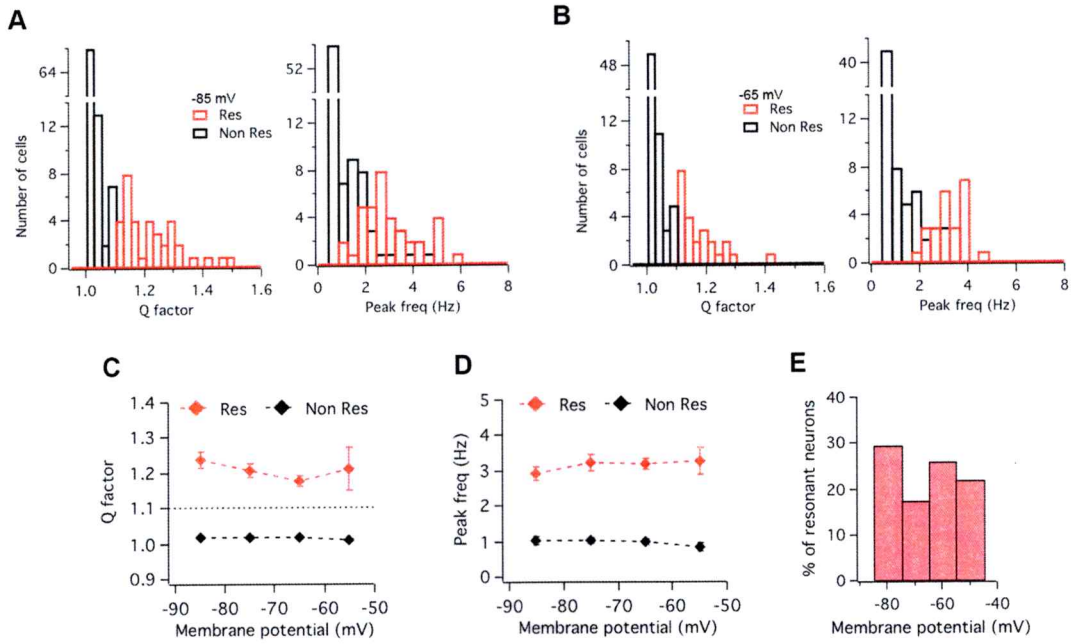

Figure 2. Q value and peak frequency distributions confirm the existence of resonant and non-resonant subpopulations of neurons. *A,* Histograms of the Q factors (left) and the frequencies at which Z reaches its maximum (peak frequency; right), for ZAP stimulation at an average voltage of -85 mV (i.e., in the range from -80 to -89 mV; n = 125 neurons). Data with Q < 1.10 are shown in black and that with Q ³ 1.10, in red. *B,* Same as in A, for -65 mV (-60 to -69 mV; n = 92 neurons). *C,* Average Q factor for resonant and non-resonant ACo neurons at different membrane potentials. *D,* Average frequency at Z_{max} (peak frequency) as a function of voltage, for both subpopulations. *E,* Percentage of neurons displaying resonant behavior at the indicated voltage ranges (30, 17, 26 and 22% for -85, - 75, -65 and -55 mV, respectively). The analyses in C-F were obtained from the pooled data from 156 neurons. The number of cells recorded at each potential range was 125, 132, 92 and 41, for -85, -75, -65 and -55 mV, respectively (note that not all neurons were recorded at the four potential ranges).

and -65 mV, respectively) in the range $1.05 < Q < 1.10$ that were classified as non resonant by the criterion $Q \geq 1.10$, may actually belong to the resonant subpopulation. However, as our criterion was set to avoid misclassification of noisy profiles, we prefer to consider these small percentages into the experimental uncertainty instead of overestimating the proportion of resonant cells. Probably the most important outcome of the histograms shown in the left panels of Figure 2A,B, is that they confirm the existence of two distinct populations of ACo layer II cells, resonant and non-resonant, instead of just one population with different grades of resonant behavior. This conclusion is further supported by a plot of the average Q values of resonant and non-resonant cells as a function of voltage (Fig. 2C), where the two populations are clearly distinguishable. Remarkably, Figure 2C indicates that resonant behavior does not disappear at resting membrane potential, in contrast to what happens in CA1 neurons (Hu et al., 2002).

In the right panels of Figures 2A, B we plotted the frequency at which the peak impedance was observed (corresponding to f_R in the case of resonant cells and shown here in red). Histograms illustrate the range of frequencies observed at these two membrane potential ranges and Figure 2D shows the average values for the different subthreshold voltage ranges. Finally, the percentage of resonant cells per membrane potential range is shown in Figure 2E. Note that these percentages (30% or less) are not inconsistent with our previous statement that about 50% of ACo neurons present resonance at least at one potential range.

In the next sections we describe a series of experiments in which pharmacological tools where used to identify the membrane conductances implicated in resonance at hyperpolarized and depolarized potentials in ACo.

Role of the voltage-gated persistent Na^+ current (I_{NaP})

Subthreshold membrane potential oscillations and neuronal resonance are usually thought to be related phenomena involving similar voltage-dependent membrane conductances, even though the role and impact of these conductances in the two processes may not necessarily be the same (Hutcheon and Yarom, 2000). As a first attempt to identify the ion channels implicated in ACo resonance, we tested if the blockade of persistent voltage-gated Na^+ currents, that we had previously shown to abolish oscillations (Sanhueza and Bacigalupo, 2005), could affect resonance. Figure 3 shows an example of a resonant neuron recorded before and during bath application of tetrodotoxin (TTX, 1 μM). Comparison of output waves (Fig. 3A1, A2) and impedance profiles (Fig. 3B) indicates that the band-pass filter properties are strongly attenuated for depolarized potentials under TTX. An overall reduction of voltage response is observed, mainly for lower frequencies. The average effect of this drug on resonance in the group of cells studied was quantified in terms of the changes in Q. On average, Q value at -65 mV was reduced from 1.14 ± 0.04 in control conditions, to 1.03 ± 0.04 in the presence of TTX ($n = 6$, $p = 0.002$; paired t-test). Figures 3C and D show the phase shift profile and complex impedance plots for control and TTX conditions. The plot in Figure 3C shows that in the presence of TTX the phase profile preserves the inductive properties at

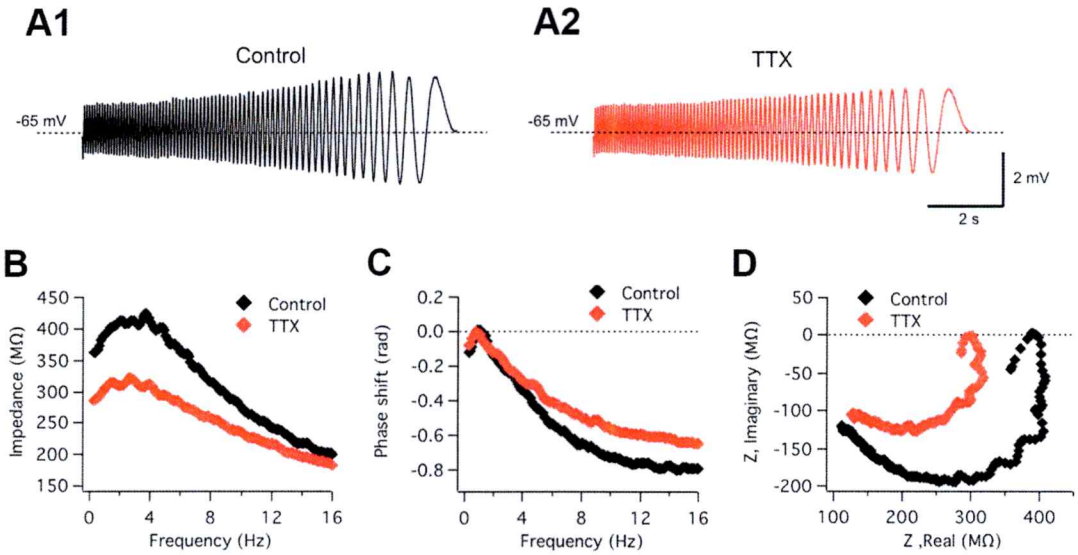

Figure 3. I_{NaP} plays a critical amplifying role in resonance but is not involved in band- pass filtering. Representative experiment (n = 6) illustrating the effect on resonance of blocking voltage-dependent Na^+ currents. *A,* Voltage responses evoked by ZAP stimulation in a resonant neuron before (A1; Control) and during (A2) the extracellular application of TTX (1 μM). *B,* Impedance profiles before (black) and during (red) TTX treatment. f_R and Q value in control conditions were 3.0 Hz and 1.25, and during TTX superfusion, 2.4 Hz and 1.08, respectively. *C and D,* Comparison of phase shift profiles and complex impedance representations, respectively, indicating that while impedance amplitude was strongly reduced by TTX (see also B), the phase resonant spectrum is still present The ZAP protocol was 20-0 Hz and 10 pA amplitude. See text for average data from six experiments. ZAP stimulus: 15-0 Hz, 10 pA.

low frequencies that distinguish resonant from non-resonant neurons. Instead, TTX caused an increase in phase at high frequencies (see Discussion). Figure 3D also illustrates the phase shift conservation at low frequencies, including phase values close or above zero, while the strong TTX-induced impedance decrease is apparent. The fact that phase properties at low frequencies were preserved while resonance pattern was clearly reduced in the impedance curve, suggests that the conductances responsible for the inductive membrane properties were not targeted by the toxin. Therefore, it seems probable that, as reported for other rat brain regions (Hutcheon and Yarom, 2000; Hu et al., 2002), a persistent voltage-gated Na^+ current amplifies the resonance behavior, instead of taking part in its induction mechanism. In agreement with this interpretation, TTX application to a non-resonant neuron also reduced the impedance (not shown); this attenuation was higher for more depolarized baseline potentials, revealing a general amplifying effect not specifically related to the resonance phenomenon.

Voltage-dependent currents involved in resonance: contribution of I_h and I_M

As mentioned above, two specific active currents presenting biophysical properties consistent with a participation in theta resonance at the analyzed voltage ranges are I_h and I_M. We first evaluated the contribution of these currents to ACo neurons resonance by using pharmacological tools. As I_h is known to be blocked by extracellular Cs^+ in the low millimolar range (Halliwell and Adams, 1982; Spain et al., 1987; Klink and Alonso, 1993), we tested if bath applications of 4 mM Cs^+ (n = 9) affected voltage waveforms and impedance or phase profiles. An example of these experiments is shown in Figure 4. Note that here the impedance profiles before and after

drug application were normalized (see Methods) for a more straightforward comparison of profile shape and to cancel any global shifts due to input resistance modification. We found that at hyperpolarized potentials resonant profiles were completely lost during Cs^+ application (Fig. 4A1; similar results were obtained at -77 and -70 mV, not included). In contrast to TTX, Cs^+ increased impedance in the lower frequency range (Fig. 4B1), consistent with the removal of a high-pass filter mechanism, represented by the theoretical inductive branch of the RLC phenomenological model circuit, but resulting from the action of specific voltage-dependent conductances in resonant cells. The average Q values at hyperpolarized potentials for all tested resonant cells before and after Cs^+ application were Q = 1.17 ± 0.09 for Control and 1.01 ± 0.01, for Cs^+ ($p = 0.0009$, $n = 9$; paired t-test). The phase curve was also deeply modified by the blocker (Fig. 4C1), the phase shift reduction and the positive lags originally observed for low frequencies disappeared and the curve was transformed from one resembling an RLC circuit to a mono-phase function characteristic of an RC circuit. This result differs from the effect of TTX, as in that case the resonant phase profile was preserved (Fig. 4C). This result and the aforementioned increase in impedance indicate that, in contrast to TTX, Cs^+ targets the resonance-generating mechanism.

In the range of the hyperpolarized potentials considered here and at resting potential, the only known current sensitive to extracellular Cs^+ is I_h. Therefore, our results suggest that this is the current responsible for resonance at these voltages. Moreover, Cs^+ application

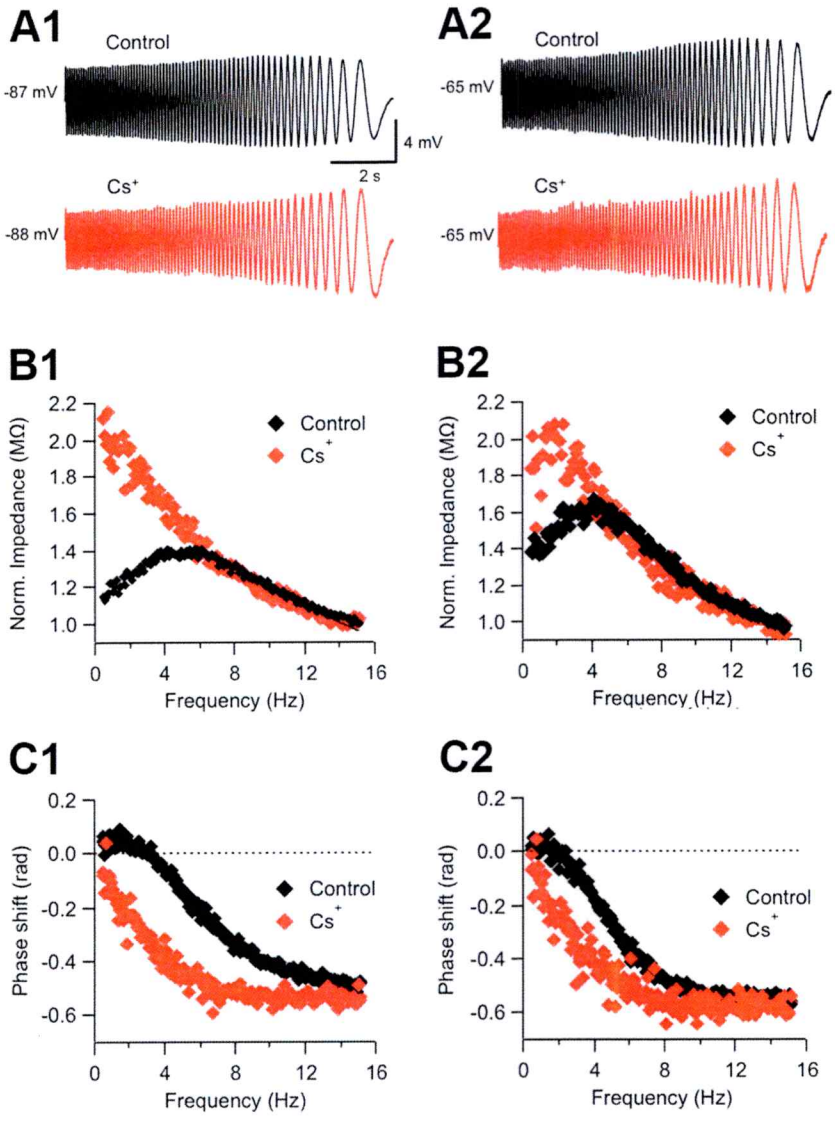

Figure 4. Resonance blockade by external Cs+. *A1*, ZAP-stimulus-induced voltage responses of a resonant neuron at a hyperpolarized potential (n = 7), before (Control) and during extracellular application of Cs+ (4 mM). *B1,* Normalized impedance profiles for the traces shown in A1. Note that in the presence of Cs+ impedance increases at low frequencies and resonance is completely lost (Q = 1.21 for Control and 1.00 for Cs+, as calculated from the least-squares fitted curve). *C1*, Phase shift for both conditions plotted against frequency, indicating that the inductive profile is missing in the presence of Cs+. *A2-C2,* same as A1- C1, for a depolarized potential (-65 mV; n = 4), Q = 1.19 in control conditions and 1.00 in Cs+. See text for average data from nine experiments. ZAP stimulus: 15-0 Hz, 10 pA.

had no effect on non-resonant cells, suggesting that I_h is very small or absent in these cells (Vera et al).

Interestingly, in the experiment shown in Figure 4 both voltage waveforms (Fig. 4A2) and resonant impedance profile (Fig. 4B2) were also deeply affected by Cs^+ at depolarized potentials. Moreover, the resonant phase profile was also modified, being now closer to the RC behavior (Fig. 4C2). Considering all experiments with Cs^+, in those cells in which a resonant profile was resolved at subthreshold depolarized potentials without action potential discharges (~ -65 mV; 4 cells), resonance strength showed a trend to decrease in Cs^+, though the difference did not reach statistical significance (Q = 1.27 ± 0.15 for Control and 1.03 ± 0.03 for Cs^+; p = 0.054; paired t-test). These experiments suggest a contribution of I_h to resonance also at perithreshold voltages, in contrast to what has been reported for CA1 pyramidal cells, for which at depolarized potentials resonance relies exclusively on I_M (Hu et al., 2002). To assess a possible contribution of both I_M and I_h to perithreshold resonance in ACo neurons, we used more specific pharmacological tools.

We first evaluated the effect of the specific I_h blocker ZD7288 on resonant behavior (n = 5). As shown in Figure 5A1 and A3, application of this drug completely abolished resonance at -75 mV. When considering all experiments, the average Q value at this potential was 1.14 ± 0.06 in control conditions, decreasing to 1.01 ± 0.02 in the presence of ZD7288 (p = 0.008; paired t-test, n = 5). This result reproduces the observations made at hyperpolarized potentials during Cs^+ application and confirms a role of I_h in the generation of subthreshold resonance in ACo neurons. Remarkably, as

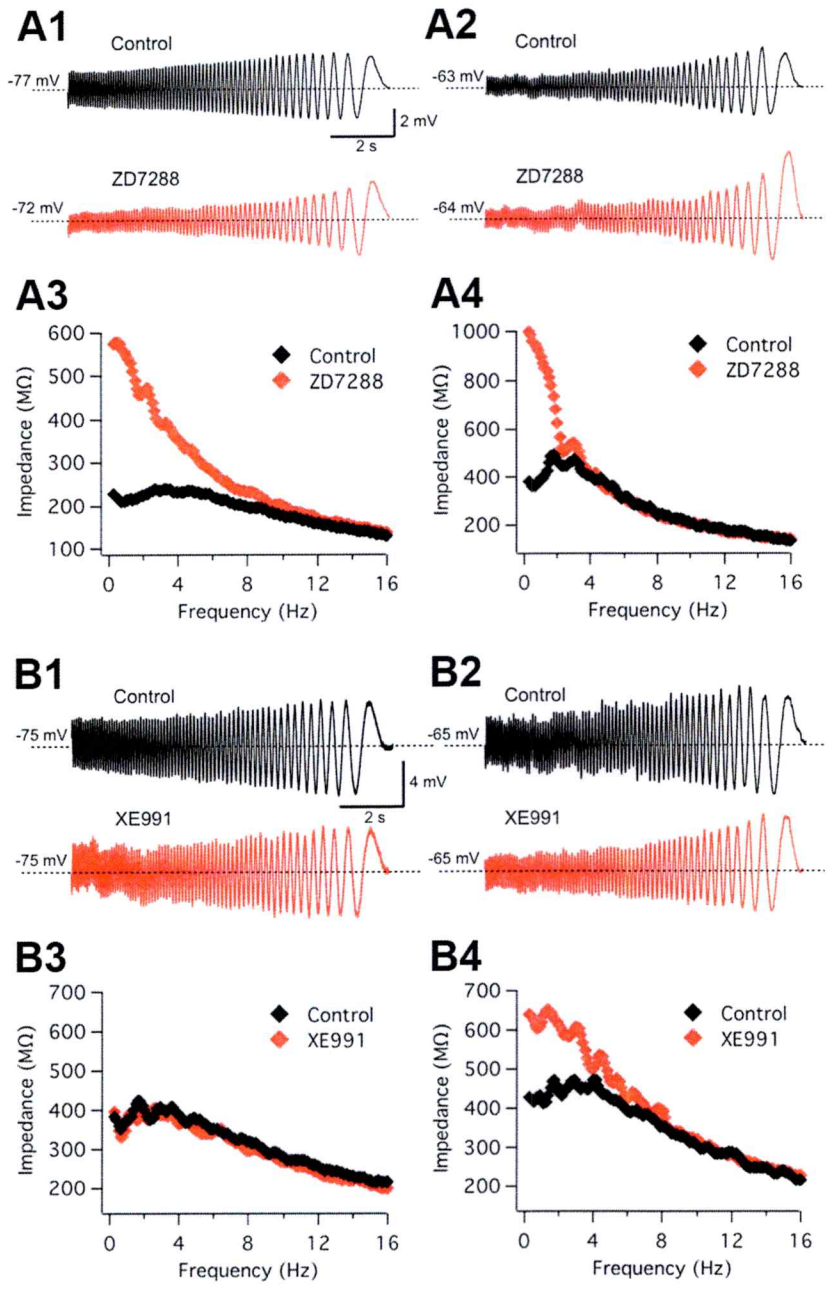

Figure 5. Subthreshold resonance depends on I_Z in the whole subthreshold range; I_M also contributes in a subset of neurons at depolarized potentials. *A1-A4,* Effect on resonance of the selective I_h antagonist ZD7288 (10 μM; n = 5). Control ZAP-induced voltage traces are compared to those in the presence of ZD7288, at -75 mV (A1) and at -65 mV (A2). The corresponding impedance profiles are shown in A3 (Q = 1.25 at f_R = 2.35 Hz, for control and Q = 1.00 for ZD7288; according to data fit by the theoretical curve, see Methods) and A4 (Q = 1.07 at f_R =1.8 Hz, for control and Q = 1.00, for

ZD7288), respectively. ZAP amplitude was 10 pA for control recordings, and 7/10 pA for ZD7288 at - 75/-65 mV. See text for average data from the 5 experiments, indicating that resonance essentially disappears in both potential ranges. *B1-B4*, Application of the selective KCNQ channel blocker XE991 (10 μM; n = 7) to a different neuron revealed a contribution of I_m at depolarized potentials. Voltage responses to ZAP stimuli applied at -75 mV (B1) and at -65 mV (B2), before and during the application of XE991. B3 and B4 show the impedance profiles for the traces in B1 and B2, respectively. It can be appreciated an increase in the impedance at low frequencies and the loss of resonance by drug application exclusively in the depolarized voltage range. Q and f_R values in control conditions were, respectively, 1.10 and 2.6 Hz (at -75 mV), and 1.20 and 2.8 Hz (at -65 mV). During XE911 application Q and f_R were 1.10 and 2.6 Hz (-75 mV) and 1.00 and 0.5 Hz (-65 mV). ZAP amplitude was 10 pA for control recordings, and 10/7 pA for ZD7288 at -75/-65 mV. See text for average data from seven experiments.

shown in Figures 5A2 and A4, ZD7288 also removed perithreshold resonance in this neuron. From the 5 neurons studied, only 3 displayed appreciable resonance at -65 mV (Q = 1.14, on average) and in all these cases it was abolished by ZD7288 (Q = 1.00). Therefore, these experiments confirm a contribution of I_h to resonance also at depolarized potentials.

On the other hand, a possible role of I_M in resonance was assessed by bath application of the selective I_M blocker XE991 in 7 resonant neurons. In the example shown in Figures 5B1-B4, XE991 abolished resonance at -65 mV, but not at -75 mV. The average effect of this drug on resonance for the different voltage ranges was as follows: For ZAP stimulation at -75 mV, resonance did not change (Control: 1.14 ± 0.05 and XE991: 1.14 ± 0.08; p = 0.4, paired t-test, n = 7). In contrast, at -65 mV, average Q value decreased from 1.14 ± 0.04 in control conditions, to 1.02 ± 0.03 during XE991 application (p = 0.007, paired t-test, n = 4). However, it was not possible to evaluate resonance at -65 mV in all neurons, since 3 out of 7 cells fired during ZAP stimulation at this potential, but in the remaining 4 experiments, resonance was present in control conditions and it was abolished by XE991 in 3 cases and decreased in the remaining cell. Therefore, on average, XE991 selectively targeted resonance at perithreshold membrane potentials. This treatment had no evident effect on non-resonant cells (Vera et al), confirming a contribution of I_M to the resonant profile at depolarized potentials.

Overall, these results suggest that two different voltage-gated currents participate in subthreshold resonance in ACo neurons: at rest and at membrane potentials hyperpolarized with respect to the resting values, resonant behavior relies on I_h, while at

perithreshold potentials, both I_h and I_M can contribute to resonance. The fact that most ACo resonant neurons presented resonance at hyperpolarized potentials, together with our observations with Cs^+ and ZD7288, point to I_h as a major generator of subthreshold resonance in this region. However, cases as that shown in Figure 5B, where I_M appears also to be key at perithreshold conditions, raises the question of whether the contribution of I_M is also a general property of resonant cells. As the activation voltage of I_M lies close to action potential threshold, it is often difficult to resolve the contribution of this current to subthreshold resonance. Also, our pharmacological experiments indicate that the presence of perithreshold resonance does not necessarily imply that I_M is always contributing, as it could also be generated by I_h. Therefore, we performed experiments in which TTX was applied to the external solution to avoid action potential discharges and in this way reach more depolarized potentials to optimize the conditions to observe I_M-dependent resonance (Hu et al., 2002). We found that I_M-resonance was actually not present in all resonant cells; one example is presented in Figure S1. The application of external Cs^+ in addition to TTX eliminated I_M-dependent resonance, leaving no signs of resonant behavior from hyperpolarized voltages up to -43 mV (Fig. S1), showing the absence of I_M-mediated resonance. For comparison, we reproduced results from CA1 pyramidal cells showing that in the presence of TTX, I_M-mediated resonance was observed in every cell (Hu et al., 2002).

Thus, our experimental results suggest the existence of a variety of resonant neurons in ACo. This diversity may be due to a differential expression of resonance-generating conductances in the cells.

Voltage-clamp recordings of currents involved in resonance: Activation voltage range of I_h and I_{NaP}

In order to determine the voltage range of activation of ionic currents involved in the generation of resonance we performed voltage-clamp experiments. With these experiments we aimed to characterize the voltage ranges for resonance and hypothesize about a possible superposition of them with the voltage range of action potential generation, which is necessary for translation of subthreshold frequency preference to a spiking regime. We used the same highly selective ion channel blockers utilized in current-clamp experiments to isolate I_h, I_M and I_{NaP}. We performed several experiments directed to record each of these currents and were able to systematically obtain blocker-sensitive currents only for I_h and I_{NaP}. In the case of I_M, after eight experiment using XE991 we could not isolate any blocker-sensitive current (The procedure is explained at supplementary Fig. S3). Nevertheless, this result is in agreement with the low abundance of resonant neurons that present I_M.

Voltage-clamp recordings of I_h

To isolate I_h, neurons were depolarized to -47 mV to deactivate HCN channels and then several hyperpolarizing potential pulses where applied (Fig. 6A). This procedure was performed in control condition to record whole-cell currents, and after addition of the selective I_h blocker ZD7288 (Fig. 6A middle.), thus recording all currents with the exception of I_h. The subtraction of both family traces reveals I_h (Fig. 6B). The isolated current displays the temporal course and voltage sensibility described for I_h, corresponding to a non-inactivating inward current that slowly activates by

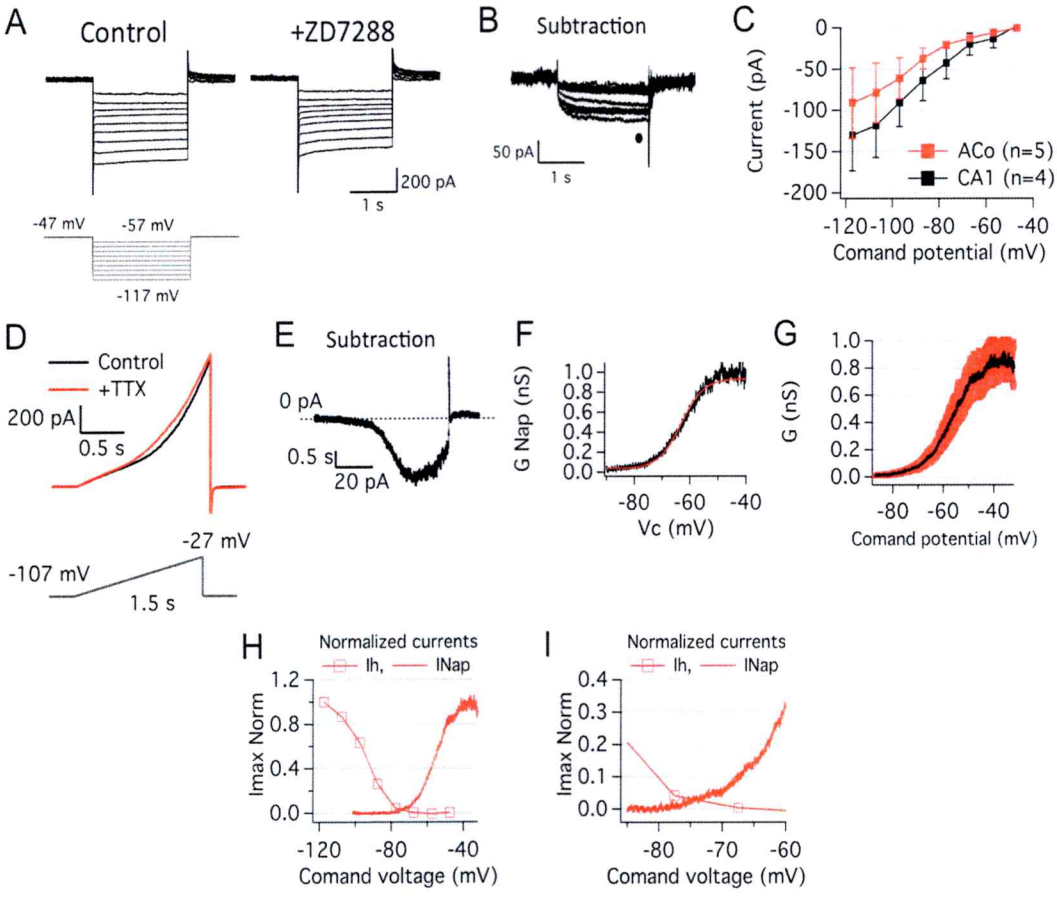

Figure 6. Voltage-clamp experiments confirmed the presence of I_h and I_{NaP}.
A Representative recording showing the voltage clamp protocol used to isolate I_h. Current activation was induced using hyperpolarized potential incursions (to -117 mV) from a depolarized holding potential (-47 mV). The same protocol was then repeated in the presence of specific blocker of this current, ZD7288. B I_h is obtained by subtracting the traces in the presence of the blocker from control condition. C Average I-V curve for I_h measured at the end of the pulse, circle in B. I_h recorded in CA1 hippocampal neurons is also plotted. D Protocol used to measure I_{NaP} in ACo neurons. We used a slow depolarizing voltage ramp to inactivate transient sodium current in control condition (black) and after the addition of 1 μM TTX (red). I_{NaP} is obtained from the subtraction of these two recordings. E I_{NaP} recorded in D and obtained by subtraction. F Single G_{NaP} curve of an ACo neuron obtained dividing I_{NaP} by V_m-E_{Na}. G Average G_{NaP} of ACo neurons. H Normalized I-V curves of I_h and I_{NaP} showed in C and F. I Zoom of interest region of graph shown in H.

hyperpolarization. The peak current (measured at the end of the 2 s pulse) reached an average of 91.0 ± 42.8 pA (n=5) at -117 mV, the most hyperpolarized potential tested (Fig. 6C). As a control we measured I_h in CA1 pyramidal neurons from hippocampus using the same procedure as in ACo neurons. The obtained traces are similar to those described for ACo neurons, as well as their amplitude and voltage sensitivity (Fig. 6C), thus validating our description.

Voltage-clamp recordings of I_{NaP}

Na^+ persistent current was isolated using a voltage ramp protocol, which depolarize neurons slowly enough to inactivate transient Na^+ current (Fig. 6D). Thus, recording the whole-cell current in control conditions and after the addition of 1 μM TTX, allows the isolation of I_{NaP} by subtracting both voltage traces (Fig. 6E). To favor an efficient voltage control during the ramp depolarization we reduced the extracellular Na^+ concentration, decreasing Na^+ reversal potential from 47 to 25 mV (see Methods). We obtained the conductance vs voltage curve for I_{NaP}, G_{NaP}, dividing the current curve by the driving force for Na^+ (Fig. 6F). Fitting a sigmoidal curve to the average G_{NaP} gives a voltage for half activation of -56.5 mV, an activation rate of 5.0 and a peak conductance of 0.95 nS near -40 mV (Fig. 6G). These values of amplitude and voltage sensitivity agree with those reported for this I_{NaP} in other cell types.

The persistent Na^+ current was recorded in a total of 6 neurons, with 4 of them also displaying I_h (thus being resonant) while the remaining 2 neurons not (being non-resonant), confirming the presence of I_{NaP} in both groups of neurons (not shown).

Comparison of activation voltage ranges for I_h and I_{NaP}

All previous experiments show that the main currents related to resonant behavior in ACo neurons are I_h and I_{NaP}. Therefore, any possible translation of subthreshold frequency preference to spiking regime relies on the overlap of the voltage ranges in which resonance and spike generation operates. Since both currents activate at opposite voltage ranges we compared their voltage dependences to see if their share a common voltage region for activation. For a more straightforward comparison, and thinking in a more qualitative analysis, we normalized both currents by its peak value and plotted them together (Fig. 6H and I). This procedure shows that only a small fraction of these currents activated at the same voltage range, generating only a narrow voltage window for simultaneous activation.

To investigate whether these neurons translate their subthreshold frequency preference to a spiking regime we conducted the following series of experiments.

Resonant neurons from ACo translate subthreshold frequency preference to a spiking regime.

The different subthreshold voltage responses to oscillatory inputs in resonant and non-resonant neurons suggest that they shall display a completely different behavior during suprathreshold rhythmic stimulation, which may have an impact on processing of

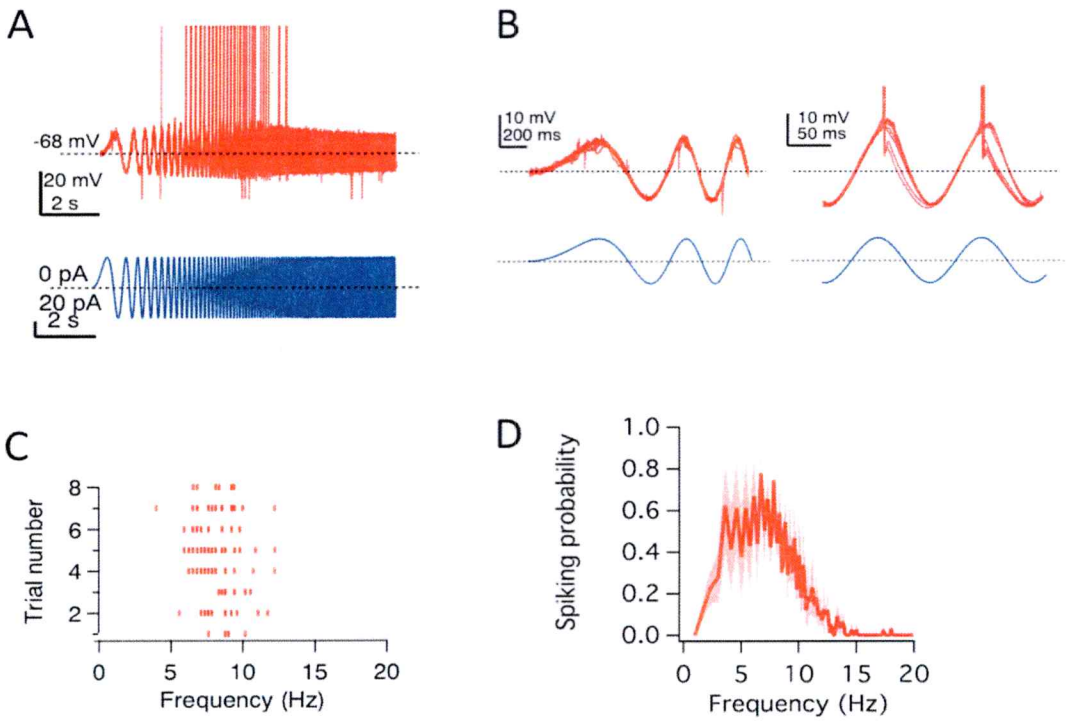

Figure 7. Resonant neurons from ACo translate their subthreshold frequency preference to spiking regime. A representative current-clamp recording of the voltage response (overlap of 8 traces, red) of an ACo resonant neuron under stimulation with the ZAP protocol (blue). Neuron was held at -68 mV by manually DC injection. B Zoom of voltage response (red) and current stimulation (blue) traces showed in A at low frequencies (left) and at preferred frequency range (right). C Raster plot showing the spiking activity vs frequency of stimulation for 8 consecutive oscillatory stimulations (showed in A). D Average spiking probability as a function of frequency of stimulation of resonant neurons, for details see Methods (n=6).

incoming inputs. To test this prediction, we examined responses of resonant neurons to ZAP current stimuli applied while cells were slightly depolarized from -65 mV. Figure 7A shows an example of these experiments (n = 4), in which 8 consecutive recordings are displayed. Low-frequency voltage oscillations are attenuated by the activation of I_h during the hyperpolarized period and its deactivation during depolarizing incursions (Fig. 7B left). At higher frequencies, I_h does not have time for significant activation thus it does not further attenuate voltage responses and the cell depolarizes towards the spike threshold (Fig. 7B right). This selective firing at theta frequencies is reliable, being observed in all trials (Fig. 7C). An average histogram of the spiking probability as a function of frequency is presented in Figure 7D. It can be clearly observed that the resonant cell fires preferentially within a limited interval of frequencies of the oscillatory input and no discharges are elicited at the lowest or highest explored frequencies.

3.1.4 Discussion

Here we report the existence of two neuronal populations in layer II of the cortical amygdala, resonant and non-resonant, with clearly different subthreshold membrane potential dynamics. Resonant neurons display an enhanced response to theta-range rhythmic stimuli of a preferred frequency between 2-6 Hz, whereas non-resonant neurons behave as low-pass filters with no frequency preference. Our data indicate that subthreshold frequency preference, or resonance, results from the existence of two active low-frequency filter mechanisms that reduce the response to slow oscillatory stimuli. These mechanisms are independent, one acting in the whole subthreshold voltage range and relying on I_h (that flows through HCN channels) and the other effective only at perithreshold potentials, generated by the muscarine-sensitive K^+ current I_M (depending upon KV7/KCNQ channels). The resonance is boosted by a persistent Na^+ current, I_{NaP}.

The mechanisms of subthreshold resonance in ACo

In general, resonance requires the coexistence of both high-pass and low-pass filter mechanisms in the cells (Hutcheon and Yarom, 2000). The high-pass filter involves slow voltage-dependent currents that are substantially activated only in the low frequency range and that when activated reduce the amplitude of voltage changes, decreasing the membrane impedance. In ACo neurons, the voltage dependence of I_h and I_M and their activation/deactivation time constants determine the frequency preference range. HCN channels slowly activate by membrane hyperpolarization giving rise to a net inward cationic current that promotes cell depolarization towards its reversal potential (-40 mV). In turn, KV7/KCNQ channels are closed at resting potential and are activated

by depolarization, originating an outward K^+ current that hyperpolarizes the cell back to its resting level. Oscillatory stimulation with a shorter period than the activation times of I_h or I_M will activate these currents, with the consequent shunting of the voltage deflections, hence acting as high-pass filters. For faster oscillatory stimuli the time needed to charge the membrane acts as a low-pass filter. The combination of these two filter mechanisms produces a voltage response with a maximal value determined by the tuning effect resulting from the time constant of the resonant currents and their passive membrane properties (resistance and capacitance).

The voltage dependence and kinetics of resonance-generating conductances also have an impact on the phase profile. The RLC phenomenological model offers a simplified alternative to simulate this effect, but it does not allow a straightforward understanding of what are the biophysical properties responsible for the phase change. As for the reduction in the amplitude of voltage oscillations at low frequencies, the effect on the phase results from the complex and dynamical interplay between the different ionic currents present in resonant cells and the membrane voltage, during the application of an external oscillatory current. In this context, the delayed voltage-dependent activation/deactivation of I_h (~100 ms at 30 °C) is critical, as what determines the activation level of I_h at a specific time is the voltage value ~100 ms earlier. To illustrate how this property affects the phase, we can compare the time at which the ZAP-induced voltage wave crosses the middle line (baseline voltage set by the injected DC current), in the presence or absence of I_h. In the first case, the activation of I_h will be high when approaching the middle line during depolarizing incursions (for frequencies around or below f_R), because the membrane underwent the maximal level of

hyperpolarization about a quarter of cycle earlier. Thus, when comparing the middle-line crossing times in the presence or absence of HCN channels, it is expected that these channels will fasten the depolarization process and the voltage will cross this level earlier. In turn, during repolarization I_h will exert a damping effect, but it will be comparatively weak due to deactivation of this current after reaching the voltage peak. Therefore, the presence of I_h leads to a reduction in the voltage wave lag relative to the current wave (impedance phase). Remarkably, depending on the relative contributions of inductive and passive membrane properties, and on the input frequency, the impedance phase may become positive, meaning that the voltage wave precedes the current wave (Fig.1C).

Interestingly, an effect of the short activation delay of I_{NaP} (~5 ms) on phase can also be resolved in our experiments. This effect goes in the opposite direction and mainly affects oscillations in the higher frequency range: as demonstrated by the increase in the phase caused by TTX at higher frequencies (Fig. 3C).

To our knowledge, this is the first time that a dual subthreshold resonant mechanism is described in neurons from the amygdaloid complex (even though this duality is not observed in all ACo cells). Previous work characterizing subthreshold behavior of basolateral amygdala neurons in guinea pig found resonance at depolarized membrane potentials, with a peak frequency of 2.4 Hz, that was attributed to an M-type current (Pape et al., 1998a). In that work resonance was only explored at membrane potentials more positive than -70 mV, for which it is likely that the HCN conductance may have not been sufficiently activated. However, no rectification was detected in the hyperpolarizing direction, suggesting that these channels are not significantly expressed

in the cells studied. Conversely, recent work in the rat supports a contribution of I_h to subthreshold resonance in the basolateral amygdala (Ehrlich et al., 2012). Although species differences may explain these discrepancies, further work is needed to elucidate whether the dual resonant behavior at theta frequency described here for rat ACo neurons is shared by other regions of the amygdaloid complex.

Subthreshold resonance relying on either I_h or I_M has been reported in different regions of the rodent brain. In the rat subiculum I_h–dependent resonance is observed at resting and hyperpolarized potentials, while no resonant behavior is observed at depolarized voltages (Wang et al., 2006). In the EC frequency preference requires I_h, with I_M playing a modulatory role (Nolan et al., 2007; Boehlen et al., 2013). On the other hand, an I_M–dependent resonance mechanism exists in frontal neurons from guinea pig (Gutfreund et al., 1995), but not from the rat, where it relies on I_h (Hutcheon et al., 1996). A dual subthreshold resonance mechanism similar to that reported here for ACo has only been found in rat hippocampal CA1 pyramidal neurons (Hu et al., 2002), suggesting a common strategy for neural activity orchestration or signal filtering in these two learning-related brain regions (Llinás, 1988; Hutcheon and Yarom, 2000), although they have some differences that are discussed below. In both CA1 and ACo neurons theta resonance implicates HCN and KV7/KCNQ channels, responsible for I_h and I_M, respectively (Wang et al., 1998; Biel et al., 2009).

We also report a contribution of I_{NaP} to resonance amplification in ACo neurons. I_{NaP} plays a similar role in the rat basolateral amygdala, the EC, the frontal cortex and the hippocampus (Gutfreund et al., 1995; Hutcheon et al., 1996; Pape et al., 1998b; Hu et al., 2002; Wang et al., 2006; Burton et al., 2008). We show that non-resonant neurons

also possess the I_{NaP} current, therefore this regenerative voltage-dependent mechanism would contribute to further differentiate the responsiveness of the two populations: while in resonant cells I_{NaP} would preferentially amplify the largest voltage deflections generated for f_R, in non-resonant cells it would mainly enhance the voltage changes at the lowest frequencies, those that are filtered in the first neuronal subpopulation.

We previously reported that a high fraction of layer II ACo neurons displays intrinsic TTX-sensitive MPOs (Sanhueza and Bacigalupo, 2005). While the mechanisms underlying MPOs and resonance are thought to be related, several observations suggest they are not identical (Hutcheon and Yarom, 2000). In contrast to the effect on resonance, TTX completely abolished oscillations in ACo but only attenuated resonant behavior; similar observations have been made in neocortical neurons (Gutfreund et al., 1995). This suggests that I_{NaP} plays a critical role in the generation of MPOs, while playing mainly an amplifying role in resonance. Accordingly, MPOs are absent at resting and hyperpolarized membrane potentials, but this is not the case for resonance. Finally, while in ACo the frequency of MPOs strongly increases with depolarization (Sanhueza and Bacigalupo, 2005), resonance frequency is comparatively poorly voltage-dependent (see Fig. 2 for average values). Here we did not systematically compared the incidence of MPOs and resonance in the same neurons, however, the differences in the percentage of ACo resonant neurons (54%) and those displaying oscillations (68%) is not surprising, as both phenomena are not necessarily expressed in the same cells (Hutcheon and Yarom, 2000).

The frequency preference range of ACo neurons (Fig. 2) and CA1 pyramidal neurons (Hu et al., 2002) is comparable in experiments conducted at a similar

temperature. Nevertheless, differences arise when comparing resonance in ACo and CA1. Firstly, while in CA1 virtually all pyramidal neurons display theta frequency selectivity, we distinguish two main ACo cell populations, resonant and non-resonant. As our criterion to discriminate among these cell types was more stringent ($Q \geq 1.10$ compared to $Q > 1.00$ used in (Hu et al., 2002)), it is possible that the number of ACo resonant neurons was underestimated. However, the existence of an important population of cells lacking low-frequency filtering properties results apparent after examining their impedance profiles ($Q = 1.00$; Fig. 2B) and their insensitivity to Cs^+ and XE991. A second relevant difference is that while resonance in CA1 neurons virtually disappears at resting membrane potential, ACo neurons exhibit resonance in the whole subthreshold voltage range. This is probably due to the fact that, in contrast to CA1 cells, the contribution of I_h to resonance in ACo neurons is significant in the whole subthreshold range. Since our voltage clamp experiment showed a similar voltage range for activation of Ih at both cell types, we explain a strong impact of I_h in ACo neurons given their high input resistance. This produces that a small amount of current will produce a higher voltage response, thus producing more filtering. However, this hypothesis needs to be corroborated by computer simulations.

Finally, the dual mechanism was found in all CA1 pyramidal cells (Hu et al., 2002), but our evidence indicates that a subpopulation of resonant ACo cells lack the I_M–dependent mechanism.

Overall, our results suggest that, in contrast to other brain regions in which theta resonance has been studied, ACo neurons exhibit different contributions of the two

resonance-generating mechanisms, including cells expressing either both, only one or none of them.

Functional implications of theta-frequency resonance

Whether the intrinsic frequency preference of mammalian resonant neurons plays a role in the generation or spreading of orchestrated rhythmic activity in the brain is still an open question. A condition that has made the resolution of this subject elusive is that resonant neurons are mainly present in high-order processing regions, such as the hippocampus, the neocortex and the basolateral amygdala, where they receive extremely complex signal patterns influenced by different sensory modalities. Therefore, it is difficult to recreate in experimental conditions the activity patterns that these neurons receive *in vivo* and to evaluate the transfer function and filter properties that they display in the brain. This context makes the cortical amygdala a promising model to evaluate a possible functional role for theta frequency resonance, because as the ACo receives direct projections from the OB, it is expected that the afferent activity preserves the characteristic sniffing-driven rhythmicity of the olfactory circuit (Kepecs et al., 2006). The impact of the intrinsic frequency preference on neuronal and network dynamics upon such oscillatory drive remains to be determined. Resonant neurons may impose their individual frequency preference to the processed signals, excluding (filtering) other rhythmic inputs and selectively transmitting activity at their individual resonant frequency, thus working as frequency discriminators (resonators) (Izhikevich, 2003). This may constitute a mechanism for selective communication between neurons. Intrinsic resonance in the EC has been related to the existence of a cognitive spatial map

represented in a sequence of grid-like patterns, in which grid spacing correlates with the f_R of stellate neurons which is scaled along the dorso–ventral axis (Moser et al., 2008). Finally, resonance may contribute to generate or propagate network rhythms (Llinás, 1988; Hutcheon and Yarom, 2000).

Our observation that cortical amygdala neurons translate their subthreshold frequency preference to a spiking regime indicates that the spike-triggering machinery is coupled to the subthreshold resonance mechanism (the voltage for spike-generating Na^+ channel activation partially overlaps with the voltages at which I_M/I_h filter slow oscillations). Therefore, resonant ACo neurons are endowed with intrinsic electrophysiological properties that make them able to selectively generate and propagate rhythmic activity at their resonance frequency.

In contrast to CA1 pyramidal neurons, the dual mechanism of resonance is not general in ACo resonant neurons. Indeed, our study shows the existence of an inhomogeneous population of resonant cells, suggesting a complex signal processing in this olfactory region. Previous anatomical studies proposed that this region constitutes an intermediate formation among cortical and nuclear structures (Kalimullina et al., 2004). It can be speculated that different populations of resonant neurons in ACo may be activated depending on their specific afferent connectivity or on the sniffing pattern. Further studies are needed to explore these possibilities. Moreover, it should be noted that layer II cells recorded here may include both projection neurons and interneurons, thus additional work is required to evaluate if different mechanisms of resonance (or the absence of this property) are associated to specific neuronal types in ACo.

While neuronal resonance is usually studied upon somatic injection of oscillatory currents, the real effect of rhythmic synaptic drive on cellular activity also depends on synaptic and dendritic filter features. Synaptic filtering depends on the specific short-term plasticity properties (mainly presynaptic) of the studied connections (Izhikevich, 2003; Wang, 2010). On the other hand, distal dendritic resonance during local injection of oscillatory currents has been demonstrated in neocortical and hippocampal pyramidal cells; the dendro-somatic transfer impedance curve preserves the resonant profile, indicating that dendritic filtering does not eliminate frequency selectivity (Ulrich, 2002; Narayanan and Johnston, 2007). The cellular distribution of resonance-related conductances also shapes the effect of resonance on neuronal activity. In CA1 pyramidal neurons, the differences in localization and voltage activation range of these channels endow the cells with two segregated and independent cellular compartments for frequency preference and processing of incoming signals: dendrites resonate at hyperpolarized potentials (through HCN channels), whereas somatic filtering occurs at depolarized potentials (KV7/KCNQ channels) (Hu et al., 2007, 2009).

Finally, some authors have found that recreation of the *in vivo* conditions in brain slices by mimicking synaptic bombardment through a reduction in membrane resistance, dampens the intrinsic frequency preference of resonant neurons (Fernandez and White, 2008). While this possibility shall be examined in the cortical amygdala, the comparatively high basal input resistance of ACo resonant cells suggests that these neurons may preserve their filter properties and translate the subthreshold frequency preference into spikes when resistance drops *in vivo* due to synaptic activity (by ~50% (Destexhe et al., 2003)).

Olfactory coding, motivation and learning

Anatomical data suggest that the olfactory representations in the PC and olfactory amygdala are differentially organized. The spatial map characterizing the OB is lost in this cortex because the projections from one glomerulus to the PC are diffuse. In contrast, the projections from the different glomeruli to the cortical amygdala are organized into spatially stereotyped overlapping patches (Sosulski et al., 2011). The cortical amygdala receives inputs from the entire OB, but in contrast to PC, there is a bias to dorsal glomeruli (Miyamichi et al., 2011), shown to convey inputs required for innate responses to aversive odorants (Kobayakawa et al., 2007). These observations and the fact that olfactory tract stimulation induces a wave of activity in PC and EC that converges in the olfactory amygdala (Kajiwara et al., 2007), suggest that this structure plays a distinct, mostly unexplored role in olfactory integration.

Behavioral and electrophysiological studies in the olfactory system indicate that a single sniff is sufficient for fine odor discrimination (Uchida and Mainen, 2003). However, there are differences in the encoding strategies for odor identification depending on whether or not it has a behavioral value (for example, is it rewarded or not?). In the rodent OB and PC, odor identity is respectively encoded by the latency and the rate of the evoked activity phase-locked to the first sniff (Kepecs et al., 2006; Miura et al., 2012). In contrast, if the odor has a behavioral value, in both olfactory regions odor information is conveyed by the non-phase-locked firing rate during several sniffing cycles (Doucette et al., 2011; Gire et al., 2013). It should be noted that it is the increased synchronized activity of groups of neurons what is critical for encoding odor value during an active detection task, however, during passive detection odor identity is

strongly conveyed by spiking activity phase-looked to sniffing (Gire et al., 2013). In a similar way, the formation and expression of auditory emotional memories involve an increase in synchronized firing and rhythmic activity at the theta-resonance frequency of neurons in the lateral amygdala (Paré and Collins, 2000; Popa et al., 2010). Therefore, when the identification of an odor has biological relevance, additional high-order structures involved in emotional memory formation/retrieval may be recruited; our results point to the cortical amygdala as an attractive candidate endowed with theta rhythmic properties. In this context, the role of the cortical amygdala in olfactory integration may be related to innate or learned odor preference or aversion, based on a selective filtering of oscillatory activity.

3.1.5 References

Alonso A, Llinás R (1989) Subthreshold Na-dependent theta-like rhythmicity in stellate cells of entorhinal cortex layer II. Nature 342:175–177.

Biel M, Wahl-schott C, Michalakis S, Zong X (2009) Hyperpolarization-Activated Cation Channels : From Genes to Function. Physiol Rev 89:847–885.

Boehlen A, Henneberger C, Heinemann U, Erchova I (2013) Contribution of near-threshold currents to intrinsic oscillatory activity in rat medial entorhinal cortex layer II stellate cells. J Neurophysiol 109:445–463.

Brown D (1988) M-currents: an update. Trends Neurosci 11:294–299.

Burton BG, Economo MN, Lee GJ, White J (2008) Development of theta rhythmicity in entorhinal stellate cells of the juvenile rat. J Neurophysiol 100:3144–3157.

Buzsaki G (2002) Theta oscillations in the hippocampus. Neuron 33:325–340.

Cang J, Isaacson JS (2003) In vivo whole-cell recording of odor-evoked synaptic transmission in the rat olfactory bulb. J Neurosci 23:4108–4116.

Destexhe A, Rudolph M, Pare D (2003) The high-conductance state of neocortical neurons in vivo. Nat Rev Neurosci 4:739–751.

Doucette W, Gire DH, Whitesell J, Carmean V, Lucero MT, Restrepo D (2011) Associative cortex features in the first olfactory brain relay station. Neuron 69:1176–1187.

Ehrlich DE, Ryan SJ, Rainnie DG (2012) Postnatal development of electrophysiological properties of principal neurons in the rat basolateral amygdala. J Physiol 590:4819–4838.

Erchova I, Kreck G, Heinemann U, Herz VM (2004) Dynamics of rat entorhinal cortex layer II and III cells: characteristics of membrane potential resonance at rest predict oscillation properties near threshold. J Physiol 560:89–110.

Fernandez FR, White JA (2008) Oscillations and Periodic Firing in Stellate Cells of the Entorhinal Cortex. J Neurosci 28:3790–3803.

Gire DH, Whitesell JD, Doucette W, Restrepo D (2013) Information for decision-making and stimulus identification is multiplexed in sensory cortex. Nat Neurosci 16:991–993.

Gutfreund Y, Yarom Y, Segev I (1995) Subthreshold oscillations and resonant frequency in guinea-pig cortical neurons: physiology and modelling. J Physiol 483.3:621–640.

Haas JS, White J (2002) Frequency selectivity of layer II stellate cells in the medial entorhinal cortex. J Neurophysiol 88:2422–2429.

Halliwell J, Adams PR (1982) Voltage-clamp analysis of muscarinic excitation in hippocampal neurons. Brain Res 250:71–92.

Hu H, Vervaeke K, Graham LJ, Storm JF (2009) Complementary theta resonance filtering by two spatially segregated mechanisms in CA1 hippocampal pyramidal neurons. J Neurosci 29:14472–14483.

Hu H, Vervaeke K, Storm JF (2002) Two forms of electrical resonance at theta frequencies, generated by M-current, h-current and persistent Na+ current in rat hippocampal pyramidal cells. J Physiol 545:783–805.

Hu H, Vervaeke K, Storm JF (2007) M-channels (Kv7/KCNQ channels) that regulate synaptic integration, excitability, and spike pattern of CA1 pyramidal cells are located in the perisomatic region. J Neurosci 27:1853–1867.

Huerta PT, Lisman JE (1995) Bidirectional synaptic plasticity induced by a single burst during cholinergic theta oscillation in CA1 in vitro. Neuron 15:1053–1063.

Hutcheon B, Miura RM, Puil E (1996) Subthreshold membrane resonance in neocortical neurons. J Neurophysiol 76:683–697.

Hutcheon B, Yarom Y (2000) Resonance, oscillation and the intrinsic frequency preferences of neurons. Trends Neurosci 23:216–222.

Izhikevich E (2003) Bursts as a unit of neural information: selective communication via resonance. Trends Neurosci 26:161–167.

Kajiwara R, Tominaga T, Takashima I (2007) Olfactory information converges in the amygdaloid cortex via the piriform and entorhinal cortices: observations in the guinea pig isolated whole-brain preparation. Eur J Neurosci 25:3648–3658.

Kalimullina LB, Akhmadeev a V, Minibaeva ZR, Mutalova LR (2004) Structural organization of the amygdaloid complex of the rat brain. Neurosci Behav Physiol 34:551–555.

Kepecs A, Uchida N, Mainen ZF (2006) The sniff as a unit of olfactory processing. Chem Senses 31:167–179.

Kepecs A, Uchida N, Mainen ZF (2007) Rapid and Precise Control of Sniffing During Olfactory Discrimination in Rats. J Neurophysiol 98:205–213.

Klink R, Alonso A (1993) Ionic mechanisms for the subthreshold oscillations and differential electroresponsiveness of medial entorhinal cortex layer II neurons. J Neurophysiol 70:144–157.

Kobayakawa K, Kobayakawa R, Matsumoto H, Oka Y, Imai T, Ikawa M, Okabe M, Ikeda T, Itohara S, Kikusui T, Mori K, Sakano H (2007) Innate versus learned odour processing in the mouse olfactory bulb. Nature 450:503–508.

Koch C (1984) Cable theory in neurons with active, linearized membranes. Biol Cybern 50:15–33.

Ledoux JE (2000) Emotion Circuits in the Brain. Annu Rev Neurosci 23:155–184.

Leung LS, Yu H (1998) Theta-Frequency Resonance in Hippocampal CA1 Neurons In Vitro Demonstrated by Sinusoidal Current Injection. J Neurophysiol 79:1592–1596.

Leung LW, Yim CY (1991) Intrinsic membrane potential oscillations in hippocampal neurons in vitro. Brain Res 553:261–274.

Llinás RR (1988) The intrinsic electrophysiological properties of mammalian neurons: insights into central nervous system function. Science 242:1654–1664.

Macrides F, Chorover SL (1972) Olfactory bulb units: activity correlated with inhalation cycles and odor quality. Science 175:84–87.

Macrides F, Eichenbaum H, Forbes W (1982) Temporal relationship between sniffing and the limbic rhythm during odor discrimination reversal learning. J Neurosci 2:1705–1717.

McDonald J (1998) Cortical pathways to the mammalian amygdala. Prog Neurobiol 55:257–332.

Miura K, Mainen ZF, Uchida N (2012) Odor representations in olfactory cortex: distributed rate coding and decorrelated population activity. Neuron 74:1087–1098.

Miyamichi K, Amat F, Moussavi F, Wang C, Wickersham I, Wall NR, Taniguchi H, Tasic B, Huang ZJ, He Z, Callaway EM, Horowitz M, Luo L (2011) Cortical representations of olfactory input by trans-synaptic tracing. Nature 472:191–196.

Moser EI, Kropff E, Moser M-B (2008) Place cells, grid cells, and the brain's spatial representation system. Annu Rev Neurosci 31:69–89.

Narayanan R, Johnston D (2007) Long-term potentiation in rat hippocampal neurons is accompanied by spatially widespread changes in intrinsic oscillatory dynamics and excitability. Neuron 56:1061–1075.

Nolan MF, Dudman JT, Dodson PD, Santoro B (2007) HCN1 channels control resting and active integrative properties of stellate cells from layer II of the entorhinal cortex. J Neurosci 27:12440–12451.

Pape H, Driesang RB (1998) Ionic Mechanisms of Intrinsic Oscillations in Neurons of the Basolateral Amygdaloid Complex. J Neurophysiol 79:217–226.

Pape H, Driesang RB, Popescu AT, Paré D, Rainnie G (1998a) Ionic Mechanisms of Intrinsic Oscillations in Neurons of the Basolateral Amygdaloid Complex. J Neurophysiol 79:217–226.

Pape HC, Paré D, Driesang RB (1998b) Two types of intrinsic oscillations in neurons of the lateral and basolateral nuclei of the amygdala. J Neurophysiol 79:205–216.

Paré D, Collins DR (2000) Neuronal correlates of fear in the lateral amygdala: multiple extracellular recordings in conscious cats. J Neurosci 20:2701–2710.

Paxinos G, Kus L, Ashwell K, Watson C (1999) Chemoarchitectonic atlas of the rat forebrain. Academic Press.

Pitkänen a, Savander V, LeDoux JE (1997) Organization of intra-amygdaloid circuitries in the rat: an emerging framework for understanding functions of the amygdala. Trends Neurosci 20:517–523.

Popa D, Duvarci S, Popescu AT, Léna C, Paré D (2010) Coherent amygdalocortical theta promotes fear memory consolidation during paradoxical sleep. Proc Natl Acad Sci U S A 107:6516–6519.

Puil E, Gimbarzevsky B, Miura RM (1987) Voltage dependence of membrane properties of trigeminal root ganglion neurons. J Neurophysiol 58:66–86.

Sah P, Faber ESL, Lopez De Armentia M, Power J (2003) The amygdaloid complex: anatomy and physiology. Physiol Rev 83:803–834.

Sanhueza M, Bacigalupo J (2005) Intrinsic subthreshold oscillations of the membrane potential in pyramidal neurons of the olfactory amygdala. Eur J Neurosci 22:1618–1626.

Sevelinges Y, Gervais R, Messaoudi B, Granjon L, Mouly A-M (2004) Olfactory fear conditioning induces field potential potentiation in rat olfactory cortex and amygdala. Learn Mem 11:761–769.

Sosulski DL, Bloom ML, Cutforth T, Axel R, Datta SR (2011) Distinct representations of olfactory information in different cortical centres. Nature 472:213–216.

Spain WJ, Schwindt PC, Crill WE (1987) Anomalous rectification in neurons from cat sensorimotor cortex in vitro. J Neurophysiol 57:1555–1576.

Swanson L, Petrovich L (1998) What is the amygdala ? Trends Neurosci 21:323–331.

Uchida N, Mainen ZF (2003) Speed and accuracy of olfactory discrimination in the rat. Nat Neurosci 6:1224–1229.

Ulrich D (2002) Dendritic resonance in rat neocortical pyramidal cells. J Neurophysiol 87:2753–2759.

Wang HS, Pan Z, Shi W, Brown BS, Wymore RS, Cohen IS, Dixon JE, McKinnon D (1998) KCNQ2 and KCNQ3 potassium channel subunits: molecular correlates of the M-channel. Science 282:1890–1893.

Wang W-T, Wan Y-H, Zhu J-L, Lei G-S, Wang Y-Y, Zhang P, Hu S-J (2006) Theta-frequency membrane resonance and its ionic mechanisms in rat subicular pyramidal neurons. Neuroscience 140:45–55.

Wang X (2010) Neurophysiological and Computational Principles of Cortical Rhythms in Cognition. Physiol Rev 90:1195–1268.

Wesson DW, Donahou TN, Johnson MO, Wachowiak M (2008) Sniffing behavior of mice during performance in odor-guided tasks. Chem Senses 33:581–596.

Wilson D (2001) Receptive fields in the rat piriform cortex. Chem Senses 26:577–584.

3.2 Electrophysiological and morphological characterization of resonant and non-resonant neurons from layer II of the anterior nucleus of the cortical amygdala

This section is a draft manuscript written by Jorge Vera in preparation for submission to a peer-reviewed journal:

Vera J., Drechler A., Astudillo D., Mpodosis, J., Bacigalupo J. and Sanhueza M. (2014) Characterization of layer II neurons from the anterior nucleus of the cortical amygdala.

After the description of subthreshold resonance in neurons from the anterior nucleous of the cortical amygdala, in this section we continue with the characterization of ACo neurons with the aim to identify resonant cells as a defined cell type. Here we study the firing properties, morphology, synaptic response and connectivity of resonant and non-resonant neurons.

3.2.1 Abstract

The anterior nucleus of the cortical amygdala (ACo) is an integral part of the olfactory circuit and has been related to the processing of biologically relevant olfactory stimuli. ACo has been scarcely studied and is believed to share many neuronal properties with the piriform cortex (PC), the main olfactory cortex. We previously described that ~50% of ACo neurons display subthreshold oscillations and a stuttering firing pattern. In a separate investigation we found that near ~30% of ACo neurons present neuronal resonance in the theta range (3-8 Hz). By conducting whole-cell current-clamp experiments in rat brain slices we characterized the intrinsic and synaptic

properties as well as the morphology of resonant and non-resonant neurons from ACo layer II. We found that layer II neurons are morphologically heterogeneous, with no evident differences among resonant and non-resonant cells. Moreover, except the ability to resonate, both groups of neurons displayed similar electrophysiological properties, as spike threshold, current-frequency curves, as well as spontaneous or evoked synaptic activity. Interestingly, most resonant neurons display a stuttering firing pattern intermingled with subthreshold oscillations. The cytoarchitecture of ACo is characterized by cells of multiple morphologies lacking the ordered organization with stereotyped cell types observed in PC. However, the synaptic activity of layer II neurons evoked with electric stimulation at different cortical layers showed similarities with PC, suggesting comparable connectivity properties in these two olfactory cortices. We corroborated the direct projection from the olfactory bulb (OB) to ACo, and found that all layer II neurons have the synaptic machinery to process rhythmic OB input at theta-frequency.

Taking together, resonant neurons from ACo do not share similarities allowing to define them as a particular cellular type like CA1 pyramidal neurons. Furthermore, these results change the previous conception of ACo as a paleocortex similar to PC and highlight the properties of ACo neurons that favor processing of rhythmic activity at theta frequency.

3.2.2 Introduction

The complex of the amygdala is a brain region that processes sensory stimuli of biological relevance and commands appropriate emotional and behavioral responses (Ledoux, 2000; Swanson & Petrovich, 1998). The main nuclei of this complex are the basolateral (BLA) and centromedial (CMA), which receive inputs from all sensory modalities and generate their influence on behavior through connections with the hypothalamus and basal brain (McDonald, 1998). During evolution of mammals olfaction (smell) it has been the primary sensory modality that has driven the development of highly specialized emotions and behaviors (social, sexual, anxiety, fear, etc.), in agreement with the high number of projections from the olfactory system towards the amygdala (McDonald, 1998). Olfactory stimuli are processed in the olfactory bulb (OB) which projects to cortical regions via the lateral olfactory tract (LOT) (Sosulski, Bloom, Cutforth, Axel, & Datta, 2011). The activity generated in the OB reaches the amygdala (BLA and CMA) by two separated pathways, one through the piriform cortex (PC) which is considered the main olfactory cortex and is thought to have an important role in the representation of olfactory information (McDonald, 1998), reason by which it has been widely studied. The other pathway is conformed by the projections from the OB directly to the cortical amygdala, which is divided into anterior (ACo) and posterolateral nuclei (PLCO) (McDonald, 1998). This cortical region in turn projects to BLA and CMA and also to the hypothalamus, constituting the shortest pathway for olfactory stimuli to arrive to that region (McDonald, 1998). Despite its role as the first amygdaloid station for processing and transmitting olfactory information, the cortical amygdala has been scarcely studied.

It has been reported that rodents exposed to odors from natural predators (even without having previous experience of contact with the predator) show a general increase in the activity of BLA neurons, without activation of neurons at ACo (measured as c-fos positive neurons) (Dielenberg, Hunt, & McGregor, 2001). This data suggests that ACo is not involved in experience-independent (unconditioned) aversive olfactory responses. In addition to the signals coming directly from the OB to ACo, *in vitro* electrophysiological studies showed that after LOT stimulation the evoked activity converges into ACo after passing through the PC and entorhinal cortex (Kajiwara, Tominaga, & Takashima, 2007). This suggests that in the intact brain cortical amygdala receives and processes two subsequent olfactory-related activity waves, the first one directly from the OB and the second after processing by the other olfactory cortices. On the other hand, a study in which animals were trained to associate odors to electrical shocks (fear conditioning) showed that the association of the olfactory and the aversive stimulus was accompanied with an increase in synaptic strength in the connections from OB to ACo, while the synapses between the OB and the PC remained unchanged (Sevelinges, Gervais, Messaoudi, Granjon, & Mouly, 2004). Overall, this evidence suggests that ACo is involved in the processing and learning of biologically relevant olfactory stimuli.

The cortical amygdala is in a ventromedial position in the telencephalon of mammals, as a ventral continuation of the posteroventral PC (McDonald, 1998). ACo cytoarchitecture has not been characterized in detail and it is usually assumed to resemble PC as a three-layered paleocortex (McDonald, 1998). At PC, layer Ia is the most external and contains fibers from LOT, layer Ib has associational projections.

Layer II has the largest number of neurons packed in a well-defined layer and layer III has a lower density of cells (L. B. Haberly, 1983). It was recently described that PC layer II neurons have a functional stratification, with superficial neurons representing well defined cell types (pyramidal and semilunar neurons) with different synaptic and intrinsic properties that produce a differential processing of OB input (Suzuki & Bekkers, 2011). It is unknown whether ACo layer II neurons present the same types of neurons and therefore a similar processing strategy.

Previous work from our laboratory described that a subset of neurons from the cortical amygdala display subthreshold oscillations of the membrane potential (1-5 mV peak-to-peak amplitude) at theta frequency range (4-8 Hz) (Sanhueza & Bacigalupo, 2005). This group of neurons presents a stuttering firing pattern, which mix periods of firing with periods of subthreshold oscillations (Sanhueza & Bacigalupo, 2005). Recently, we found that 30% of ACo neurons display neuronal resonance, which means that their voltage response is higher when stimulated at a specific frequency range, in this case between 2-6 Hz (Vera, Pezzoli, Pereira, Bacigalupo, & Sanhueza, 2014). Therefore, under oscillatory stimulation, resonant neurons present a peak voltage response at the resonance frequency, f_R (Hutcheon & Yarom, 2000). It is speculated that resonant neurons stabilize oscillatory activity in neuronal networks (Wang, 2010), and given the strong oscillatory activity of the olfactory circuit (Kay et al., 2009; Kepecs, Uchida, & Mainen, 2006) and that ACo processes and transmits olfactory signals to other regions, it is possible that resonant neurons from ACo have a pivotal role in the coordination of oscillatory activity during olfaction.

Here we present a characterization of resonant and non-resonant neurons from ACo performed with current-clamp experiments. We measured intrinsic electrophysiological properties and studied neuron morphology. We also studied the synaptic inputs to these neurons recording evoked synaptic activity.

3.2.3 Results

The first step of this investigation was to characterize ACo neurons from layer II in order to investigate whether resonant neurons correspond to a well-defined cell type as occurs in other mammal brain areas like the hippocampus and entorhinal cortex. To this aim, we investigated three aspects of cell type identity: intrinsic electrophysiological properties, synaptic electrophysiological properties and cell morphology.

Characterization of resonance in ACo neurons

To investigate the intrinsic properties of neurons from layer II of ACo we conducted experiments on 54 neurons. Their properties were explored performing current-clamp experiments under both constant and oscillatory current injections at several membrane potentials. With those recordings it was possible to classify and correlate the subthreshold behavior of neurons (i.e. resonance) with suprathreshold properties (firing pattern, spike threshold and the like).

To determine if neurons display subthreshold resonance we used the sinusoidal current protocol (Zap, see Methods) to produce 5-10 mV peak-to-peak oscillations while injecting DC current to maintain the membrane potential near -80 mV. In agreement

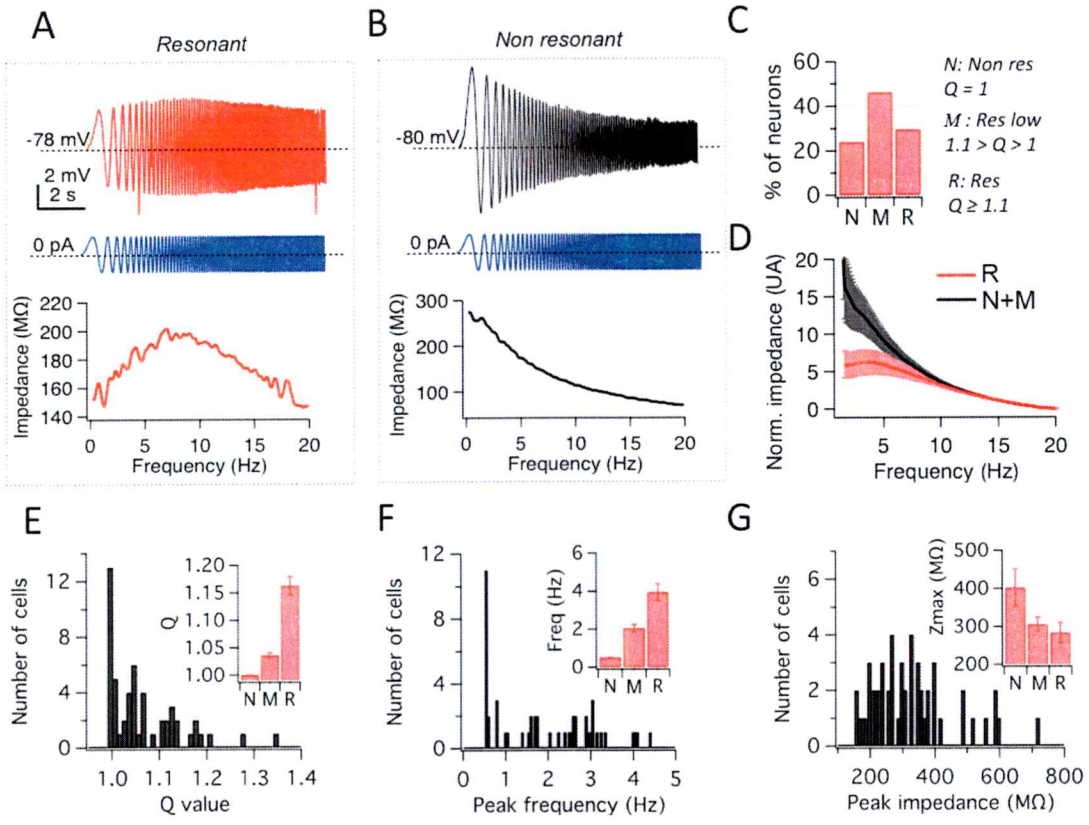

Figure 8. Characterization of subthreshold frequency preference in a subset of ACo neurons. A Voltage response (red) under ZAP stimulation (blue) and impedance profile (bottom, red trace) for a resonant neuron from ACo. B Voltage response (black) under ZAP stimulation (blue) and impedance profile (bottom, black trace) for a non-resonant neuron from ACo. C Relative abundance for resonant (R), non-resonant (N) and mixed (M) group of neurons. D Average impedance profile of R (red, n=10) and N+M (black, n=15) ACo neurons. Individual impedance profiles where normalized by the value at 15 Hz in order to compare frequency preference. E-G Histograms of Q-value (E), Peak frequency (F) and Peak impedance (G) for 54 recorded neurons. The insets show the average value for N, R and M groups.

with a previous report of our laboratory, we found neurons that responded with larger voltage oscillations at theta frequency range (~ 4 Hz), thus displaying subthreshold frequency preference (Fig. 8A) and also neurons that do not display frequency preference, responding with higher voltage deflections at oscillations near 0 Hz (Fig. 8B).

According to our previous work it is possible to use the criterion of $Q \geq 1.1$ to define a neuron as resonant. However, we previously showed that this criterion is very restrictive and underestimates the proportion of resonant neurons, since many neurons which does filter slow oscillations have a Q lower than 1.1 and clearly display an impedance profile different from non-resonant neurons ($Q = 1$). Moreover, by studying the distribution of Q values in a large number of ACo neurons, we previously showed that there effectively exist two different populations of neurons, resonant and non-resonant. Therefore, the group with $1 < Q < 1.1$ most probably contains both non-resonant and weakly resonant cells, that cannot be distinguished solely by their Q value.

While restrictive, the criterion of $Q \geq 1.1$ for resonance prevents the erroneous classification of non-resonant (N) cells as resonant (R). However, to explore a possible correlation of Q with other properties (intrinsic and/or synaptic), we grouped neurons with Q between 1 and 1.1 as a separate subset named "mixed" (M) as it may content both types of neurons. Figure 8C shows the distribution of subthreshold behavior for a total of 54 neurons, with a 24 % of non-resonant neurons ($Q = 1$, $n = 13$), 30 % of resonant neurons ($Q \geq 1.1$, $n = 16$) and 46 % of cells in the mixed group ($1 < Q < 1.1$, $n = 25$). These proportions agree perfectly with and corroborate our first characterization of theta-frequency resonance in ACo with 70% of layer II neurons considered non-

resonant and 30% of them being resonant, when using $Q \geq 1.1$ as a criterion for resonance (Vera et al., 2014).

We investigated how different is the impedance profile between the populations of resonant cells (R) and the group formed by both non-resonant neurons (N) and cells falling in the mixed group (M), thus following the most restrictive criterion for resonance in this case. We constructed an average impedance profile for each group (R and N+M). To allow a comparison of the frequency dependence of each curve, we standardized the amplitude of each single impedance profile to the value of impedance at 15 Hz (Figure 8D). This figure shows that at frequencies above 10 Hz both groups of neurons behave identically. However, at frequencies below 10 Hz the average curve of resonant neurons reaches a maximum at ~4.4 Hz, while the curve of N+M neurons reaches its peak near 0 Hz with a relative impedance three times higher than resonant neurons. Note that the higher dispersion of the last curve is consistent with the existence of an undefined number of low resonant cells in the M group. This evident difference in the average impedance profile corroborates that our criterion of classification allows a clear separation in two cell groups to further correlate them with their suprathreshold behavior.

To fully characterize the subthreshold impedance profile of ACo neurons we investigated the histograms of Q values, peak frequencies and peak impedance and obtained average values for each previously defined group: non-resonant (N), mixed (M) and resonant (R, Figs. 8E-G). According to its definition, the average Q for non-resonant neurons is 1, and these neurons contribute with a single peak in the histogram. The average Q values for M and R groups are clearly different with 1.04 ± 0.00 and $1.16 \pm$

0.02, respectively ($p<0.001$, Fig. 8E). The peak frequency histogram shows a peak at 0.5 Hz corresponding to N cells, with an average of 0.51 ± 0.01 Hz. The other points are distributed along the range from 1 to 5 Hz with an average of 2.1 ± 0.2 Hz and 4.0 ± 0.4 Hz for M and R, respectively (all three average values are statistically different, $p < 0.01$). This result shows a relationship between the Q value and the peak frequency.

The histogram of the peak impedance shows that neurons from ACo have this value distributed between 150 and 710 MΩ. Sorting neurons according to its Q value gives an average peak impedance of 401 ± 48 MΩ for N, 305 ± 18 MΩ for M and 282 ± 26 MΩ for R. For this measure there is no statistically significant difference between M and R, while both groups differ from N neurons ($p < 0.01$). This shows that peak impedance is a parameter that separates resonant and mixed group from non-resonant neurons.

As a summary, this data set corroborates the existence and relative abundance of neurons with two kinds of subthreshold behavior in layer II of ACo, resonant and non-resonant. For methodological constrains we classified neurons in three groups, those with $Q \geq 1.1$ as resonant (R), those with $Q=1$ as non-resonant (N) and those with a $1<Q<1.1$ as a mixed group (M) since contains both type of neurons. This allows a further investigation of their suprathreshold behavior.

Relating subthreshold frequency preference to suprathreshold properties

One feature that defines a neuronal type is the way cells fire action potentials spontaneously or under a sustained depolarization, what is called firing pattern (Contreras, 2004). This suprathreshold behavior is the consequence of a complex interplay between several voltage- and ligand-gated ion channels that set the spike

threshold, shape the firing rhythmicity and determine the responsiveness of each cell to a current injection (Bean, 2007). We hypothesize that resonant and non-resonant neurons might have distinctive sets of ion channels and thus have a different suprathreshold behavior. To test this hypothesis we investigated the suprathreshold voltage response of the previously characterized resonant (R) and non-resonant neurons (N).

Firing frequency curve and spike threshold

A rough but robust parameter used to characterize neuron excitability is the firing frequency curve, which is obtained stimulating the neurons with squared current steps of increasing amplitude, and then relating the average firing frequency to each current step (Contreras, 2004). Figures 9A y B shows three recordings from an R and an N neuron, respectively, that where depolarized to different levels to measure their firing response. Despite the difference in the number of spikes fired by these two particular cells under the same current injection, when R and N are grouped and averaged, no difference is observed in their firing frequency curve, contrary to our prediction (Fig. 9C, n=15 and 12 for resonant and non-resonant neurons, respectively). Since the firing frequency is proportional to the level of depolarization and hence to the input resistance (R_{in}) of the cell, we think that the high variability of R_{in} in ACo neurons might produce a variability in the firing frequency curve that hide a possible difference between resonant and non-resonant neurons. While this may or not be true, what is clear is that this parameter does not differ among both groups as it occurs in other neuronal types like semilunar and pyramidal neurons from piriform cortex (Suzuki & Bekkers, 2006), an observation that we corroborated when investigated neuronal resonance in that brain region (Fig. S4).

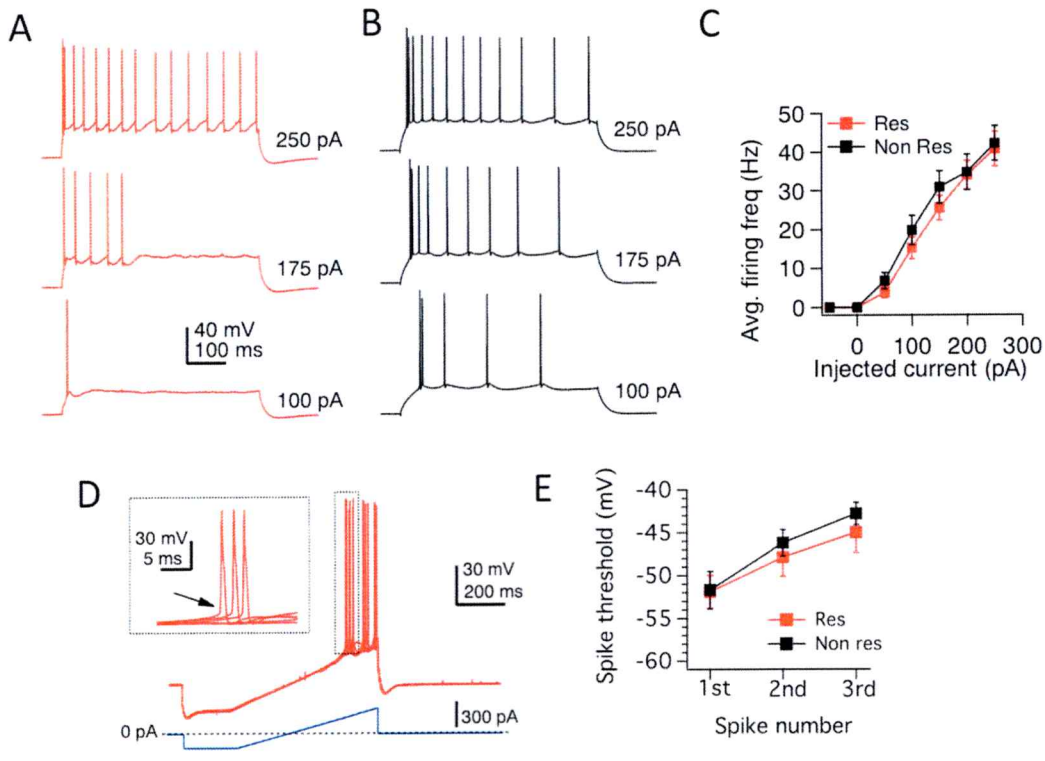

Figure 9. Characterization of firing frequency curve and spike threshold for resonant and non-resonant neurons. A-B Voltage response of resonant (A) and non-resonant (B) ACo neurons to a family of depolarizing squared current pulses of 100, 175 and 250 pA given at -80 mV. C Average firing frequency curves of resonant (red) and non-resonant (black) ACo neurons, constructed with average firing frequencies. D Six superimposed voltage response (red) under a ramp current stimulation (blue) for the measurement of spike threshold. The inset shows spikes in detail. Neurons where held at -80 mV and then, an hyperpolarizing current pulse of -100 pA and 200 ms followed by a depolarizing ramp of 400 pA during 600 ms was applied. E average spike threshold curve for the 1st, 2nd and 3th spikes fired under the ramp protocol for resonant (red) and non-resonant (black) ACo neurons.

The spike threshold is another parameter that reflects the interplay of different ion channels, mostly Na^+ channels types and density in addition to passive properties (Bean, 2007), thus it may reflect differences between these two cells groups.

By definition the spike threshold is the voltage at which the probability to fire an action potential is 0.5, and because of their statistical nature is difficult to measure. Instead we used another, more practical way to measure and compare threshold using a depolarizing current ramp as illustrated in Figure 9D. Starting from a membrane potential of -80 mV neurons were briefly hyperpolarized to ~ -100 mV to reset voltage sensitive channels and then were constantly depolarized with a current ramp at a rate of 0.67 pA/ms during 600 ms. This procedure depolarized neurons above spike threshold and evoked a train of 3 to 6 spikes. As accepted, we measured the spike threshold as the voltage at which its derivative exceeds 5 mV/ms (Shu, Duque, Yu, Haider, & Mccormick, 2007). Using this procedure we found that both, R and N neurons present similar spike threshold for the first spike of the train with -51.9 ± 1.9 mV and -51.7 ± 2.2 mV, respectively. The spike threshold for the second and third spikes of the train showed a more depolarized value, again with no differences between both cell groups (Fig. 9E, for details see legend). This result shows again that there is no big difference in an intrinsic variable between resonant and non-resonant neurons from ACo, challenging the hypothesis that resonant neurons are a defined cell type regarding their general electrophysiological properties (Contreras, 2004).

Nevertheless, each time an intrinsic property is evaluated using a fixed current stimulation, the high variability of ACo neurons passive properties difficult the interpretation of results. Since the voltage response that follows current stimulation

drives the gating for voltage-dependent channels, when a fixed current protocol is used the variability of passive properties (R_{in} and capacitance) is translated into variability in the activation of the channels whose effect we want to measure.

One way to get rid of this variability is to evaluate a parameter or behavior independently of the level of current stimulation, like the firing pattern.

Relating subthreshold resonance with firing pattern

One remarkable property of a subpopulation of ACo neurons is the ability to spontaneously generate subthreshold theta-oscillations of the membrane potential when are depolarized with constant current injection (Sanhueza & Bacigalupo, 2005). These oscillations drive rhythmic firing and have been related to subthreshold resonance in hippocampus and entorhinal cortex (Burton, Economo, Lee, & White, 2008; Chapman & Lacaille, 1999; Erchova, Kreck, Heinemann, & Herz, 2004; Pastoll, Ramsden, & Nolan, 2012), thus suggesting a possible relationship with resonant neurons in the ACo. In addition, previous work of the laboratory described three cell types in layer II ACo according to their firing pattern: 1) tonic firing, neurons that fire spikes with constant frequency during the pulse, corresponding to 38% of cells, 2) Cluster firing, with a response of spikes arranged in clusters with intermingled periods displaying subthreshold oscillations, corresponding to 48% of cells and 3) adapting firing, characterized by a response of highly decreasing firing frequency, corresponding to 13 % of the cells (Sanhueza & Bacigalupo, 2005).

To investigate the relationship between subthreshold frequency preference and these three types of firing patterns, we examined the firing pattern of 43 neurons previously

classified in the N, M or R groups. Neurons where depolarized by constant current injections in order to reach a 5-8 Hz firing rate. By observing the recorded firing patterns we were able to classify cells in one of two groups, tonic or cluster-firing. Cluster-firing (Figs 10A-E) was defined as a firing pattern in groups of actions potentials with brief periods without spikes (but with oscillations), which were clearly distinguishable in the recorded trace, the raster plot and the bimodal distribution of the inter-spike interval (ISI, Fig. 10E). The other firing pattern found was the tonic firing, corresponding to a constant and regular discharge without periods of silence or frequency adaptation (Figure 10F-J). The adapting firing pattern was not observed.

The distribution of the different firing patterns in the three groups of subthreshold frequency preference is shown in Table 1. Note that both described firing patterns occurred at the same voltage range (Figs 10D and I).

Table 1. Distribution of the different firing patterns in N (Q = 1), M (1 < Q < 1.1) and R (Q ≥ 1.1) groups.

	Tonic	Cluster	Total	%
N	6	6	12	28
M	5	13	18	42
R	1	12	13	30
Total	12	31	43	
%	28	72		

From a total of 43 neurons in which the firing pattern was recorded, 28 % was tonic-firing, while the remaining 72 % was cluster-firing, without observation of adapting-firing neurons. From all N neurons (n=12) a half of them were tonic-firing and the other

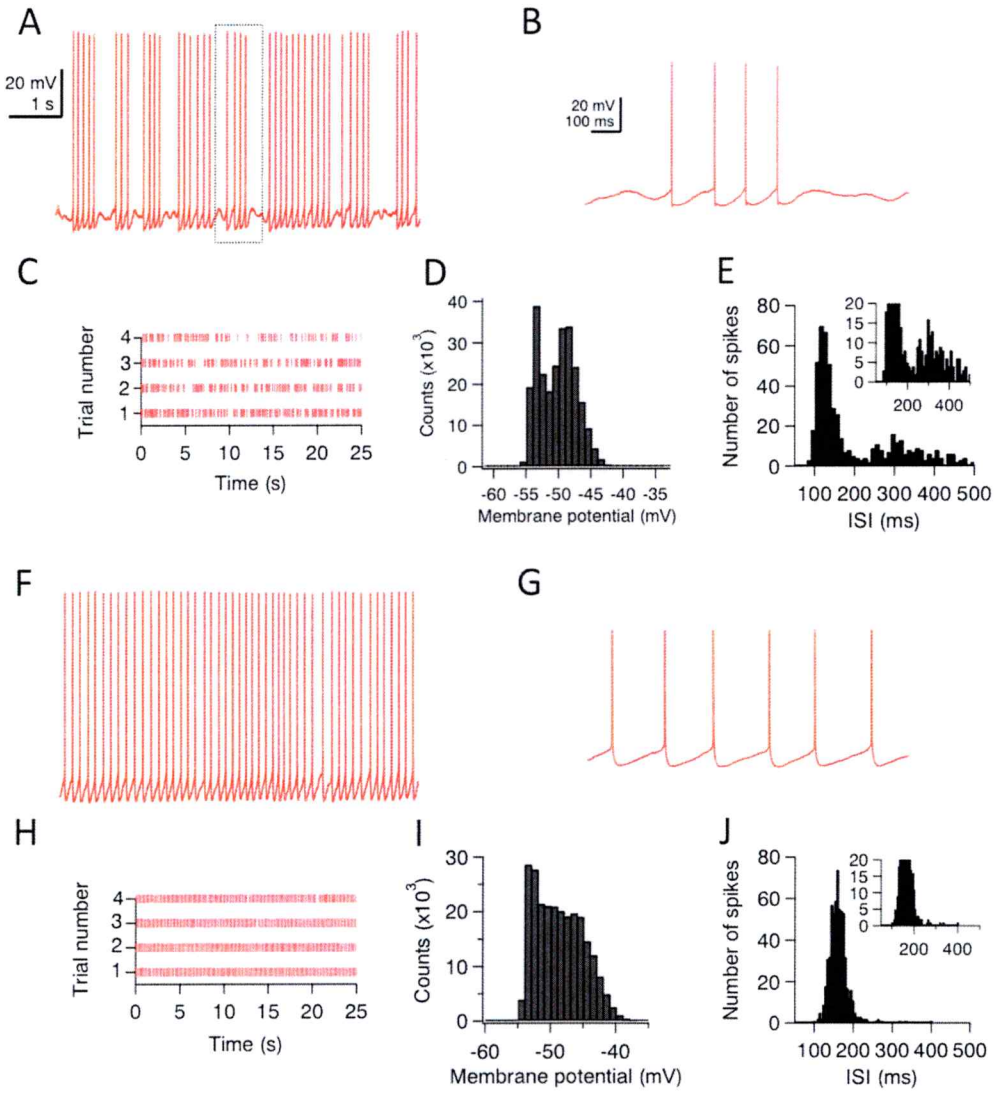

Figure 10. Relating subthreshold frequency preference to firing pattern. A current-clamp recording of a cluster-firing resonant neuron under sustained depolarization to -50 mV using constant current injection. B Zoom of the box-selected region showed in A. C Raster plot showing 100 sec of activity from the cell shown in A. D Histogram of membrane potential from the recording shown in A. E Histogram of the inter spike interval (ISI) extracted from C, the inset show a zoom of Y-axis. F current-clamp recording of a tonic-firing non-resonant neuron under sustained depolarization to -50 mV using constant current injection as in A. G Zoom of the selected region from F. H Raster plot showing 100 sec of activity from the cell showed in F. I Histogram of membrane potential from the recording shown in F. J Histogram of the inter spike interval (ISI) extracted from C, the inset show a zoom of Y-axis.

half cluster-firing. The M group (n=18) had 28% tonic and 72% cluster neurons, while from 13 R neurons all but one were cluster-firing (results summarized in Table 1).

The restrictive criterion of $Q \geq 1.1$ ensures the absence of false-positive resonant neurons, however, it is expected that some neurons that have the intrinsic machinery to resonate only produce a mild filter effect and thus have a Q value below 1.1. Having this in mind it is easier to understand the absence of an exclusive relationship between subthreshold frequency preference and firing pattern. However, taking into account that (R) neurons display almost only cluster firing (12/13 neurons) it is possible to associate this firing pattern with neurons that strongly filter low frequency oscillations.

Medium duration after-hyperpolarization (AHPm) and resonance in ACo layer II neurons.

The possible functional role of neuronal resonance is related to their ability to filter away slow oscillatory synaptic inputs and propagate activity at their preferred frequency (Hutcheon & Yarom, 2000; Izhikevich, 2002). This makes possible that resonant neurons might have a mechanism for action potential generation that is coupled to the subthreshold frequency preference, thus integrating sub and suprathreshold mechanisms toward the generation of a strong and robust frequency-dependent processing of neuronal activity. One component of intrinsic excitability that sets the firing of neurons at determined frequency ranges is the after-hyperpolarization potential (AHP) that follows each fired spike and determines the length of the inter-spike interval (Fernandez & White, 2008; Storm, 1989). Depending on the different voltage and ligand-gated ion channels present in a specific neuronal type, the mechanism of the AHP varies, but it is

normally produced by the activation of several K^+-currents that hyperpolarized neurons (Zhang & McBain, 1995). Depending on the different rates of activation and deactivation of these channels the AHP may contain a fast (AHPf), medium (AHPm) and/or slow (AHPs) components that last in the range of 10, 100 and 1000 ms, respectively (Storm, 1989; Storm, 1987). Since firing frequency at 4-10 Hz (theta range) implies inter-spike intervals (ISI) between 250 and 100 ms, respectively, the AHP related to this timing is the AHPm. In line with this, it has been shown that theta resonant neurons from hippocampus and entorhinal cortex display a robust AHPm, and that its amplitude shapes theta firing (Fernandez & White, 2008; J F Storm, 1989). Therefore, we investigated whether the presence and magnitude of the AHPm might be related to the presence of resonance in ACo neurons and thus being a possible property of resonant cells.

To analyze the AHPm we decided to measure its underlying current under voltage clamp to have a voltage control while evoking the AHPm current (AHPc). The procedure to measure the AHPc is shown in Figure 11A. From a holding potential of -70 mV the AHPc was evoked with a 50 ms depolarization step to 0 mV. The AHPc is observed as a post-stimulus transient outward current that peaks near 10-15 ms after stimulus ends with ~10-20 pA amplitude and decays exponentially with a time constant of ~30 ms (Fig. 11A, control trace) (Sah, 1996). We quantified the magnitude of AHPc as the integral of the trace (the charge) from the time when the trace pass the baseline level after the depolarization pulse, to 200 ms after the pulse. After measuring the AHPc in 7 R and 9 N neurons we found an average value of 1.5 ± 0.7 pQ vs 1.7 ± 0.8 pQ for the

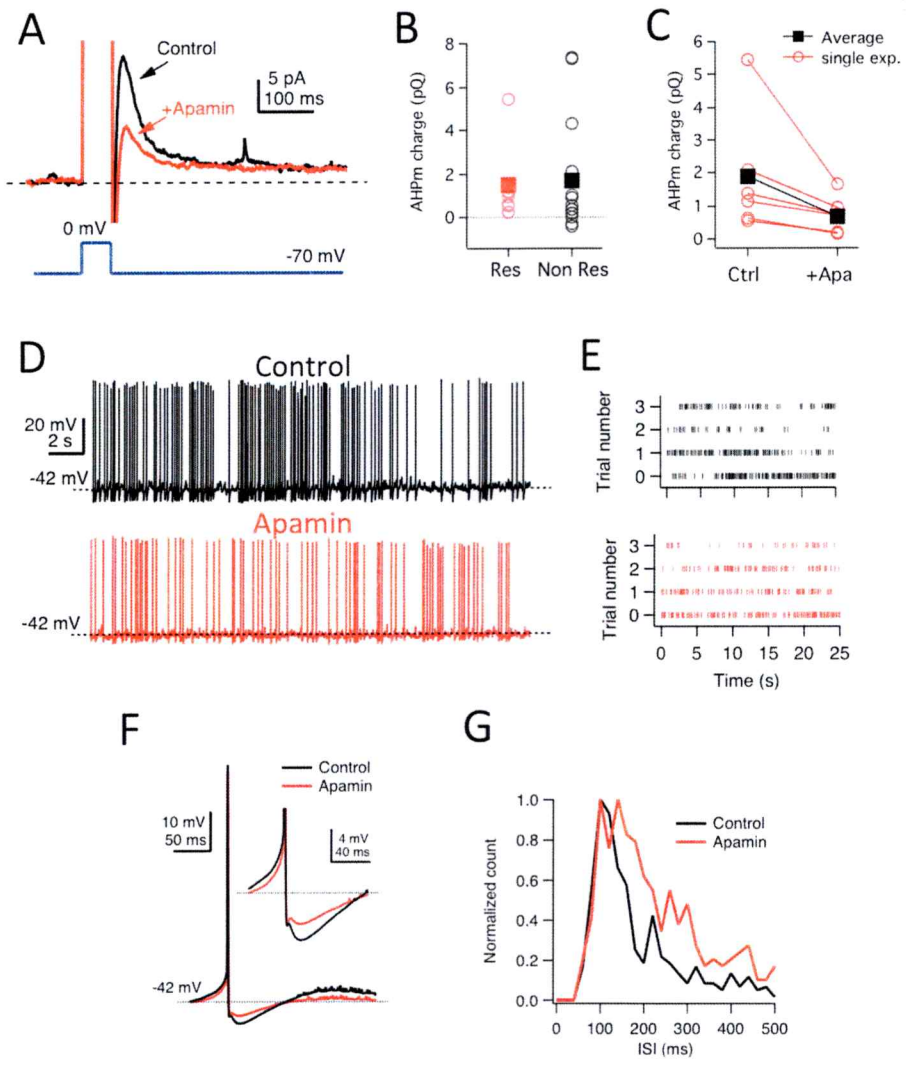

Figure 11. Medium duration after-hyperpolarization (AHPm) and resonance in ACo layer II neurons. A Voltage-clamp protocol to evoke After hyperpolarization potential currents (AHPc). Neurons are held at -70 mV and are depolarized to 0 mV during 40 ms with a squared voltage step. The AHPc is observed as a transient outward current following stimulus depolarization. In the presence of 200 nM of Apamin the outward current is reduced, revealing the contribution of Ca^{2+}-sensitive small conductance SK channels. B Whole AHPc contribution measured as the transported charge (integral of current trace) in resonant and non-resonant neurons. C Measurement of SK channel contribution to AHPc in resonant neurons (For more details see the text). D Membrane potential of a cluster-firing neurons in control condition (black) and after the addition of Apamin (red). E raster plot of recordings in D. F Average action potential waveform extracted from recordings in D. G Distribution of the inter spike intervals extracted from recordings in G.

mobilized charge (Fig. 11B) and 40.4 ± 7.9 ms vs 49.6 ± 8.2 ms for the time constant (not shown), respectively, with no statistically significant differences between neither of them (p=0.39 and 0.46, respectively). Besides this average result, the quantification of the AHPm showed a high variability within each cell group. Discarding the cells that have an AHPc near cero (mostly non-resonant, Fig. 11B), the high variability might be related to the amount of channels in each neuron that obviously will vary according to cell size. This variability thus hinders a possible differentiation between the compared resonant and non-resonant neurons based on their AHPm.

Continuing with the investigation of suprathreshold features of resonant neurons we went one step forward to investigate the contribution of SK channels to the AHPm in these neurons (Villalobos, Shakkottai, Chandy, Michelhaugh, & Andrade, 2004). The depolarization triggered by action potentials produces bouts of calcium entrance that transiently increments the intracellular concentration and serves as second messenger (Bading, Ginty, & Greenberg, 1993; West et al., 2001), controlling metabolic processes and gene expression in a process described as the excitation-transcription coupling (Dolmetsch, 2003). The restoration of intracellular calcium concentrations depends on the repolarization of the membrane potential that closes voltage-sensitive channels and stops calcium entrance. A key step in this repolarization is the activation of Ca^{2+}-sensitive K^{+}-currents that act as a feedback loop (Bond, Maylie, & Adelman, 2005). SK channels are small-conductance, highly Ca^{2+}-sensitive and voltage-insensitive channels whose opening and underlying current follows the rise and decay of intracellular Ca^{2+} and thus serves as an indirect way to evaluate Ca^{2+} changes during firing process

(Martin Stocker, 2004). Furthermore, since Ca^{2+} clearance lasts in the range of tens of ms, the SK-current may contribute to AHPm and with that, to firing in theta frequency.

We evaluated the contribution of SK-current to the AHPc in resonant neurons using the selective SK channel blocker apamin (M Stocker, Krause, & Pedarzani, 1999). Following the same experimental procedure described above, we measured the AHPc charge after and before the addition of 200 nM of apamin (Fig 11A), observing that it produced an average reduction of 60% in the charge, from 1.9 ± 0.8 pQ to 0.7 ± 0.2 pQ ($n = 6$, $p < 0.05$, Fig. 11C). This result shows that resonant neurons from ACo layer II have a SK-current that contributes to 60% of the AHPc, and indirectly shows that these neurons have a calcium entrance coupled to the firing of action potentials and hence may present excitation-transcription coupled processes.

Finally, since the AHPm drives the rhythmicity of intrinsic firing pattern we investigated the contribution of SK-current and their underlying Ca^{2+} entrance, on the cluster-type firing of resonant neurons. We characterized the cluster firing pattern before and after the bath addition of 200 nM apamin. In control conditions neurons showed the previously described stuttering behavior (Fig 11D) with a skewed distribution of inter-spike intervals with at maximum near 120 ms (ISI, Fig 11E). After the blocking of SK channels, the general appearance of the firing pattern is not altered, displaying similar pattern of activity observed in both the row recordings and raster plots (Fig. 11D-E). However, the observation of the action potential waveform confirm the reduction of the AHPm and a variation in the ISI histogram, as was expected (Fig. 11F-G), but without a dramatic effect on the firing pattern.

The overall conclusion from these experiments is that resonant neurons from layer II ACo have a strong AHPm, which is in agreement with their theta-range firing pattern. Moreover, an important fraction of the AHPc is carried by SK-channels, confirming the Ca^{2+} entrance after excitation and their possible implication in excitation/transcription coupling.

Relating subthreshold frequency preference to cell morphology: Characterizing ACo cytoarchitecture

By far the most striking and notorious feature of a given cell type is their cell morphology. Since the times of Ramon y Cajal neuroscientists have described tens of different neuronal morphologies, that faithfully identify specific groups of neurons that share in common other physiological properties, by reporting the shape of the soma, the disposition and size of dendrites and, in some cases, axon arborization (Fiala, Spacek, & Harris, 2008). Regardless of an expected variability in morphology inside a given neuronal type, some common patterns emerge as a fingerprint, like the laminar disposition of the soma, dendrites and axon, the shape of the soma, the presence of predominant dendrites, the direction and extension of dendrites, the times each main dendrite branches, and like these, one can mention many other visually descriptive criteria that allow morphology description (Fiala et al., 2008).

In this way, resonant neurons from hippocampus and entorhinal cortex have been described in detail. Pyramidal neurons from CA1 are very similar, all of them with the soma in the layer called *stratum piramidale*, with a pyramidal shaped soma (15-20 μm major diameter) that ends in a principal dendrite (main dendrite) that extends near 700

μm, reducing its diameter with its distance from the soma. Arborizing secondary and tertiary dendrites are located on *stratum radiatum* and *stratum lacunosum moleculare* layers. At the opposite extreme of the soma, 3-6 basal dendrites arise and extend near 200 μm into the *stratum oriens*. All resonant neurons from CA1 hippocampus meet this description (Spruston & McBain, 2007). Resonant neurons from entorhinal cortex, the stellate cells, are located in layer II, have a large pyramidal soma with two or three principal neurons that are heavily branched. Again, all stellate neurons meet this description (Klink & Alonso, 1997). Of course, both of these resonant neuronal types are intermingled with several different neuronal types in their respective brain regions, CA1 pyramidal neurons share their layer with multiple types of interneurons and stellate neurons are in between interneurons (Spruston & McBain, 2007), and pyramidal neurons of layer II entorhinal cortex (Canto, Wouterlood, & Witter, 2008).

With the aim of characterizing the morphology of resonant and non-resonant neurons, and with this, probably find different neuronal types, we used 0.1% of biocytin in the intracellular solution to label each recorded neuron. Immediately after recording each brain slice was fixed and neuronal morphology was obtained with a standard method based on diaminobenzoic acid (DAB) reaction (see Methods). Throughout the development of this thesis we were able to characterize the morphology of a total of 45 neurons, 21 resonant and 24 non-resonant. Figure 12 shows a reconstruction of ACo cytoarchitecture using a selection of the best-resolved morphologies (14 resonant and 17 non-resonant, tagged with an R and an N, respectively). This reconstruction was made faithfully describing the position of the soma and dendrites distribution in the different layers. By observing Figure 12, the first impression is the impossibility of finding any

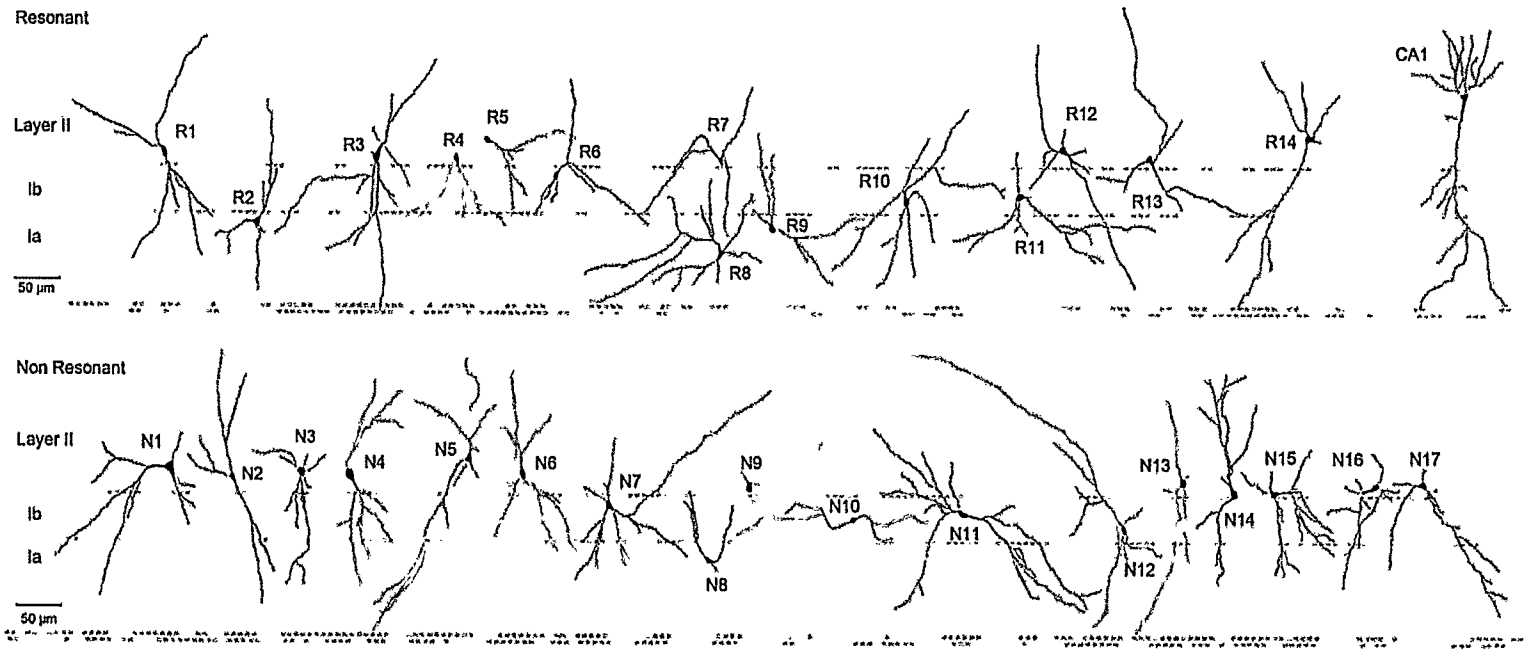

Figure 12. Cytoarchitecture of the anterior cortical amygdala nucleous (ACo) separating resonant and non-resonant neurons. Selection of 14 resonant (R1-14, $Q \geq 1.08$) and 17 non-resonant (N1-17, $Q = 1$) from a total of 45 ACo neurons recorded with intracellular solution containing 0.1% of biocytin. After recordings slices were fixed and then morphology was revealed using DAB-based reaction. The layer position of each neuron was reconstructed based on their actual position.

clear difference between resonant and non-resonant neurons, which resulted quite astonishing. There is no a characteristic soma shape or location, nor a typical dendritic branching. Within both groups we found neurons with small-rounded somas (R5, 6, 9, 11 and N3, 9, 10, 13), and also cells with pyramidal somas with a sort of main apical dendrite oriented to different directions (R2, 3, 8, 12 and N1, 2, 4, 11, 12, 14, 16). In general ACo cytoarchitecture is characterized by isodendritic neurons with no dendrites biased towards any particular layer, this is true for both resonant and non-resonant neurons (R1, R2, R3, R10, N2, N5, N6, N11, to name some). Particularly striking is the presence of a couple of neurons with dendrites polarized toward layer Ia resembling PC semilunar neurons (R4, R11, also called extraverted), typical cellular type present in layer II of the main olfactory cortex that we described as non-resonant (unpublished data, Fig. S4).

The major conclusions that can be obtained with this characterization are as follows. ACo does not have a main principal cell type (or morphology), as is observed in other three layered cortical regions like the hippocampus or piriform cortex (L. Haberly, 1998; Spruston & McBain, 2007). The morphological heterogeneity observed in ACo highlights its structure of cortical nucleus rather than an ordered laminar cortex as described in the literature for the piriform cortex (L. Haberly, 1998). Furthermore, most of the neurons from layer II, both resonant and non-resonant, extend dendrites to all the three layers of ACo, suggesting an anatomical connectivity of each neuron with the different ACo afferences (olfactory bulb, cortical association axons and other brain regions). Finally, there is no clear morphology than can be related neither to resonant, nor to non-resonant neurons from ACo.

Characterization of synaptic properties of layer II ACo neurons

After characterizing basic intrinsic properties and morphology of neurons from layer II of ACo we went to describe the synaptic properties of these neurons, always with the idea of finding any property that could distinguish resonant neurons from non-resonant neurons and that may help us to understand or propose a functional role for subthreshold frequency preference in this region.

ACo has two interesting aspects that place it as a possible privileged model for studying neuronal resonance. First, the simplicity of the main synaptic inputs that it receives. It has been described that the main input of ACo is the OB, which sends its projections to the different olfactory cortical regions (which include PC, entorhinal cortex, and cortical amygdala) through the olfactory tract and then through the layer Ia (L. Haberly, 1998). In the intact brain this pathway conducts strong oscillatory activity in theta range, which has been described in detail as synaptic inputs to the PC (Cang & Isaacson, 2003; Desmaisons, Vincent, & Lledo, 1999; Kajiwara et al., 2007; Smear, Shusterman, O'Connor, Bozza, & Rinberg, 2011). From the OB the signals reach directly the ACo, which serves as a gate for olfactory signals to enter into the BLA for further processing and elaboration of emotional response (McDonald, 1998). Contrasting with that simplicity, other models of neuronal resonance, like the hippocampus or entorhinal cortex, have the additional difficulty that in the intact brain these areas process multimodal sensory signals (from most sensory modalities) (Ahmed & Mehta, 2009; Canto et al., 2008), thus receiving complex oscillatory inputs which have not been described in detail so far, and hence make it difficult to test whether resonant neurons

express their frequency preference while process them. Nonetheless, since the ACo is a scarcely studied brain region, we first attempted to confirm the neuroanatomical projections from the OB to the olfactory cortex, with emphasis on the ACo.

The second aspect that places the ACo as a privileged model for our purposes is related to the functionality of the preserved collaterals in the layer Ia of acute coronal slices. This means that those axons collaterals are sensitive to electrical stimulation and allows an easy rhythmic drive of postsynaptic potentials in ACo neurons while are recorded in whole-cell configuration (Sanhueza & Bacigalupo, 2005). However, it is not known whether resonant neurons receive or not inputs from the OB and if the dynamics of synaptic activity integration will support the transmission of theta-frequency rhythmic inputs without a disruptive effect of synaptic facilitation or depression. If this is the case, the ACo will serve as the first experimental model allowing the direct evaluation of the processing of realistic rhythmic synaptic inputs in resonant neurons. These questions were addressed in this thesis and are described below.

Confirming neuroanatomical projections from the olfactory bulb

To confirm that the OB projects collaterals to the ACo we injected the anterograde neuronal tracer PHAL (Phaseolus vulgaris leuco-agglutinin) unilaterally in the left hemisphere of the OB of rats and evaluated the presence of the tracer in ACo after five days of migration. Figure 13 shows a coronal brain section where PHAL was detected by immunoreaction and then counterstained with Nissl to locate the position of the somas. This procedure allowed the observation of the tracer as a diffuse gray shadow mark that can be distinguished from the blue background. Figure 13A shows a section of

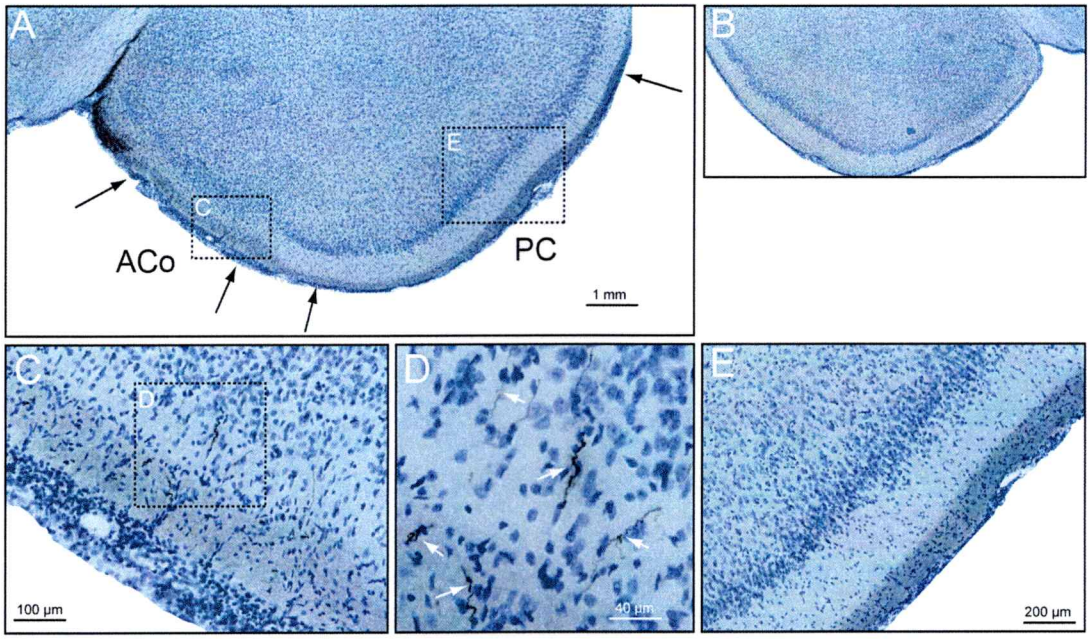

Figure 13. Confirming anatomical projections from the olfactory bulb. Axons from the olfactory bulb project to the anterior cortical amygdala. Experiment to study the projections of the olfactory bulb to the amygdala and other cortical olfactory cortices. Was injected in tracer PHAL anterograde (Phaseolus vulgaris leuco-agglutinin) in the left hemisphere of the olfactory bubo of an adult rat. Five days post injection the animal process. The presence of PHAL was obtained by immunodetection / DAB then a Nissl staining was performed. Cross section (50 microns) to anteroposterior level including cortical amygdala appears (is corroborated by the level of penetration and shape of the optic tract) A lower Region of the left hemisphere (ipsilateral to the injection site) showing brand PHAL along entire Ia (light gray, outermost layer) layer, via the piriform cortex (PC) and amygdala cortical (CA), but not the in the layer Ib. It can be compared with the layer of non-injected hemisphere (right) showing no presence of the tracer (B). C Increased image A corresponding to the cortical amygdala, which lets you see more detail PHAL brand presence in the layer and the presence of axons in layer Ib. D Enlargement of C, axons present in the layer Ia and Ib are shown with white arrows. E Expansion image corresponding to the piriform cortex (PC) where you can see the mark of PHAL in the layer A, but the absence of axons that innervate deeper layers (Ib and / or II).

the injected hemisphere, which has a dark shadow mark along the whole layer Ia (the outermost layer, compare with Figure 13B that shows the non-injected hemisphere without tracer mark). Arrows show both olfactory cortices, ACo and PC. This diffuse mark shows that layer Ia presents passing collaterals from the OB all along ACo and PC. Higher magnification of the microphotography shows putative OB axons invading layers Ib and II only in the ACo, and thus possibly making synaptic contacts (Figure 13C and D). By striking contrast, the PC presents a complete absence of collaterals invading layer Ib or II (Figure 13E).

These results confirm that axons from OB effectively pass through the entire layer Ia of olfactory cortex and invade interior layers specifically at ACo. This allows the stimulation of synaptic terminals onto ACo neurons in the coronal slice by means of electric stimulation of layer Ia, in order to recreate rhythmic OB activity. In addition, it is interesting that the distribution of axonal projections show differences between PC and ACo that, to our knowledge, have not been previously described.

Spontaneous synaptic activity onto ACo neurons

The synaptic activity in a neuronal network is determined by the temporal summation of the individual synaptic events. Unitary synaptic events will vary in amplitude and frequency depending on brain region, being characteristic of it. For example, in CA1 pyramidal neurons an typical miniature event (recorded in the presence of TTX to block spike-evoked synaptic events) will have an average amplitude of 20 pA (when recorded in voltage clamp, and near 0.5 mV under current clamp) and a frequency close to 1 Hz. In turn, in the PC, superficial pyramidal neurons have an amplitude near 10 pA and a

frequency near 5 Hz, thus showing functional and structural differences with the neurons from the hippocampus. In this way, the amplitude and frequency of the events provide information on the synaptic physiology of the circuit.

To characterize the spontaneous synaptic activity from layer II ACo neurons we recorded postsynaptic currents under voltage-clamp configuration at a holding potential of -80 mV. Since that membrane potential is hyperpolarized respect to reversal potential for Cl^- ions, GABA-ergic (inhibitory postsynaptic currents, IPSC) and glutamatergic (excitatory postsynaptic currents, EPSC) postsynaptic currents are observed as inward currents (downward deflections, Fig. 14A-C). The analysis of these experiments showed that ACo neurons have spontaneous synaptic events with an average frequency of 3.1 ± 1.4 Hz and amplitude of 22.2 ± 2.3 pA (n=10). We compared the values between resonant (n=3) and non-resonant (n=7) neurons and found no difference for frequency or amplitude of spontaneous synaptic events, reason by which all data was pooled together. It is important to note that for these experiments we did not use TTX, thus the recorded events correspond to a sum of miniature events and spike-evoked synaptic events. However, given the low amplitude of the recorded events they most probably represent mainly miniature synaptic events. In addition, these neurons do not display spontaneous firing when recorded, and in this preparation (acute slice) most of the afferences are not present, thus it is expected that the spontaneous level of spiking-driven synaptic events in the slice preparation remains low, almost negligible. Therefore, the values obtained for the amplitude and frequency serves as a first preliminary characterization of synaptic events in layer II ACo neurons.

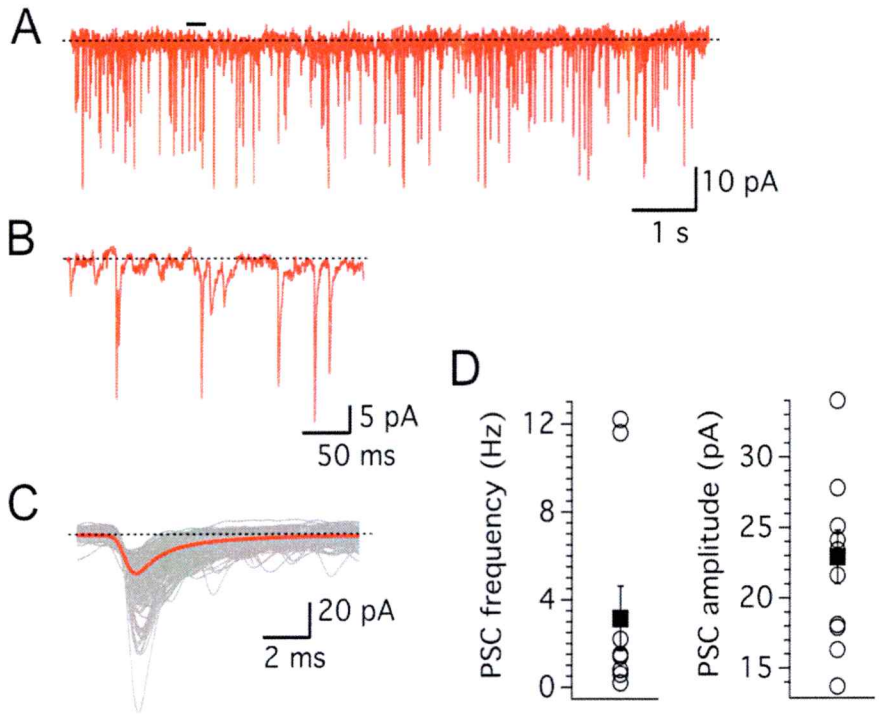

Figure 14. Characterization of spontaneous synaptic activity of layer II ACo neurons. The spontaneous synaptic activity was recorded in voltage-clamp mode by holding the membrane potential at -80 mV. A Representative recording in standard condition of whole-cell membrane currents in an ACo neuron showing spontaneous synaptic activity as downward deflections of different amplitudes. B Zoom from a selected region from recording shown in A with a black bar. C Overlay of events detected on 30 seconds of recording (including that shown in A), the average waveform is showed in red. D Frequency and amplitude of spontaneous events recorded in 11 ACo neurons. Circles and squares represent individual experiments and the filled symbols the average values.

Evoked synaptic activity through stimulation of afferent projections

Since PC is a well-described olfactory cortex, we used it as a reference to conduct and compare our exploration of evoked synaptic activity on layer II ACo neurons. Evoked synaptic activity on PC layer II neurons through electric stimulation shows differences depending on whether layer Ia or Ib are stimulated: a faster synaptic response is evoked by stimulation in layer Ib (Franks & Isaacson, 2005). It has been shown that associational (intracortical) projections localized to layer Ib reach layer II neurons near the soma, thus reaching the soma faster and with little attenuation caused by dendritic filtering. Projections from layer Ia contact layer II neurons at a dendrite site distal from the soma, thus synaptic potentials have larger delay and increase time to peak when measured at the soma due to dendritic filtering (Franks & Isaacson, 2005).

Considering this information and with the idea of characterizing the functionality of the inputs from OB to layer II ACo neurons, we evaluated three putative synaptic pathways. Figure 15A-C show photomicrographs of the configuration used in these experiments indicating the position of stimulation and recording electrodes. Three stimulation electrodes where settled in layers Ia, Ib and II/III at a neighboring region to ACo (PC/ACo transition region, PAx), in order to avoid direct stimulation of layer II ACo neurons. The stimulating electrode identified as No. 1 was placed in the outermost region, layer Ia (Fig. 15A), to stimulate OB collaterals (Fig. 15B). Layer Ib is the layer right above layer Ia (see Fig. 15A) and electrode No. 2 was placed here to stimulate associational connections (Fig. 15B). A third electrode was placed in layer II/III to stimulate projecting fibers from PC into ACo (Fig. 15B). Figure 15C shows the recording pipette distant at least 400 μm from the stimulation electrode array.

The characterization of evoked synaptic responses triggered by the stimulation of different electrodes was made in voltage-clamp configuration, holding the membrane potential at -80 mV and increasing the amplitude of the stimulation current in order to produce an observable synaptic event. Figure 15D shows recordings obtained from a representative neuron. Most recorded neurons (10/11) showed evoked synaptic activity when stimulated trough any of the electrodes located in layer Ia, Ib or layer III. Only one neuron displayed a sort of layer selectivity without showing evoked response to stimulations in layer Ib (not shown). We aimed to evoke events with comparable amplitude at each layer, but this was difficult to achieve due to a steep relationship between stimulation intensity and evoked response amplitude. Despite the difference in amplitude, which is controlled by the intensity and position of the stimulation electrode, the comparison of the normalized responses shows clear differences in the temporal course of the evoked events at each stimulation site (Fig. 15D right). To quantify these differences we measured the time to peak, decay time, delay, and peak amplitude for all neurons (Fig. 15E). The time to peak, which is related to the degree of dendritic filtering, was 3.1 ± 0.5 ms, 2.6 ± 0.5 ms and 3.5 ± 1.0 ms for electrodes at layer Ia, Ib and II/III, respectively. The decay time, also related to dendritic filtering, was 5.1 ± 1.0 ms, 4.7 ± 0.6 ms and 6.8 ± 2.0 ms for stimulations at layer Ia, Ib and II/III. The delay time measured from the stimulation artifact to the onset of the synaptic response was 2.9 ± 0.5 ms, 3.6 ± 0.3 ms and 3.6 ± 0.2 ms for layers Ia, Ib and II/III, respectively. The amplitude of the synaptic response was 53.8 ± 13.6 pA, 33.5 ± 5.7 pA and 98.1 ± 40.9 pA for layers Ia, Ib and II/III, respectively. Even though average values show a trend suggesting that the electrodes evoked different synaptic events, and thus that they were

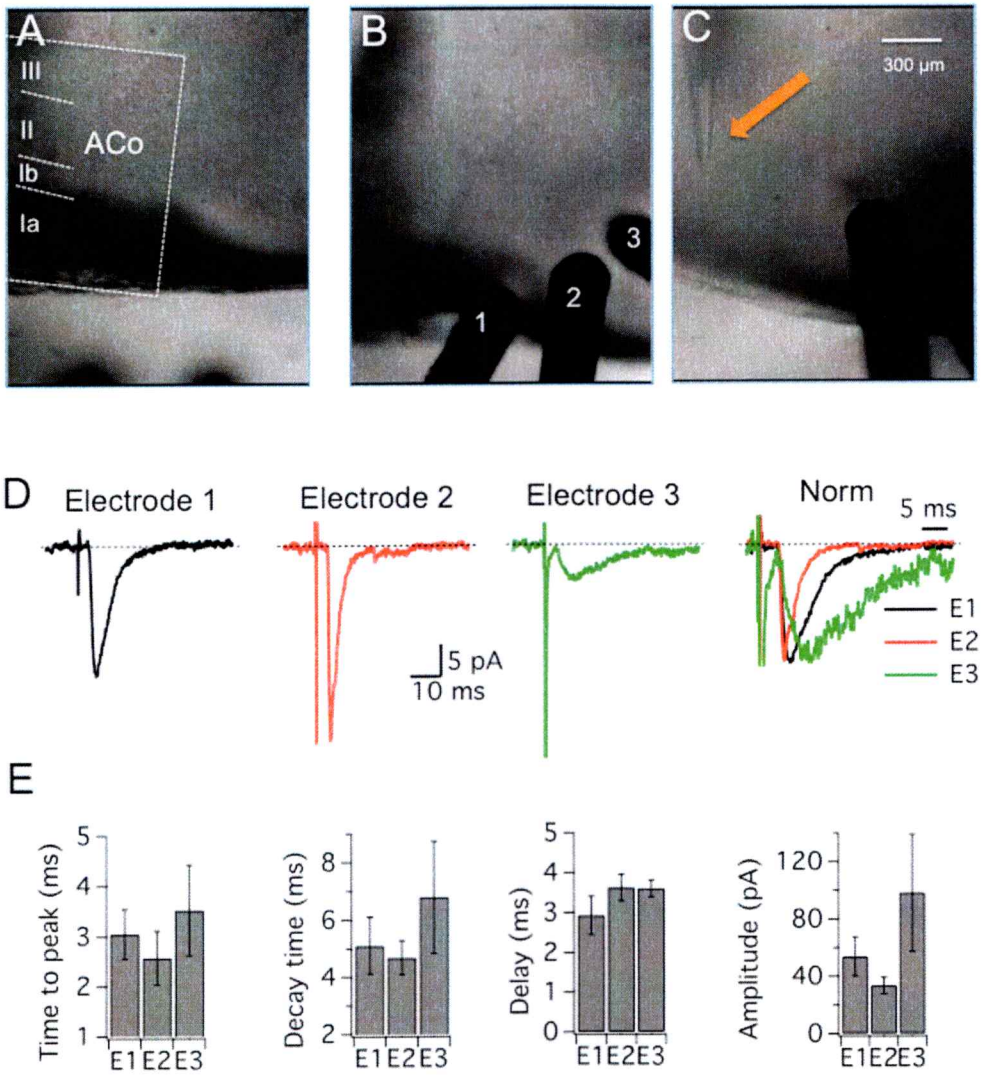

Figure 15. Characterization of evoked synaptic activity of layer II ACo neurons. A Photomicrograph showing the layer distribution of ACo in the slice preparation. B position of stimulation electrodes in the same slice showed in A. C Position and relative distance (≥400 µM) between stimulation and recording (arrow) electrodes, note that this is a different slice. D Whole-cell evoked currents according to stimulation at layer Ia (electrode 1), Ib (electrode 2) and layer II / III (electrode 3), and their normalized overlay (right). E Quantification of synaptic evoked responses according to stimulation layer.

stimulating different afferent pathways, the high variability of obtained values hinder a statistically significant differences between any of them. We think that the source of variability that occludes the significance of our results lies on the high heterogeneity of cell morphologies that characterize ACo layer II cytoarchitecture (described previously). The uneven dendritic branching of each neuron through the different layers (Fig. 12) should produce variability in the synaptic response under stimulation with an extracellular electrode, even when the same afferent pathway is compared (i.e. same layer).

Notably, the relationship of average values of time to peak and decay time agrees with the trend described in the in PC for specific layer stimulation (Franks & Isaacson, 2005). The activity evoked in pyramidal neurons of PC by stimulation of layer Ia has a higher time to peak and a higher decay time relative to layer Ib, which is the same relationship we found. This data support the idea that the synaptic afferences to ACo maintain the organization described to the PC, with the OB projections going through layer Ia and associational projections through layer Ib.

Despite the fact we did not identified differences in the synaptic response to stimulations at each cortical layer, we found very interesting results allowing us to achieve the goal of characterizing the synaptic connectivity of ACo neurons preserved in the coronal slice. Now we know that ACo has a high degree of connectivity with axonal projections coming through layers Ia, Ib and II/III, making synaptic contact with practically all neurons from layer II. Importantly, the fact that this connectivity is preserved in the coronal slice allows an easy and selective activation through a stimulation electrode.

Characterization of rhythmic synaptic transmission in layer II ACo neurons

Once was confirmed the anatomical and electrophysiological connectivity of ACo layer II neurons, we characterized the response of these neurons to a rhythmic stimulation of layer Ia fibers in order to assess the frequency-dependent performance of these synapses. We studied the response to two distinct types of stimulation. First, we used a stimulus composed of six single pulses with an inter-stimulus interval corresponding to a frequency in the range of 0.5 to 12 Hz, that we called "theta stimulation". The other mode of stimulation consisted of a nested theta-gamma stimulus, comprising triplets (a burst of three pulses at 60 Hz) applied 4 times at an inter-triplet interval varying in order to span the range of 0.5 to 12 Hz. That stimulation was called "theta-gamma stimulation". This nested stimulation was chosen because it reproduces *in vivo* activity patterns observed in OB and PC (Cang & Isaacson, 2003; Wilson, 2001).

Frequency-dependent response under synaptic stimulation

The result obtained with the theta stimulation is summarized in Figure 16. Each frequency was studied by applying a train of six stimuli with the exception of 0.5 Hz, which consisted of only 4 stimuli to reduce the time of the recording (Fig. 16A). Note that in Figure 16A the trace between each pulse was removed for 0.5 - 2 Hz to allow the same temporal scaling. Each train of stimuli was applied six times, with a resting time of 2 s between each application to allow the restoration of basal synaptic levels. We quantified the synaptic response by measuring the peak voltage amplitude of each synaptic response.

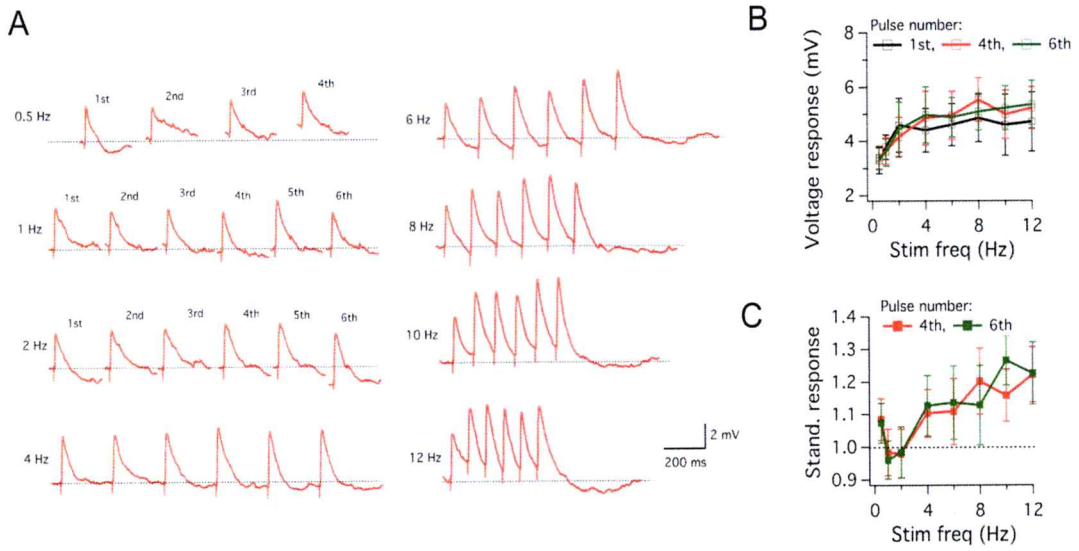

Figure 16. Characterization of evoked synaptic responses of ACo neurons under theta rhythmic stimulation of layer Ia. A Representative voltage response of an ACo neuron under theta rhythmic stimulation protocol. The neuron was held at -80 mV by injecting a constant current. Stimulation was performed at the intensity needed to evoke 5 mV peak responses at frequency of 0.5, 1, 2, 4, 6, 8, 10 and 12 Hz. Stimulation protocol consisted in applying a train of six pulses at intervals determined by the desired frequency, except the frequency of 0.5 Hz, in which only four pulses were applied. For each frequency the train was repeated 6 times and the average trace was analyzed. B Amplitude of the peak voltage response for the 1st (black), 4th (red) and 6th (green) stimulation pulse of the train given at each studied frequency (mean ± standard error, n = 11). C Amplitude of the peak voltage response for the 4th (red) and 6th (green) pulses normalized by the amplitude of the 1st pulse of the train.

The idea behind this experiment is that the first pulse of the train always will be independent of the train frequency, since it is preceded by 2 s of resting. Therefore, any change in the amplitude of the 1st pulse will indicate frequency-independent processes. By contrast, the following pulses in the stimulus train are evoked within the studied frequency regime, and thus will express frequency-dependent processes, including short term synaptic facilitation or depression. Figure 16B shows the amplitude of the response evoked by the 1st, 4th and 6th pulse of each train as a function of stimulation frequency. For this quantification, resonant (n = 4) and non-resonant neurons (n = 7) where averaged together because of their lack of differences. Figure 16B shows a sustained increase in the amplitude responses as frequency rises from 0.5 to 4 Hz. Since this increase of evoked amplitude occurs in the 1st pulse, which we said is frequency-independent, and taking into account that the 4^{th} and 6^{th} pulses also display the increase of amplitude, we think that such increase is due to the stabilization of intracellular condition after obtaining the whole-cell configuration. To investigate frequency-dependent changes we normalized the 4th and 6th pulses by the amplitude of the first pulse, thus getting rid of baseline changes. This procedure revealed an increase of the evoked amplitude proportionally to stimulation frequency, rising up to 20% at 12 Hz. Since this increase of amplitude is observed for stimuli above 2 Hz (implying inter-pulse times lower than 500 ms), it might be related to presynaptic facilitation processes.

Interestingly, this result demonstrates that layer II ACo neurons have a synaptic response able to process theta frequency stimulation without a strong depression that could filter out theta rhythmic input at synaptic site before intrinsic properties were allowed to be expressed. Therefore, resonant neurons from ACo have the synaptic machinery to

receive theta-rhythmic layer Ia activity allowing a possible intrinsic frequency-dependent processing.

Frequency-dependent response under nested theta-gamma stimulation

As a final step of this synaptic characterization we assessed the ability of ACo neurons to receive synaptic stimulation under a mixed theta and gamma frequencies regime, as described in *in vivo* preparations. We stimulated layer Ia using nested theta-gamma protocol composed by 4 pulses at varying theta frequency, with each pulse consisting of a fixed 60 Hz triplet. The quantification of each response was performed measuring the peak amplitude of the third triplet at each evoked response. Note that in Figure 17A the trace between each pulse was removed for 0.5 - 2 Hz to allow the same temporal scaling. The 60 Hz triplets produce a summation of unitary responses in a nonlinear way, with a depression of the second and third responses relative to the first in each triplet. The complex synaptic responses generated by each triplet last ~200 ms and there is no observable change between them in trains from 0.5 - 4 Hz. At frequencies above 4 Hz responses to triplets begin to overlap, changing the baseline to the next triplet. While the amplitude of the 1st triplet (measured after the third pulse) is stable across all theta-frequencies, the peak amplitude of the 4th triplet decreases at frequencies above 4 Hz (Figure 17B). To isolate frequency-independent effects we normalized the 4th triplet amplitude by the 1st triplet amplitude (Figure 17C). This procedure reveals an almost sustained reduction in the evoked response down to 20% and 60 % for 6 and 12 Hz, respectively.

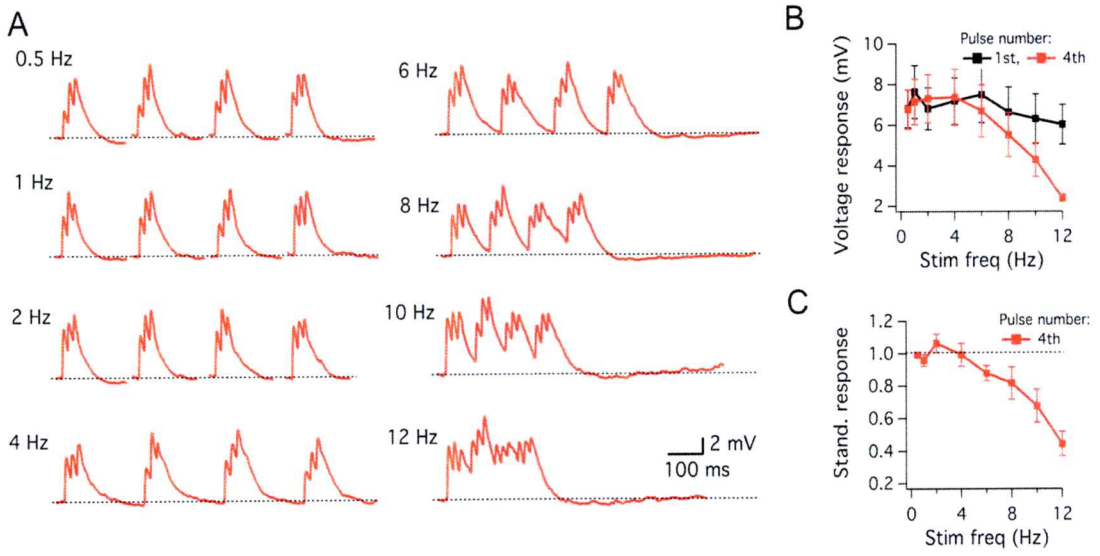

Figure 17. Characterization of evoked synaptic responses of ACo neurons under theta-gamma rhythmic stimulation of layer Ia. A Representative voltage response of an ACo neuron under theta-gamma rhythmic stimulation protocol. The neuron was held at -80 mV by injecting a constant current. Stimulation was performed at the intensity needed to evoke 5 mV peak responses at frequency of 0.5, 1, 2, 4, 6, 8, 10 and 12 Hz. Stimulation protocol was a train of four fixed 60 Hz triplets at intervals determined by the desired theta frequency. For each theta frequency the train was repeated 4 times and then was averaged for analyses. B Amplitude of the peak voltage response corresponding to the last stimulus in each triplet for the 1st (black) and 4th (red) stimulation triplet of the train given at each studied frequency (mean ± standard error, n = 11). C Amplitude of the peak voltage response for the 4th triplet normalized by the amplitude of the 1st triplet of the train.

This frequency-dependent processing shows that ACo neurons have the synaptic dynamics needed to receive synaptic stimulus in a nested theta-gamma frequency.

Comparison between theta and theta-gamma synaptic response

Figure 18 summarizes the differential effect observed in ACo neurons by stimulating afferent olfactory pathway with two types of stimuli that resulted in a very different evoked response. On one hand, the application of a simple stimulus produces a frequency-dependent increase of amplitude (Fig. 18A-B, top). However, by replacing the single pulse with a 60 Hz triplet and thus generating nested theta-gamma stimulation, there was an entirely opposite effect, producing a frequency-dependent decrease of peak amplitude. This differential effect is clearly seen when the two normalized curves are superimposed (Fig. 18C).

Although this result lets many unanswered questions related to the underlying mechanism, its robustness shows something very interesting. First, the possibility to differentially activate ACo neurons when stimulated at theta and theta-gamma frequencies. Second, because we were able to get measurable and reproducible responses at the soma, even after synaptic and dendritic filtering, allows to design suitable experiments to investigate the impact of intrinsic frequency preference and evaluate a differential processing of realistic synaptic inputs. The protocols should more reliably reproduce the massive and coherent excitatory and inhibitory inputs that a neuron receives during theta network activity.

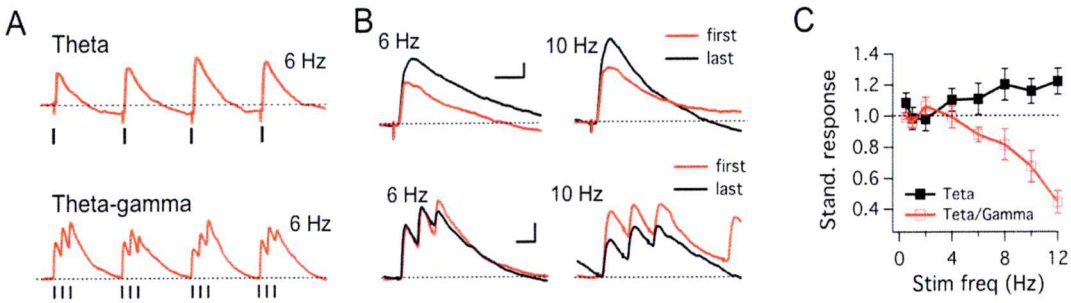

Figure 18. Differential response of ACo neurons to theta or theta-gamma stimulation. Comparison of evoked voltage responses under 6 Hz rhythmic stimulation using single (top) or 60 Hz triplet (below) stimuli. B Overlay of the first and last evoked voltage responses of the stimulation train applied at 6 and 10 Hz for theta (above) and theta-gamma (below) stimuli. C Comparison of normalized voltage response as a function of stimulation frequency for theta and theta-gamma stimuli, as shown in Figure 16 and 17.Scale bar 1 mV and 50 ms.

3.2.4 Discussion

In this work we present a characterization of neurons from layer II of ACo with the aim to investigate whether resonant neurons are part of a defined cell type, in terms of morphology, as well as passive and active electrophysiological properties. Interestingly, despite the characteristic subthreshold impedance profile that allows a clear differentiation between neurons that display resonance and neurons that do not (Vera et al., 2014), it was not possible to correlate this either intrinsic, synaptic or morphological parameters. Despite the lack of other specific similarities within each group of neurons, during the process of characterization we obtained valuable information that helps understanding ACo as an amygdaloid region that processes olfactory stimuli, with a cellular organization and functional properties different from PC.

To our knowledge, this is the first description of resonant neurons not constituting a clearly defined cell type. According to our results, near 30 % of ACo neurons display subthreshold resonance ($Q \geq 1.1$), and considering all neurons belonging to the mixed group ($1<Q<1.1$) the amount of resonant neurons reaches a possible maximum of near 70%. It is interesting that choosing any other parameter, it results difficult to clearly identify resonant from non-resonant neurons, which is very straightforward in other brain regions like hippocampus or entorhinal cortex (Canto et al., 2008; Spruston & McBain, 2007). However, we found a correlation between resonance and firing pattern, with practically all R neurons displaying stuttering firing pattern (Fig. 10 and Table 1). Since stuttering firing is related to subthreshold oscillations and firing at theta rhythm, the fact that most R neurons are stuttering-firing implies that these neurons have

subthreshold and suprathreshold building mechanisms to favor oscillatory activity at theta frequencies.

We also showed that resonant neurons have an SK current contributing to the after-hyperpolarization potential of medium duration, and despite the fact this current does not influence firing at theta frequency, their contribution confirms the calcium entry after firing action potentials. This is important, since calcium signaling is used for the coupling of excitation and genes transcription, crucial phenomenon in the regulation of activity levels and neuronal performance (Bading et al., 1993; Dolmetsch, 2003).

The other question addressed in this investigation is whether neurons from ACo layer II are able to process rhythmic inputs from OB projections. This is a very relevant topic because resonance always has been studied using somatic or dendritic stimulation through the recording electrode (Erchova et al., 2004; Hu, Vervaeke, & Storm, 2002; Hutcheon, Miura, & Puil, 1996; Pape, Paré, & Driesang, 1998; Puil, Meiri, & Yarom, 1994), ignoring the possible time-dependent changes that may occur during synaptic transmission like facilitation or depression (Creager, Dunwiddiet, & Lynch, 1980; Debanne, Guerineau, Giihwiler, & Thompson, 1996). Supposing that rhythmic synaptic inputs are arriving to a resonant neuron, if synaptic transmission is subject to facilitation it is possible that neurons depolarize fast enough with only a couple of synaptic events without engaging resonant machinery. Conversely, if synaptic transmission displays strong depression rhythmic input will never reach subsequent stages of processing. The exploratory experiments shown here indicate that ACo neurons have the synaptic machinery to receive and convey theta-frequency oscillatory synaptic signals coming from the OB, a basic requirement to study a possible differential processing by resonant

neurons. An obvious question that arises from our results is why resonant and non-resonant neurons displayed the same voltage response under rhythmic stimulation, without signs of different frequency processing. One possibility is that rather than a lack of differential processing between resonant and non-resonant neurons, the problem was that the content of theta frequencies present in our stimulation protocol was not enough to reveal differences between both groups. Under a close inspection of the voltage responses of neurons when are stimulated at theta rhythm (Fig. 16A) it is possible to see that voltage response to stimulation at frequencies between 0.5 and 6 Hz have identical temporal course, taking around tens of ms for the rise and falling components. Despite the fact that selected inter-stimulus intervals match low frequency stimulation (0.5-6 Hz), the frequency component of the synaptic event is above 60 Hz, thus explaining why resonant neurons can not express their selective filtering of slow oscillations. To evaluate the ability of resonant neurons to selectively filter low frequency synaptic-driven oscillations is necessary to generate a stimulation protocol containing low frequency components. One possibility is to use a protocol with trains of stimulations that would incorporate low frequency components through the train envelope, similar to the case of theta-gamma nested stimulation (Fig. 17A).

3.2.5 References

Ahmed OJ, Mehta MR (2009) The hippocampal rate code: anatomy, physiology and theory. Trends Neurosci 32:329–338.

Bading H, Ginty D, Greenberg ME (1993) Regulation of Gene in Expression by Hippocampal Neurons by Distinct Calcium Signaling Pathways. Science (80-) 260:181–186.

Bean BP (2007) The action potential in mammalian central neurons. Nat Rev Neurosci 8:451–465.

Bond CT, Maylie J, Adelman JP (2005) SK channels in excitability, pacemaking and synaptic integration. Curr Opin Neurobiol 15:305–311.

Burton BG, Economo MN, Lee GJ, White J a (2008) Development of theta rhythmicity in entorhinal stellate cells of the juvenile rat. J Neurophysiol 100:3144–3157.

Cang J, Isaacson JS (2003) In vivo whole-cell recording of odor-evoked synaptic transmission in the rat olfactory bulb. J Neurosci 23:4108–4116.

Canto CB, Wouterlood FG, Witter MP (2008) What does the anatomical organization of the entorhinal cortex tell us? Neural Plast 2008:381243.

Chapman C, Lacaille JC (1999) Intrinsic theta-frequency membrane potential oscillations in hippocampal CA1 interneurons of stratum lacunosum-moleculare. J Neurophysiol 81:1296–1307.

Contreras D (2004) Electrophysiological classes of neocortical neurons. Neural Netw 17:633–646.

Creager B, Dunwiddiet T, Lynch G (1980) Paired-pulse and frequency facilitation in the CA1 region of the in vitro rat hippocampus. J Physiol:409–424.

Debanne D, Guerineau NC, Giihwiler BH, Thompson SM (1996) Paired-pulse facilitation and depression at unitary synapses in rat hippocampus: quantal fluctuation affects subsequent release. J Physiol 491:163–176.

Desmaisons D, Vincent JD, Lledo PM (1999) Control of action potential timing by intrinsic subthreshold oscillations in olfactory bulb output neurons. J Neurosci 19:10727–10737.

Dielenberg R, Hunt GE, McGregor IS (2001) "When a rat smells a cat": the distribution of Fos immunoreactivity in rat brain following exposure to a predatory odor. Neuroscience 104:1085–1097.

Dolmetsch R (2003) Excitation-transcription coupling: signaling by ion channels to the nucleus. Sci STKE 2003:PE4.

Erchova I, Kreck G, Heinemann U, Herz a VM (2004) Dynamics of rat entorhinal cortex layer II and III cells: characteristics of membrane potential resonance at rest predict oscillation properties near threshold. J Physiol 560:89–110.

Fernandez FR, White J a (2008) Artificial synaptic conductances reduce subthreshold oscillations and periodic firing in stellate cells of the entorhinal cortex. J Neurosci 28:3790–3803.

Fiala J, Spacek J, Harris K (2008) Dendrite structure. In: Dendrites, 2nd ed. (Stuart GJ, Spruston N, Hausser M, eds), pp 1–42. Oxford University Press.

Franks KM, Isaacson JS (2005) Synapse-specific downregulation of NMDA receptors by early experience: a critical period for plasticity of sensory input to olfactory cortex. Neuron 47:101–114.

Haberly L (1998) Olfactory cortex. In: Synaptic organization of the brain, 4th ed. (Shepherd GM, ed), pp 377–416. Oxford University Press, USA.

Haberly LB (1983) Structure of the piriform cortex of the opossum. I. Description of neuron types with Golgi methods. J Comp Neurol 213:163–187.

Hu H, Vervaeke K, Storm JF (2002) Two forms of electrical resonance at theta frequencies, generated by M-current, h-current and persistent Na+ current in rat hippocampal pyramidal cells. J Physiol 545:783–805.

Hutcheon B, Miura RM, Puil E (1996) Subthreshold membrane resonance in neocortical neurons. J Neurophysiol 76:683–697.

Hutcheon B, Yarom Y (2000) Resonance, oscillation and the intrinsic frequency preferences of neurons. Trends Neurosci 23:216–222.

Izhikevich EM (2002) Resonance and selective communication via bursts in neurons having subthreshold oscillations. Biosystems 67:95–102.

Kajiwara R, Tominaga T, Takashima I (2007) Olfactory information converges in the amygdaloid cortex via the piriform and entorhinal cortices: observations in the guinea pig isolated whole-brain preparation. Eur J Neurosci 25:3648–3658.

Kay LM, Beshel J, Brea J, Martin C, Rojas-Líbano D, Kopell N (2009) Olfactory oscillations: the what, how and what for. Trends Neurosci 32:207–214.

Kepecs A, Uchida N, Mainen ZF (2006) The sniff as a unit of olfactory processing. Chem Senses 31:167–179.

Klink R, Alonso A (1997) Morphological characteristics of layer II projection neurons in the rat medial entorhinal cortex. Hippocampus 7:571–583.

Ledoux JE (2000) Emotion Circuits in the Brain. Annu Rev Neurosci 23:155–184.

McDonald a J (1998) Cortical pathways to the mammalian amygdala. Prog Neurobiol 55:257–332.

Pape HC, Paré D, Driesang RB (1998) Two types of intrinsic oscillations in neurons of the lateral and basolateral nuclei of the amygdala. J Neurophysiol 79:205–216.

Pastoll H, Ramsden HL, Nolan MF (2012) Intrinsic electrophysiological properties of entorhinal cortex stellate cells and their contribution to grid cell firing fields. Front Neural Circuits 6:17.

Puil E, Meiri H, Yarom Y (1994) Resonant behavior and frequency preferences of thalamic neurons. J Neurophysiol 71:575–582.

Sah P (1996) Ca(2+)-activated K+ currents in neurones: types, physiological roles and modulation. Trends Neurosci 19:150–154.

Sanhueza M, Bacigalupo J (2005) Intrinsic subthreshold oscillations of the membrane potential in pyramidal neurons of the olfactory amygdala. Eur J Neurosci 22:1618–1626.

Sevelinges Y, Gervais R, Messaoudi B, Granjon L, Mouly A-M (2004) Olfactory fear conditioning induces field potential potentiation in rat olfactory cortex and amygdala. Learn Mem 11:761–769.

Shu Y, Duque A, Yu Y, Haider B, Mccormick DA (2007) Properties of action-potential initiation in neocortical pyramidal cells: evidence from whole cell axon recordings. J Neurophysiol 97:746–760.

Smear M, Shusterman R, O'Connor R, Bozza T, Rinberg D (2011) Perception of sniff phase in mouse olfaction. Nature 479:397–400.

Sosulski DL, Bloom ML, Cutforth T, Axel R, Datta SR (2011) Distinct representations of olfactory information in different cortical centres. Nature 472:213–216.

Spruston N, McBain CJ (2007) Structural and functional properties of hippocampal neurons. In: The hippocampus book (Andersen P, Morris R, Amaral D, Bliss T, O'Keefe J, eds), pp 133–201. Oxford University Press.

Stocker M (2004) Ca(2+)-activated K+ channels: molecular determinants and function of the SK family. Nat Rev Neurosci 5:758–770.

Stocker M, Krause M, Pedarzani P (1999) An apamin-sensitive Ca2+-activated K+ current in hippocampal pyramidal neurons. Proc Natl Acad Sci U S A 96:4662–4667.

Storm JF (1987) Action potential repolarization and a fast after-hyperpolarization in rat hippocampal pyramidal cells. J Physiol:733–759.

Storm JF (1989) An after-hyperpolarization of medium duration in rat hippocampal pyramidal cells. J Physiol 409:171–190.

Suzuki N, Bekkers JM (2006) Neural coding by two classes of principal cells in the mouse piriform cortex. J Neurosci 26:11938–11947.

Suzuki N, Bekkers JM (2011) Two layers of synaptic processing by principal neurons in piriform cortex. J Neurosci 31:2156–2166.

Swanson L, Petrovich L (1998) What is the amygdala ? Trends Neurosci 21:323–331.

Vera J, Pezzoli M, Pereira U, Bacigalupo J, Sanhueza M (2014) Electrical Resonance in the θ Frequency Range in Olfactory Amygdala Neurons. PLoS One 9:e85826.

Villalobos C, Shakkottai VG, Chandy KG, Michelhaugh SK, Andrade R (2004) SKCa channels mediate the medium but not the slow calcium-activated afterhyperpolarization in cortical neurons. J Neurosci 24:3537–3542.

Wang X (2010) Neurophysiological and Computational Principles of Cortical Rhythms in Cognition. Physiol Rev 90:1195–1268.

West a E, Chen WG, Dalva MB, Dolmetsch RE, Kornhauser JM, Shaywitz a J, Takasu M a, Tao X, Greenberg ME (2001) Calcium regulation of neuronal gene expression. Proc Natl Acad Sci U S A 98:11024–11031.

Wilson D (2001) Receptive fields in the rat piriform cortex. Chem Senses 26:577–584.

Zhang L, McBain CJ (1995) Potassium conductances underlying repolarization and after-hyperpolarization in rat CA1 hippocampal interneurones. J Physiol 488 (Pt 3:661–672.

3.3 Mechanism for perithreshold resonance in pyramidal neurons from CA1 hippocampus.

The data presented in this section is unpublished, and is a draft manuscript written by Jorge Vera in preparation for submission to a peer-reviewed journal:

Vera J., Reynaert B., Alcayaga J., Bacigalupo J. and Sanhueza M. (2014) Contribution of persistent Na^+ current and muscarine-sensitive K^+ current to perithreshold behavior of CA1 pyramidal neurons.

Whether CA1 pyramidal neurons display resonance at perithreshold potential is controversial, with some researchers reporting strong resonant behavior whereas others claim that pyramidal neurons behave as non-resonant. Here we describe in detail the perithreshold behavior of CA1 pyramidal neurons and propose a mechanism that reconcile both contradictory propositions.

3.3.1 Abstract

Most neurons from hippocampus and other learning and memory-related areas have the ability to intrinsically generate rhythmic activity at theta frequency, which may contribute to the strong theta waves observed during hippocampal-related behaviors like navigation or episodic memory formation. Pyramidal neurons from CA1 area receive theta rhythmic inputs from other regions generating place fields. The way these neurons respond to perithreshold oscillatory stimulation has been controversial, with evidence favoring a non-resonant or integrator-like behavior and other studies claiming for a

resonant behavior. The currents that contribute to perithreshold behavior of pyramidal neurons are the persistent sodium current I_{NaP}, a depolarizing fast-activating current that develops above -70 mV and the muscarine-sensitive K^+ current I_M, with a hyperpolarizing effect, slower activation and that is gated by voltages more depolarized than -60 mV. By using current and voltage clamp we conducted a detailed description of perithreshold excitability of CA1 pyramidal neurons under oscillatory stimulation. We found that these neurons have two different perithreshold behaviors, a 20% of neurons expresses resonant behavior and translates theta frequency selectivity to spiking, while the other 80% acts as low-pass filters, without expressing theta frequency preference in the discharge. While I_M is present in CA1 neurons, in the latter group spike firing prevents the expression of perithreshold resonance in our slices. Paired measurement of I_{NaP} and I_M showed that at perithreshold membrane potentials the activation level of I_M is in general low, while I_{NaP} is high enough to depolarize neurons toward spike threshold overcoming the subtle hyperpolarizing effect of I_M, thus explaining the most abundant non-resonant perithreshold behavior. After a partial block of I_{NaP} with pharmacological tools or dynamic clamp, it was possible to change non-resonant behavior to resonant, demonstrating that the difference between both groups is the activation level of I_{NaP}. Furthermore, changing the activation range for I_M towards hyperpolarized potentials by using dynamic clamp also transformed non-resonant neurons onto resonant. We propose that the relative levels of I_{NaP} and I_M control perithreshold behavior of pyramidal neurons. The fact that these two currents are highly modulated by intracellular signaling and neuromodulators provides a fast mechanism to tune perithreshold frequency preference and selective firing at CA1 according to cell and network activity.

3.3.2 Introduction

In mammals, cognitive and behavioral processes dependent on hippocampal function like memory and navigation rely on network oscillatory activity in theta range (O'Keefe and Recce, 1993; Buzsaki, 2002; Csicsvari et al., 2003; Buzsáki, 2005, 2006; Lisman, 2005). Principal neurons from CA1 hippocampus are endowed with an intrinsic tendency to favor activity at theta frequency by displaying an increased voltage response under rhythmic stimulation in the theta range, thus acting as resonators (Hu et al., 2002). The increased voltage response at the preferred frequency is the result of an active attenuation of low-frequency voltage responses by specific membrane currents in addition to the passive filtering of high frequency oscillations due to the charge of the cellular membrane (Hutcheon and Yarom, 2000). This generates a band-pass filtering property that tunes the voltage response of resonant neurons at a specific frequency of inputs (Izhikevich, 2002). Resonant neurons have a bell-shaped impedance profile characterized by the resonant frequency, f_R, defined as the frequency where the impedance reaches its peak, Z_{Max}. The resonance strength is measured as the ratio between Z_{Max} and the impedance at 0.5 Hz, known as the Q value (Hutcheon and Yarom, 2000).

The mechanism described for subthreshold resonance is based on three voltage-sensitive ionic currents widely present in the mammalian brain: the hyperpolarization-activated cationic current I_h (Biel et al., 2009), the muscarine- and voltage-sensitive current, I_M (Shah et al., 2002), and the voltage-sensitive persistent sodium current, I_{NaP} (Crill, 1996). The activation voltage range for the first two currents is opposed, with I_h activating at voltages more hyperpolarized than -70 mV, and I_M above -60 mV thus covering most of

the subthreshold range. I_h and I_M are both slow-activating and non-inactivating currents that generate the attenuation of low-frequency responses by driving membrane potential away from their activation voltage range, thus generating a feedback loop that decreases oscillation amplitude (Hutcheon and Yarom, 2000). Since the activation/deactivation time constant (τ) for these currents is in the range of tens of ms, oscillatory activity with a period slower than $1/2\pi\tau$ (< ~5-10 Hz) will result in current activation or deactivation and consequent attenuation of the voltage response (Hutcheon and Yarom, 2000). In addition, these two currents have a differential subcellular distribution, with the channels responsible for I_h (HCN) expressed in dendrites in a gradient that increases in density with the distance from the soma (Notomi and Shigemoto, 2004), and the I_M-generating channels (KCNQ2/3) mostly restricted to the somatic region (Hu et al., 2007).

In turn, I_{NaP} is a fast-activating (~1 ms time constant) non-inactivating and voltage-sensitive current that activates at potentials above -70 mV (French et al., 1990). Given these properties and its depolarizing effect, this current serves as an amplifier of subthreshold voltage oscillations in both resonant and non-resonant neurons (Hutcheon and Yarom, 2000).

Considering the voltage-sensitivity and cellular distribution of the conductances involved in resonance, it has been proposed that CA1 pyramidal neurons possess a dual and complementary resonant mechanism. One component is the I_h-driven resonance, which is present in dendrites and filters voltage oscillation at hyperpolarized potentials, while the second component is I_M-driven resonance that operates at somatic location and at perithreshold potentials (Hu et al., 2009). While the former mechanism is widely accepted, the latter is controversial because perithreshold resonance is not always

observed (discussed in Hu et al, 2002) and it is often considered that only in slices pyramidal neurons behave as integrators (Prescott et al., 2008). To understand the contribution of intrinsic neuronal properties to the well-known oscillatory activity of the hippocampus (Harris et al., 2002; Goutagny et al., 2009; Lubenov and Siapas, 2009), it is necessary to address this discrepancy.

The perithreshold behavior of CA1 pyramidal neurons results from the interplay between I_{NaP} and I_M. Aside the well-documented individual contribution of each current to neuronal excitability, at both, perithreshold and suprathreshold voltage ranges, the relative influence exerted by these currents on the setting of perithreshold behavior remains unexplored. Their opposed effects on membrane potential and similar voltage range of activation, together with a high degree of modulation by second messengers and neuromodulators (Crill, 1996; Marrion, 1997), place the combination of two currents as a possible and sophisticated mechanism for control of perithreshold excitability. In this scenario, if a pyramidal neuron is subjected to rhythmic afferent stimulation, as is observed in *in vivo* recordings (Kamondi et al., 1998), the outcome will depend on their behavior just below action potential threshold. If the neuron behaves as a non-resonator (i.e. as integrator), it will be insensitive to the specific frequency of the rhythmic stimulation and will respond with preference for the slowest (near 0 Hz) oscillatory activity. However, if the neuron resonates it is expected to display an increased voltage response when stimulated at their preferred frequency, favoring spike generation at that specific frequency range and thus contributing with their own preference to the network oscillatory activity.

In order to compare the contribution of each current to perithreshold behavior of CA1 pyramidal neurons, in this paper we investigate the voltage range of action of both, I_M and I_{NaP}, using whole-cell patch-clamp technique under current- and voltage-clamp configuration.

We found that CA1 pyramidal neurons present two different types of subthreshold behaviors when stimulated with an oscillatory current of constant amplitude and linearly increasing frequency (ZAP stimulation). A 20% of them express perithreshold resonance and fire selectively at the preferred theta frequency, while the other 80% of them acts as integrators at the perithreshold region, i.e., without theta frequency preference. These non-resonant neurons preserve their behavior when depolarized until reaching spike threshold, firing spikes with higher probability at the lowest frequencies of stimulation tested. However, all non-resonant cells actually display I_M-driven resonance when depolarized in presence of the sodium channel blocker tetrodotoxin (TTX), suggesting that spike firing precludes the expression of perithreshold resonance in these cells. Paired measurement of I_{NaP} and I_M in the same cells showed that at perithreshold membrane potentials the activation level of I_M is near 0, with the current being practically absent in most neurons, while I_{NaP} is activated enough to depolarize neurons toward spike threshold, thus explaining the most abundant non-resonant behavior. After a partial block of I_{NaP} with a selective pharmacological agent or by dynamic clamping, it was possible to change the behavior of non-resonant neurons to resonant, thus demonstrating that the difference between both groups is the level of activation of I_{NaP}, compared to I_M. Furthermore, changing the activation range for I_M towards hyperpolarized potentials by using dynamic clamp, also transforms non-resonant

neurons into resonant. We propose that the relative levels of I_{NaP} and I_M control perithreshold behavior of these neurons. The fact that both currents are highly modulated by intracellular signaling and neuromodulators (Li et al., 1992; Moore and Schweitzer, 1994; Ma et al., 1997; Schweitzer, 2000; Mantegazza et al., 2005), produces a fast mechanism to tune perithreshold frequency preference and selective firing at CA1 hippocampus.

3.3.3 Results

Most CA1 pyramidal neurons do not show perithreshold resonance under somatic sinusoidal stimulation

Our first approximation for investigating the perithreshold behavior of pyramidal neurons was to measure the voltage response of these neurons to ZAP stimulation under whole cell current clamp. We stimulated neurons with a ZAP protocol in order to produce a voltage oscillation of ~5-8 mV peak-to-peak, while neurons were held at hyperpolarized (-85 mV), near resting (-70 mV) or depolarized (-63 mV) subthreshold potentials. When exploring the most depolarized potentials, just before reaching spike threshold (i.e. the perithreshold potential), two types of behaviors arise regarding the processing of oscillatory stimuli. Most neurons (21 out of 26) allow a subthreshold stimulation up to an average potential of -63.6 ± 2.8 mV displaying an impedance profile with low-pass filter properties (Q = 1, which means that the maximal impedance is observed at the lowest measured frequency (0.5 Hz)), with a complete absence of subthreshold resonance (Figure 19A-B, red traces). In contrast, when depolarized to a similar voltage (-62.3 ± 0.6 mV), the remaining neurons (5 out of 26), displayed a strong

resonant behavior with Q= 1.24 ± 0.09 and f_R, 3.5 ± 1.6 Hz ($p < 0.0005$), while showing a lower Z_{max} (119.5 ± 8.2 MΩ vs 175 ± 8.8 MΩ, for resonant and non-resonant cells, $p < 0.005$) (Figure 19A-C, black traces). Note, however, that at -85 mV these two groups of cells have on average a similar impedance profile, without significant differences in Q (1.22 ± 0.02 vs 1.17 ± 0.06, $p = 0.21$), in f_R (6.1 ± 0.3 Hz vs 6.9 ±1.2 Hz, $p = 1.5$) or Z_{max} (60.7 ± 6.8 MΩ vs 52.9 ± 11.8 MΩ, $p = 0.3$). At -70 mV the impedance profile (Q, f_R and Z_{max}) is also similar for neurons that resonate and those that do not resonate at perithreshold potential, showing that despite the difference at perithreshold potential, both groups of neurons share the same subthreshold response to oscillatory stimulus. These results are summarized in Fig. 19C.

These observations indicate that while CA1 pyramidal neurons have a robust and general resonant behavior at hyperpolarized potential, when depolarized to perithreshold levels only a 20% of them display resonance, with the remaining 80% behaving as low-pass filters.

To evaluate if pyramidal neurons display frequency-preference in the spiking regime under oscillatory stimulation (peak-to-peak oscillation of ~5-8 mV), we applied the ZAP protocol at a slightly more depolarized potential in order to reach the spike threshold and quantified the firing probability as a function of frequency (see Methods). Using this protocol, we observed that those neurons that do not show resonance at perithreshold

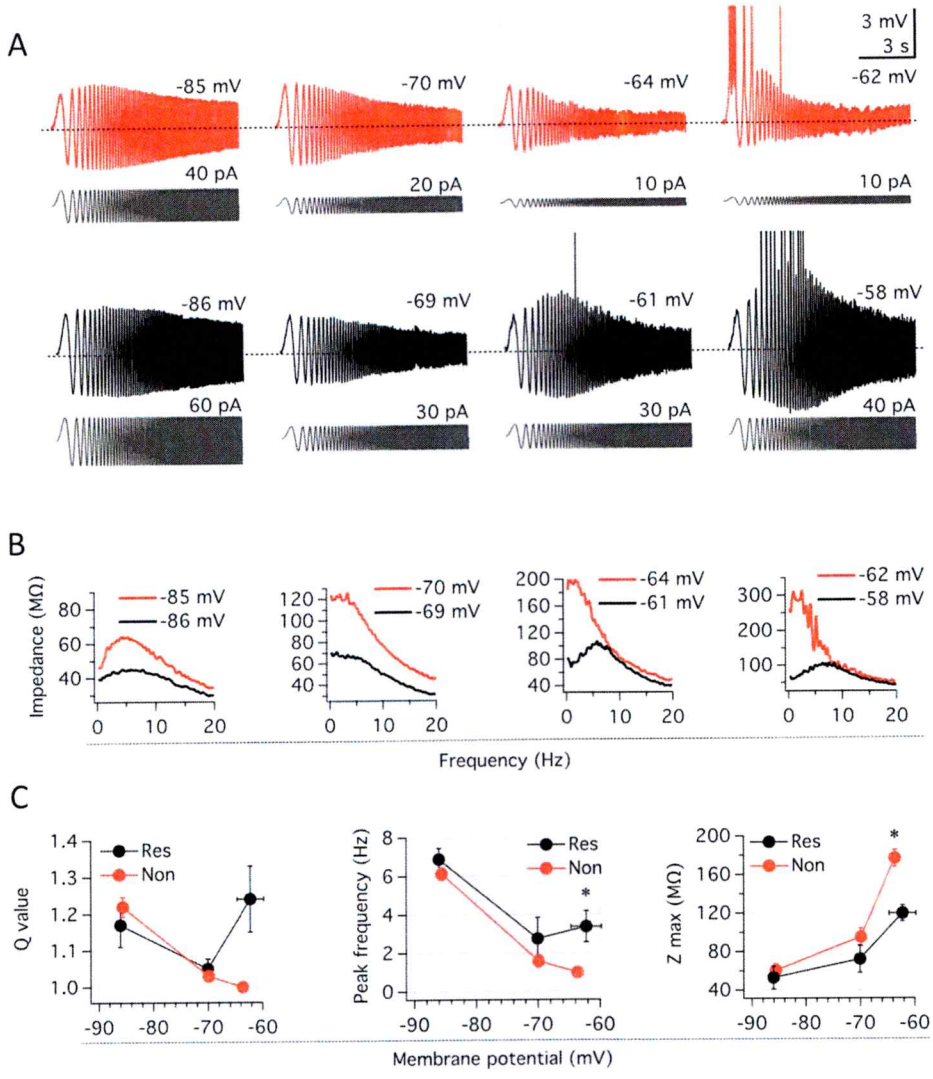

Figure 19. CA1 pyramidal neurons display two different behaviors under perithreshold oscillatory stimulation. A Subthreshold voltage response of two CA1 pyramidal neurons under ZAP stimulation at four different membrane potential, representing two different perithreshold behaviors, non-resonant (red) or resonant (black). B Impedance profile obtained from recordings in A, for non-resonant (red) and resonant (black) neurons. C Quantification of resonant parameters for neurons displaying non-resonant (n=21) and resonant (n=5) behavior at perithreshold potential.

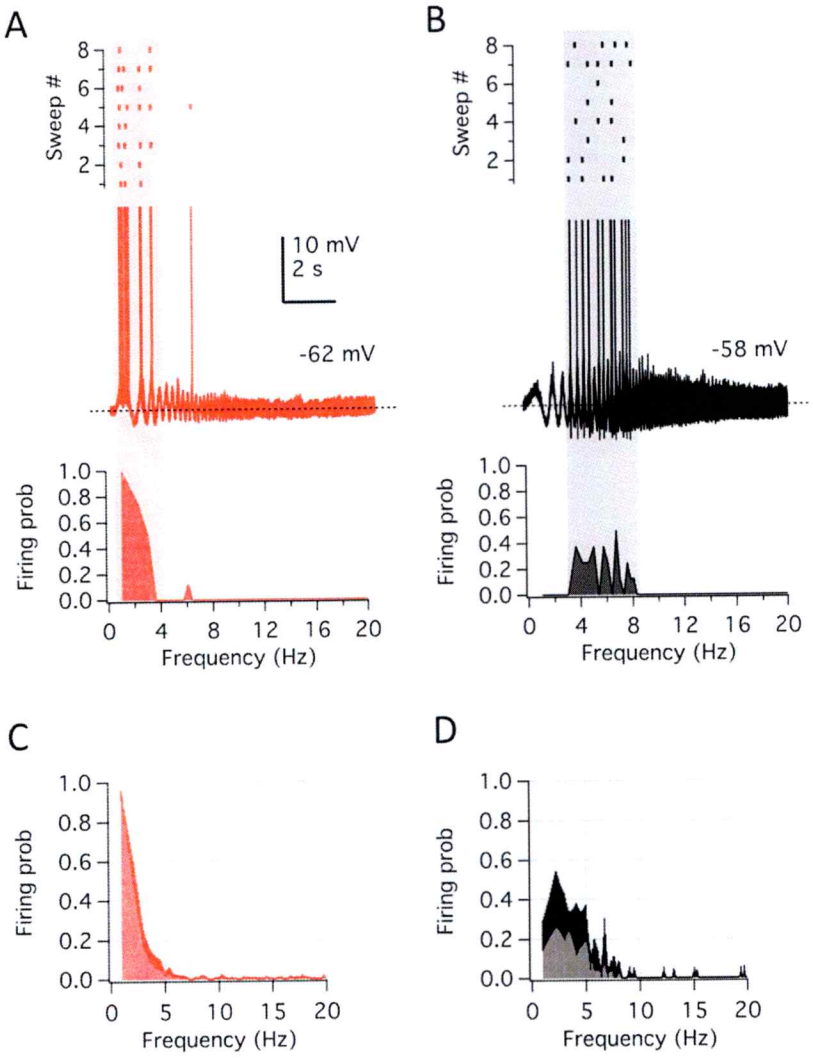

Figure 20. Different perithreshold behavior of CA1 pyramidal neurons is maintained under firing regime. A Voltage response of a non-resonant pyramidal neuron when the ZAP stimulation is applied at near-threshold membrane potential (overlay of 8 consecutive recordings is shown). The raster plot shows the firing activity for each trace (top) and the firing probability as a function of frequency of stimulation is shown at the bottom. B Same as A, but for a resonant neurons. C and D show the average firing probability curve for non-resonant (n=21) and resonant neurons (n=5).

potential start to fire action potentials during the first depolarizing incursion at low frequency (1.2 Hz, Figure 20A, red trace at right). On the other hand, when neurons that displayed subthreshold resonance near -60 mV were depolarized to reach spike threshold, they translated their perithreshold frequency preference to spiking regime, firing action potentials with a higher probability near 3-4 Hz with a clear attenuation of voltage responses and firing probability at lower frequencies (Figure 20 B, D). The low-pass filter behavior at perithreshold potential present in most pyramidal neurons is highly uniform between all neurons that belong to this group as opposed to the other group of neurons that display perithreshold resonance, which present more variability at their individual firing preference. This variability can be seen in the average curve of firing probability vs frequency of each group (Fig. 20C-D), and may reflect that perithreshold behavior of pyramidal neurons varies as a continuum from non-resonant to highly resonant, as the example shown in Figure 20B.

Spike firing prevents expression of M-resonance

The described difference in perithreshold behavior of pyramidal neurons suggests that the conductances that control perithreshold resonance, I_{NaP} and I_M, may have different levels of activation in these two cell populations. For example, one possibility is that in non-resonant neurons the amount of I_M may be too low to engage neurons in resonant behavior.

To evaluate this possibility we explored the ZAP-induced voltage response at suprathreshold potentials in presence of the selective sodium channel blocker tetrodotoxin (TTX) to avoid spike generation while exploring membrane potentials up to

-45 mV with 5 mV steps. In these conditions it is possible to see that all studied neurons, despite of being non-resonant near -60 mV, they display strong resonant behavior at membrane voltages above -55 mV (Q=1.34 ± 0.09 and 1.65 ± 0.14 and f_R= 4.2 ± 0.7 Hz and 5.5 ± 0.5 Hz for -50 mV and -45 mV, respectively, n=9. Fig. 21A-E). To corroborate that the observed resonant behavior was consequence of I_M activation we bath-applied the selective M-channel blocker XE991, observing that resonance at depolarized potentials was eliminated (Q=1.03 ± 0.03 and 1.07 ± 0.04 and f_R= 1.5 ± 0.4 Hz and 1.8 ± 0.3 Hz for -50 mV and -45 mV, respectively. $p < 0.01$, paired t-test, n=6. Fig. 21A-E). These experiments show that M-resonance appears in all neurons consistently at voltages above -55 mV, which is above the transition from resting to spiking regime. This suggests that in non-resonant neurons the impact of M-resonance on somatic filtering is hidden by action potential firing.

In order to compare the spike threshold value with the voltage range at which I_M is expressed, we measured the action potential threshold of spikes fired under oscillatory stimulation (here the threshold is defined as the voltage at which dVm/dt > 0.5 mV/ms and values were obtained from experiments shown in Figure 20). We obtained a value of -52.0 ± 0.9 mV and -50.9 ±1.3 mV for non-resonant (n=18) and resonant (n=6) neurons, respectively, without statistical differences among groups ($p = 0.27$, t-test). This lack of difference in spike threshold indicates that the latter is not causing the dissimilar firing patterns observed, and suggests that the difference in spiking behavior between these two groups results from a distinct perithreshold dynamics at membrane voltages below spike threshold, at perithreshold potentials. Is at that voltage range where the divergence

groups have different level of depolarization at perithreshold potential we measured the average membrane potential during the whole stimulation protocol shown in Figure 20, without taking into account spikes. We obtained a value of -61.7 ± 0.8 mV for non-resonant neurons and slightly more depolarized perithreshold potential of -59.0 ± 1.4 mV for resonant neurons ($p < 0.05$). Since the perithreshold potential results from the interplay of I_{NaP} and I_M, this difference in the depolarization level of each cell group suggests that the differential behavior resides on variations on the relative amount of perithreshold currents. Therefore, we decided to investigate the relative magnitudes and voltage activation ranges of these cells.

Measurement of somatic I_{NaP}

A ramp protocol was used to measure the voltage sensitivity of I_{NaP}, taking advantage on the TTX sensitivity of this current and on its different inactivation time constant compared with the fast transient sodium current (Magistretti and Alonso, 1999). Whole cell currents where elicited by a slow voltage ramp (30 mV/s) in order to inactivate fast current, both in control condition and after the application of 1 μM TTX (Fig. 22A). I_{NaP} was obtained digitally by subtracting the recording in TTX from the control condition (Fig. 22B). After this procedure we obtained a TTX-sensitive current that showed non-linear voltage dependence, activating at command potentials above -70 mV and reached peak amplitude near -40 mV (Fig. 22B). Since we modified the driving force for Na^+, we recorded a reduced I_{NaP} with respect to current clamp condition. We obtained a

variable independent of the modified sodium reversal potential by calculating the sodium persistent conductance (G_{NaP}) dividing the measured current by its driving force (V_m-E_{Na}). The voltage-dependent activation of G_{NaP} was characterized by fitting a sigmoidal curve to each trace (see Methods), obtaining a voltage for half activation of -52.2 ± 1.0 mV, a slope voltage of 4.9 ± 0.4 mV and a maximal plateau conductance of 5.3 ± 0.5 nS for voltages above -40 mV (avg ± sem, n=13; Fig. 22C). These values are in agreement with previous investigations on CA1 neurons performed in dissociated cells (4.4 nS, -50.0 mV and 9 mV for G_{max}, $V_{0.5}$ and slope, respectively, French et al., 1990) and acute slices (Vervaeke et al., 2006). This result shows that at perithreshold potential (near -58 mV) a substantial amount of G_{NaP} is active, thus driving cell toward spike threshold.

Measurement of somatic I_M

Since I_M is closed at hyperpolarized potentials and activates with depolarizations, we evoked whole-cell currents by 2 s depolarizing steps to voltages between -77.5 and -32.5 mV from a holding potential of -87.5 mV to characterize the voltage dependence of their activation around perithreshold potentials. To measure I_M in the same cells in which we previously measured I_{NaP}, we applied this voltage protocol in the presence of TTX as control condition. The described voltage protocol elicited a sustained whole-cell outward current that contained a mix of several ionic currents (Figure 22D). To isolate I_M we bath-applied 10 μM of the selective blocker XE991 and repeated the protocol after 5-8 mins (Fig. 22E), obtaining the XE991-sensitive current by digital subtraction (Fig. 22F).

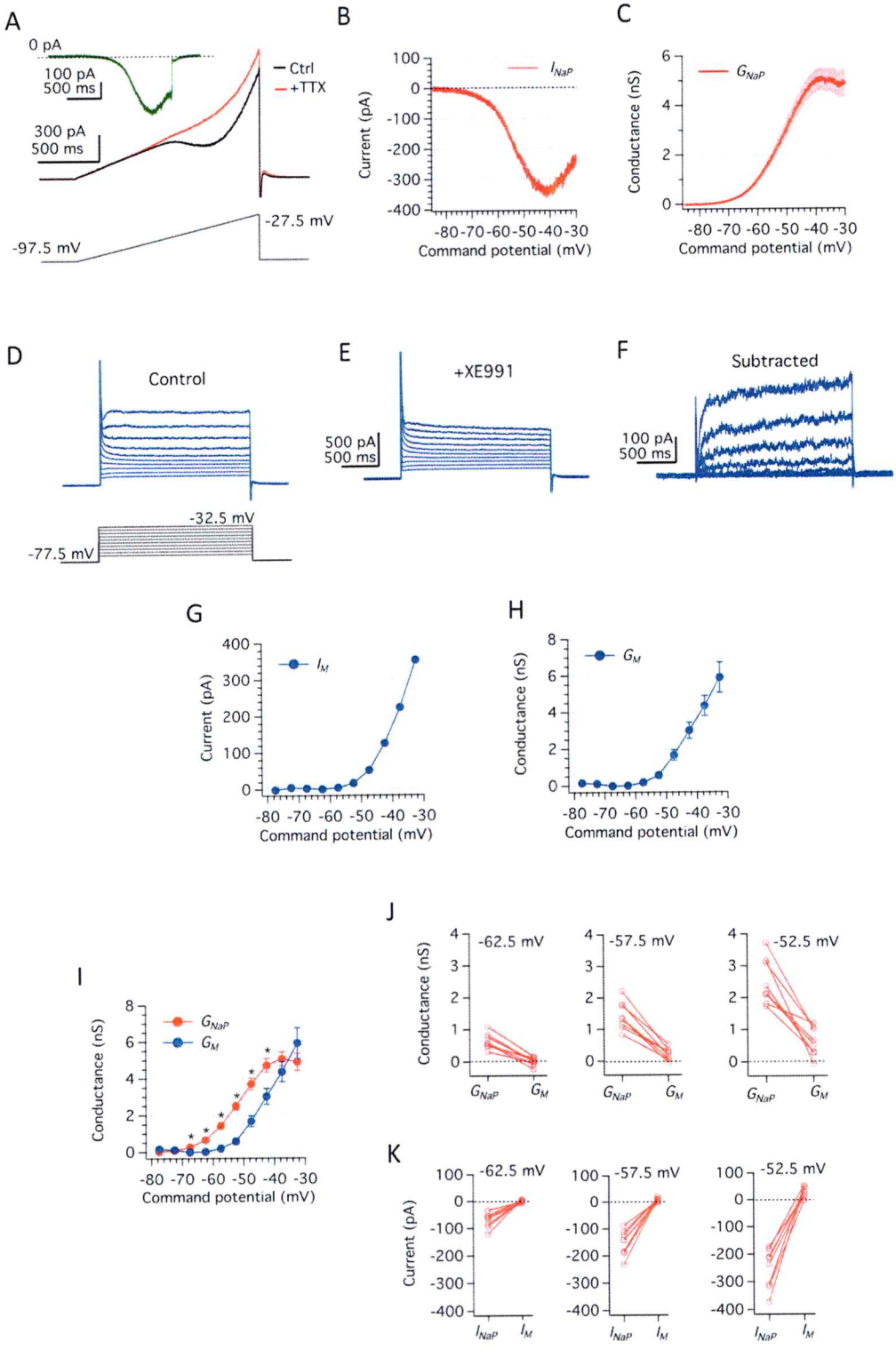
A
0 pA
100 pA
500 ms
300 pA
500 ms
Ctrl
+TTX
-27.5 mV
-97.5 mV
B
Current (pA)
I_{NaP}
Command potential (mV)
C
Conductance (nS)
G_{NaP}
Command potential (mV)
D
Control
-32.5 mV
-77.5 mV
E
+XE991
500 pA
500 ms
F
Subtracted
100 pA
500 ms
G
Current (pA)
I_M
Command potential (mV)
H
Conductance (nS)
G_M
Command potential (mV)
I
Conductance (nS)
G_{NaP}
G_M
Command potential (mV)
J
Conductance (nS)
-62.5 mV
-57.5 mV
-52.5 mV
G_{NaP}
G_M
K
Current (pA)
-62.5 mV
-57.5 mV
-52.5 mV
I_{NaP}
I_M

Figure 22. Voltage-clamp measurement of I_{NaP} and I_M. A Protocol used to measure I_{NaP}. We used a slow depolarizing voltage ramp to inactivate transient sodium current in control condition (black) and after the addition of 1 μM TTX (red). Clean I_{NaP} is obtained from the subtraction of these two recordings (green trace). B Single I_{NaP} vs command potential curve. C Average G_{NaP} vs command potential curve. Individual conductances curves were obtained dividing I_{NaP} by V_m-E_{Na}. D-E Protocol used to measure I_M. Neurons were held at -87.5 mV and a family of depolarizing 2 s squared voltage pulses were used to explore command potentials between -77.5 and -32.5 with 5 mV steps at control conditions (D) and after bath addition of 10 μM of XE991. E I_M is isolated by subtracting recordings in XE991 from those in control condition. G I_M vs command potential from traces showed in F (current was measured as the average of the last 50 ms of the pulse). Average G_M vs command potential curve. Individual conductances curves were obtained dividing I_M by V_m-E_K. I Overlay of G_{NaP} and G_M curves shown in C and H, respectively. Continue G_{NaP} curve was quantized extracting values at same potentials explored for G_M. J Paired comparison of G_{NaP} and G_M obtained at three perithreshold potentials (n=8). K Paired comparison of I_{NaP} and I_M calculated using reversal potential from current clamp condition (n=8).

The isolated currents showed a slow activation constant (60-200 ms) with no inactivation, in agreement with the described I_M kinetics (Shah et al., 2002) (Fig. 22F). On the other hand, the I-V curve shows that this current is closed at resting potential and begins to activate with potentials above -55 mV, increasing monotonically with voltage and reaching near 400 pA at -32.5 mV, the maximal voltage tested (Fig. 22G). We obtained the G-V curve dividing the I-V trace by the driving force for K^+, obtaining the voltage dependence of its conductance, G_M, that reaches near 6 nS at -32.5 mV (Fig. 22H).

Comparing perithreshold behavior of I_{NaP} and I_M

Once we had measured the voltage dependence of I_{NaP} and I_M under the same conditions and at the same cells, we were able to estimate and compare their relative activation levels at voltages explored when neurons are oscillating near perithreshold potential. To make the comparison between both conductance curves easier, we constructed a quantized curve for G_{NaP} using the values from the continuous curve at the same voltages at which I_M was measured, thus allowing a direct evaluation at each voltage step. When comparing the levels of activation of both currents resulted that at all voltages between -67.5 and -42.5 mV the amount of G_{NaP} is higher that G_M (Figure 22I). A closer inspection at perithreshold potentials shows that in all recorded neurons the amount of G_{NaP} always exceeds G_M, with G_{NaP} ranging from 0.6 to 2.5 nS whereas G_M only reaches a modest average activation of 0.6 nS at -52.5 mV (G_{NaP} vs G_M: 0.64 ± 0.08 nS vs 0.00 ± 0.04 nS at -62.5 mV, 1.44 ± 0.15 nS vs 0.21 ± 0.06 nS at -57.5 mV and 2.52 ± 0.24 nS vs 0.62 ± 0.15 nS at -52.5 mV; $p < 0.0076$, $n = 8$, Fig. 22J).

Since at perithreshold potentials the driving force for Na^+ is higher than for K^+, is expected that the difference between I_{NaP} and I_M will be even higher than for the conductances. Using the driving force given by ionic concentrations in our current clamp experiments (see Methods) we obtained that I_{NaP} is around -150 pA at spike threshold levels, while I_M only 9 pA, maintaining this paired relative difference for each recorded neuron (I_{NaP} vs I_M: -70.5 ± 8.9 pA vs 0.1 ± 1.5 pA at -62.5 mV, -150.7 ± 15.8 pA vs 8.8 ± 2.6 pA at -57.5 mV and -250.6 ± 24.0 pA vs 29.1 ± 7.0 pA at -52.5 mV; $p < 0.00011$ paired t-test, n = 8. Fig. 22K).

Summarizing these voltage-clamp results, in all recorded neurons I_{NaP} contributes to subthreshold excitability from voltages above -70 mV reaching more than -100 pA just below threshold potential, with a clear contribution to perithreshold depolarization. In contrast, I_M has a scarce contribution below spike threshold relegating its mayor impact on excitability to suprathreshold potentials (i.e. firing frequency accommodation).

Changing perithreshold behavior with I_{NaP} blockers

Since all recorded pyramidal neurons have the intrinsic machinery to display resonant behavior we explored the effect of blocking a fraction of I_{NaP}, with the purpose of reducing the driving for depolarization and with this increasing the firing threshold, thus allowing the activation of I_M at perithreshold region before spiking. Therefore, we characterized perithreshold behavior and firing preference within the oscillatory stimulation regime in control condition, after the addition of 60 μM of the I_{NaP} blocker, phenytoin (see Methods), and after washing out the blocker. Figure 23A shows a representative example of what we found in this experiment. In control condition

neurons behave as non-resonant, with a high voltage response and firing probability at the slowest oscillations. Interestingly, and in agreement to our prediction, when the I_{NaP} blocker is added to extracellular solution, the previous non-resonant neuron changed its behavior, reached a more depolarized perithreshold range, attenuated voltage response at low frequencies and displayed maximal firing probability at theta frequency, thus behaving as a resonant neuron. Notably, when the I_{NaP} blocker is washed out the neuron returned to its original non-resonant perithreshold behavior, recovering all their characteristics (Fig. 23A-B). This experiment was performed on 6 pyramidal neurons, obtaining always the same result. Figure 23C shows the average firing probability curves for all three conditions, going from a clear low-pass filter property at control condition to a band-pass filter pattern when a fraction of I_{NaP} is blocked, effect that is almost completely reversed upon blocker removal. To measure the impact of this partial blockade of I_{NaP} on impedance we built the impedance profile using those recordings where neurons were firing action potentials under the oscillatory current injection. The average impedance profile obtained in control conditions has a low-pass filter shape with a peak impedance of 270 MΩ near 0 Hz with an impedance hump near 4 Hz that breaks the monotonic drop of impedance as frequency increases (Fig. 23D). That hump might be caused by a small activation of I_M while neurons oscillate around perithreshold potentials. In presence of phenytoin the impedance near 0 Hz falls to 150 MΩ and the shape of the impedance profile changed to a band-pass filter type with the peak impedance at the same frequency of the hump observed in control conditions (see overlapped curves in Fig. 23D). This change in impedance profile is partially reversed after washing the drug out, and a decrease in the filtering of low-frequency oscillations

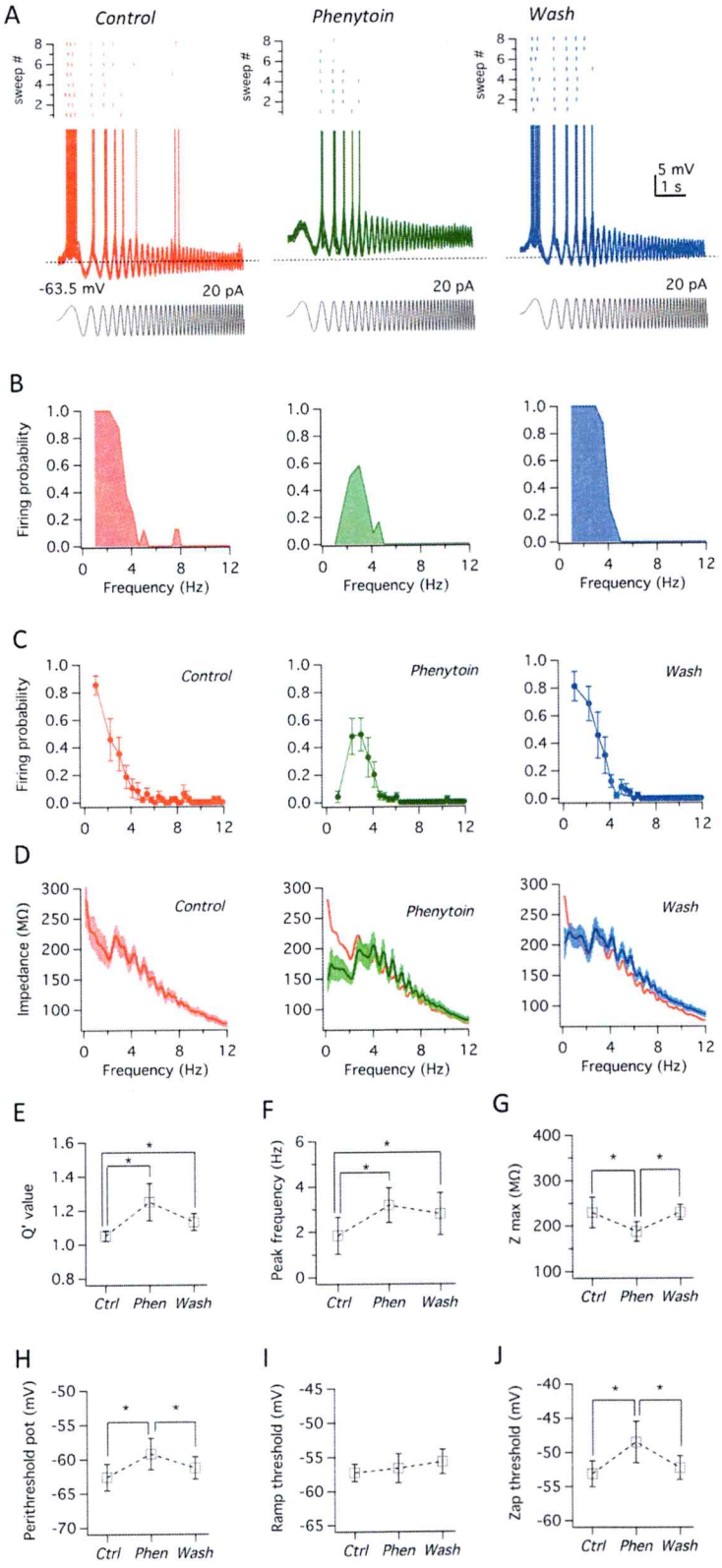
A
Control
Phenytoin
Wash
sweep #
5 mV
1 s
-63.5 mV
20 pA
B
Firing probability
Frequency (Hz)
C
Control
Phenytoin
Wash
D
Impedance (MΩ)
E
Q' value
F
Peak frequency (Hz)
G
Z max (MΩ)
H
Perithreshold pot (mV)
I
Ramp threshold (mV)
J
Zap threshold (mV)
Ctrl
Phen
Wash

Figure 23. Pharmacologic reduction of I_{NaP} produces a switch from non-resonant to resonant behavior in CA1 pyramidal neurons.
A Representative voltage response of a non-resonant CA1 pyramidal neurons under ZAP stimulation (grey) at perithreshold potential at consecutive control (red), 60 μM phenytoin (green) and wash-out (blue) conditions. Each voltage response is composed by the overlay of 8 consecutive recordings. The raster plot of the spiking activity at each condition is shown at the top of each family traces. B Firing probability vs stimulation frequency curves for recordings shown in A. C Average firing probability curves from recordings obtained in 6 neurons under the same experiment shown in A (avg ± sem). D Average impedance profile for non-resonant neurons stimulated with the ZAP protocol at near-threshold in control condition as in A (left), in phenytoin (middle, green trace) and after wash out of the drug (right, blue trace). The red trace is the average curve in control condition. E-J Average parameter measured in neurons stimulated with the ZAP protocol at perithreshold potential in the three consecutive studied conditions, average membrane potential under ZAP stimulation (E), spike threshold measured with a depolarizing current ramp (F) and spike threshold of spikes fired during ZAP stimulation (G). From impedance profile analysis, Q' value (H), peak frequency (I) and peak impedance (J). n=6, * means $p<0.05$ using paired T Test.

is manifested by the recovery of the impedance value near 0 Hz to more than 200 MΩ. Given that the analyzed voltage traces contain action potentials, and hence contain sub and suprathreshold frequency and amplitude components, we calculated an apparent Q value (Q') considering frequencies between 2 and 10 Hz in order to focus the comparison on I_M resonance. Average impedance profile revealed a Q' of 1.05 ± 0.02 at 1.8 ± 0.6 Hz that after partial block of I_{NaP} increased to 1.25 ± 0.08 at 3.2 ± 0.6 Hz, values that are in agreement with a resonant behavior generated by I_M (Fig. 23E, F). This effect is almost completely reverted after drug washout. In agreement with an amplifying effect of I_{NaP}, phenytoin addition produced a 20% drop of peak impedance (Fig. 23G).

As we predicted, the partial block of I_{NaP} also reproduced the depolarized perithreshold potential observed in resonant neurons, shifting the average voltage during the oscillatory stimulation from -63.6 ± 1.5 mV to -60.2 ± 1.7 mV ($p<0.05$), effect that is reverted after phenytoin removal (Fig. 23H).

The spike threshold measured with a voltage ramp yielded no differences when a fraction of I_{NaP} is removed, however, the spike threshold measured when spikes are fired from oscillations at perithreshold potential suffered a shift from -54.1 ± 1.4 mV to -49.5 ± 2.3 mV, reproducing another feature of resonant neurons (Fig. 23I, J).

This experiment confirms that hippocampal neurons that behave as non-resonant at perithreshold potential are able to change their perithreshold frequency preference to resonant behavior by a moderate reduction on I_{NaP}.

Modulation of perithreshold behavior through a sliding balance between I_{NaP} and I_M

The previous experiments showed that by decreasing the amount of I_{NaP} it is possible to change non-resonant behavior to resonant, at perithreshold voltages. Our following strategy to confirm this observation was to change the perithreshold balance of I_{NaP} and I_M in non-resonant neurons using the dynamic clamp technique, which allows generating virtual knock-in or knock-out of ionic currents (see Methods). In this case, we produced a virtual knock-down of I_{NaP} by injecting a negative I_{NaP} ($-I_{NaP}$) in order to decrease a fraction of total endogenous I_{NaP}. To simulate the voltage sensitivity of - I_{NaP} we used our own measured parameters obtained in voltage-clamp experiments and an activation time constant of 1 ms reported for this current on CA1 pyramidal neurons (Vervaeke et al., 2006). Thus, this experiment is analogous to the previous experiment where I_{NaP} was partially blocked with phenytoin.

On the other hand, to investigate whether non-resonant neurons are able to resonate with their natural intrinsic levels of I_{NaP} (without altering endogenous I_{NaP}) we used dynamic clamp to incorporate a virtual I_M ($+I_M$) based on the activation curve previously described with voltage-clamp experiments, but with the voltage sensitivity shifted towards hyperpolarized potentials (see Methods).

As in previous experiments, the protocol to assess frequency preference was the injection of oscillatory current at perithreshold potentials in order to induce spiking. In first place we characterized the frequency preference of a neuron in control condition, corroborating the lack of theta-frequency preference on their voltage response and firing probability (Fig. 24A, left). After verifying their non-resonant behavior we proceeded to

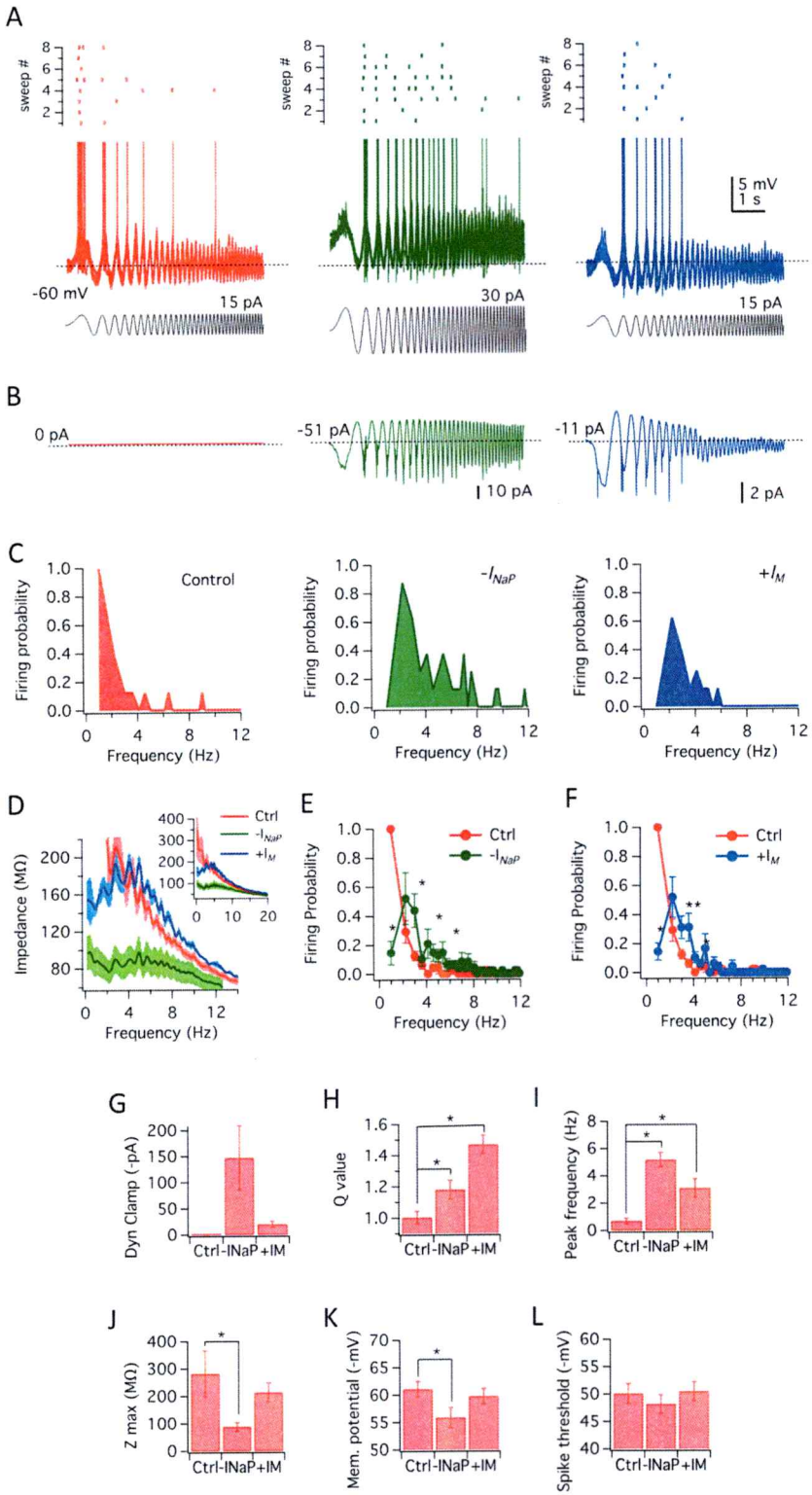
A
sweep #
5 mV
1 s
-60 mV
15 pA
30 pA
15 pA
B
0 pA
-51 pA
10 pA
-11 pA
2 pA
C
Control
$-I_{NaP}$
$+I_M$
Firing probability
Frequency (Hz)
D
Impedance (MΩ)
Ctrl
$-I_{NaP}$
$+I_M$
E
F
Firing Probability
G
Dyn Clamp (-pA)
H
Q value
I
Peak frequency (Hz)
J
Z max (MΩ)
K
Mem. potential (-mV)
L
Spike threshold (-mV)
Ctrl-INaP+IM

Figure 24. Dynamic-clamp reduction of I_{NaP} or increase of I_M produces a switch from non-resonant to resonant behavior in CA1 pyramidal neurons.
A Representative voltage response of a non-resonant CA1 pyramidal neurons under ZAP stimulation (grey) at perithreshold potential at control condition (red) and after the consecutive reduction of I_{NaP} (green) or increase of I_M (blue) by means of dynamic clamping. Each voltage response is composed by the overlay of 8 consecutive recordings. The raster plot of the spiking activity at each condition is shown at the top of each family traces. B Average trace from dynamic current injected at each condition. At control condition the dynamic current is zero, at $-I_{NaP}$ condition dynamic current is equivalent to the amount of reduced endogenous I_{NaP} and in the case of $+I_M$ condition dynamic current is the added I_M. C Firing probability vs stimulation frequency curves for recordings shown in A. D Overlay of average impedance profile for non-resonant neurons stimulated with the ZAP protocol at perithreshold potentials in control (red), in $-I_{NaP}$ (green trace) and after $+I_M$ (blue trace) conditions. The inset shows a zoom out of the overlay. E Average firing probability curves from recordings at control (red) and $-I_{NaP}$ (green) conditions. F Average firing probability curves from recordings at control (red) and $-I_M$ (blue) conditions (n=6). G-L Average quantification for this experimental set performed in six neurons: dynamic current injected at each condition (G), resonance strength at perithreshold potential (H, for details see main text), peak frequency in the impedance profile (I), peak impedance of the impedance profile, average membrane potential during ZAP stimulation at perithreshold potential (K) and the spike threshold of the spike fired under ZAP stimulation. n=6, * means $p<0.05$ using paired T Test.

inject – I_{NaP}, beginning with 2 nS of maximal conductance (G_{NaPMax}). In three out of six recorded neurons that amount of $-I_{NaP}$ was enough to observe the expression of perithreshold resonance as a filtered voltage response at low frequencies with the concomitant low firing probability at the slower tested oscillation (Fig. 24A-C). In the other three neurons, it was needed to increase the amount of - I_{NaP} to 4.5 nS in one of them and 9 nS in the other two cells. Despite the differences in the amount of injected – I_{NaP} (average of -147.6 ± 61.9 pA, Fig. 24G), in all 6 neurons it was possible to induce an equivalent perithreshold resonant behavior in terms of the impedance profile (Fig. 24D) and translation of frequency preference to firing regime (at 1 Hz the firing probability dropped from 1.0 to 0.15 ± 0.09, and at 3 Hz raised from 0.13 ± 0.04 to 0.44 ± 0.13, $p < 0.01$, Fig. 24E). Since impedance profiles contain low frequency components derived from firing activity, we calculated impedance parameters as described in the previous section (taking into account only the 2-10 Hz interval). After this procedure we obtained that the reduction of I_{NaP} increased Q' from 1.0 to 1.18 ± 0.06 ($p < 0.01$, Fig. 24H) and shifted peak frequency from 0.7 ± 0.2 Hz to 5.2 ± 0.5 Hz ($p < 0.0001$, Fig. 24I). As expected, the neutralization of native I_{NaP} eliminates its amplifier role on impedance producing a considerable reduction on impedance profile which is reflected in a drop of peak impedance from 282 ± 84.1 MΩ to 88.8 ± 15.5 MΩ ($p < 0.04$, Fig. 24D and J).

The injection of $-I_{NaP}$ shifted perithreshold potentials towards depolarization from -61.1 ± 1.4 mV to -55.9 mV ($p < 0.02$) in the same way we found with phenytoin experiments. Importantly, the modification of I_{NaP} that allows a change in perithreshold behavior without modifying the transient sodium current (I_{NaT}) does not alter the action potential

threshold of spikes fired under oscillatory stimulation (-50.1 ± 1.8 mV and -48.2 ± 1.7 mV for control and $-I_{NaP}$ condition, respectively, p = 0.16, Fig. 24L).

Right after the injection of $-I_{NaP}$ we proceeded to explore the effect of injecting $+I_M$. It was needed to shift the $V_{0.5}$ of the activation curve from -39 mV to -49 mV (n=3), -54 mV (n=1) or -59 mV (n=2), in order to achieve a critical amount of virtual I_M enough to change the perithreshold behavior from non-resonant to resonant (average activated current during voltage oscillations was -20.1 ± 7.3 pA, Fig. 23G). As expected, intrinsic I_{NaP} interacts with $+I_M$ to induce resonant behavior which is able to translate frequency preference to spiking regime, modifying firing probability with an almost complete reduction at 1 Hz oscillations from 1.0 to 0.15 ± 0.07 ($p < 1E-5$) and with an increase in the range of 3-4 Hz oscillations ($p < 0.04$, Fig. 24F). Analysis of the impedance profile shows that the injection of $+I_M$ only modifies its shape by attenuating the response to frequencies below 4 Hz without altering higher frequencies, thus changing only the low-pass filter profile to a selective band-pass filter shape and without differences on average peak impedance (282.2 ± 84.1 MΩ vs 214. 2 ± 34.2 MΩ, for control and $+I_M$ condition, respectively, p = 0.11, Fig. 24D and J). The combination of high levels of endogenous I_{NaP} together with the critic amount of $+ I_M$ produces a strong resonance expressed as an increment in Q' from 1 to 1.47 ± 0.19 ($p < 0.02$, Fig. 24H) and a shift of peak frequency of resonance from 0.7 ± 0.2 Hz to 3.7 ± 0.4 Hz ($p < 2E-4$, Fig. 24I). As expected from the unaltered I_{NaP}, under the $+I_M$ condition resonant behavior develops without depolarizing the perithreshold membrane potential, nor the spike threshold (Fig. 24K and L).

Taken together, these results show that the perithreshold behavior of CA1 pyramidal neurons can be transformed from non-resonant to resonant by changing the levels of I_{NaP} and I_M.

3.3.4 Discussion

The contribution to single cell excitability of both membrane currents investigated in this paper, I_{NaP} and I_M, has been widely described in the nervous system, but always separately. I_{NaP} contributes to repetitive firing and to generate rhythmicity, it also plays a general role as amplifier current increasing voltage responses of synaptic stimulation (EPSP and IPSP) and promoting resonance (Schwindt and Crill, 1995; Stuart and Sakmann, 1995; Pape and Driesang, 1998; Parri and Crunelli, 1998; Stuart, 1999; Brumberg et al., 2000; Hu et al., 2002). For its part, I_M is the main current involved in frequency accommodation, in control of cell excitability and it also has been described as a current generating subthreshold resonance (Marrion, 1997; Hu et al., 2002, 2007; Peters et al., 2005; Lawrence et al., 2006; Shah et al., 2008; Leão et al., 2009). These two currents have opposed effects on membrane potential, with I_{NaP} producing depolarization towards spike threshold and promoting the behavior as integrator, and with I_M hyperpolarizing the neuron and promoting resonant behavior. The precise perithreshold behavior of pyramidal neurons will depend on the relative levels of each current. It is remarkable that both currents are highly regulated, with I_{NaP} being modulated in amplitude and voltage sensitivity by PKA (Li et al., 1992) and GTP pathway (Ma et al., 1994), respectively and I_M being suppressed by activation of muscarine receptor (Delmas and Brown, 2005a) and endocanabinoids (Schweitzer, 2000) or increased by somatostatine (Moore et al., 2014). This degree of modulation may be the reason, at least in part, of why some authors have described pyramidal neurons as integrators and others as resonators. Prescott and coworkers (Prescott et al., 2008) showed that pyramidal neurons behave like integrators under *in vitro* conditions

(characterized by low synaptic input) and that under *in vivo*-like conditions (under recreated high synaptic stimulation) they switch to resonant behavior given a depolarization of spike threshold and a subsequent increase on I_M activation. This switch is a mixed mechanism between intrinsic and synaptic properties and do not explain the observation of resonant behavior under *in vitro* conditions (Hu et al., 2002). In this paper we found that pyramidal neurons from CA1 hippocampus in the same conditions, and even in the same slice, can behave as non-resonant (integrator) or resonant only relying on intrinsic properties.

Perithreshold behavior of pyramidal neurons depends on the balance between I_{NaP} and I_M

Based on the results shown in this paper, we propose that the expression of perithreshold resonance in hippocampal neurons depends on the relative magnitude of I_{NaP} and I_M at perithreshold voltages. We show that at perithreshold potentials I_{NaP} displays some degree of variability in activation among the recorded neurons, whereas I_M is mostly closed (Figure 21J-K). For this reason, we think that it is I_{NaP} (by its level of activation and maximal conductance), who governs perithreshold dynamics. In this line, perithreshold behavior of pyramidal neurons lies between two extremes. At one extreme are those neurons in which the amount of I_{NaP} is high enough to drive the membrane potential directly towards spike generation, acting as non-resonant neurons, whereas in the other extreme are those neurons in which low levels of I_{NaP} shifts perithreshold region towards depolarized potentials with the consequent activation of I_M above some critical amount that allows the expression of strong perithreshold resonance. In non-

resonant neurons the high amount of I_{NaP} relative to I_M generates a strong attractor towards action potential threshold, thus setting the perithreshold region more hyperpolarized, making even more difficult I_M activation. According to this, all CA1 pyramidal neurons have the intrinsic ability to display perithreshold frequency preference, however, the expression of this property would depend on whether the level of I_{NaP} allows significant I_M activation before spiking is triggered. Despite the fact that technical limitations precluded the recording of I_{NaP} and I_M on identified resonant neurons in order to corroborate their relative amounts of each current (see Methods), our experiments with pharmacology or dynamic clamping demonstrate that reducing the amount of I_{NaP} is enough to change a neuron from non-resonant to resonant. The same occurs when I_M is increased. Given the level of change needed to transform the perithreshold behavior, it is very plausible that in the intact brain neurons jump from one behavior to the other according to modulation by intracellular second messengers or neuromodulators. The amplitude of I_{NaP} can be reduced by 40-80% through the cAMP-dependent pathway (Li et al., 1992) and its voltage activation curve can be shifted 8-10 mV towards hyperpolarized potentials through G protein-coupled receptor pathway (Ma et al., 1997; Mantegazza et al., 2005). For its part, I_M amplitude has been shown to be increased by the neuropeptide somatostatine (Moore et al., 2014) or suppressed by endocanabinoids (Schweitzer, 2000) and multiple muscarinic agonist (Marrion, 1997; Delmas and Brown, 2005b).

The fact that we found a differential perithreshold behavior in the same experimental conditions, despite the control of intracellular metabolites concentration, suggests that the cause of the differential behavior relies in the particular quantities of Na_V and KCNQ

channels expressed at each neuron. This is in agreement with the current view of control of cell excitability, in which the level of expression of each conductance in a given neuron is variable and its relative amount compared to the other conductances present in the membrane would determine the specific neuronal behavior (Destexhe and Marder, 2004; Marder and Goaillard, 2006). Since the behavior of neurons at perithreshold potentials has a tremendous influence in the way neurons achieve the task of translating subthreshold activity to action potentials, we speculate that the ability to switch between non-resonant to resonant behavior is used to dynamically tune neuronal responsiveness according to network requirements in the intact brain.

3.3.5 References

Biel M, Wahl-schott C, Michalakis S, Zong X (2009) Hyperpolarization-Activated Cation Channels : From Genes to Function. 847–885.

Brumberg JC, Nowak LG, McCormick D (2000) Ionic mechanisms underlying repetitive high-frequency burst firing in supragranular cortical neurons. J Neurosci 20:4829–4843.

Buzsaki G (2002) Theta oscillations in the hippocampus. Neuron 33:325–340.

Buzsáki G (2005) Theta rhythm of navigation: link between path integration and landmark navigation, episodic and semantic memory. Hippocampus 15:827–840.

Buzsáki G (2006) Rhythms of the Brain. Oxford University Press, USA.

Crill WE (1996) Persistent sodium current in mammalian central neurons. Annu Rev Physiol 58:349–362.

Csicsvari J, Jamieson B, Wise KD, Buzsáki G (2003) Mechanisms of gamma oscillations in the hippocampus of the behaving rat. Neuron 37:311–322.

Delmas P, Brown D (2005) Pathways modulating neural KCNQ/M (Kv7) potassium channels. Nat Rev Neurosci 6:850–862.

Destexhe A, Marder E (2004) Plasticity in single neuron and circuit computations. Nature 431:789–795.

French CR, Sah P, Buckett KJ, Gage PW (1990) A voltage-dependent persistent sodium current in mammalian hippocampal neurons. J Gen Physiol 95:1139–1157.

Goutagny R, Jackson J, Williams S (2009) Self-generated theta oscillations in the hippocampus. Nat Neurosci 12:1491–1493.

Harris KD, Henze D, Hirase H, Leinekugel X, Dragoi G, Czurkó A, Buzsáki G (2002) Spike train dynamics predicts theta-related phase precession in hippocampal pyramidal cells. Nature 417:738–741.

Hu H, Vervaeke K, Graham LJ, Storm JF (2009) Complementary theta resonance filtering by two spatially segregated mechanisms in CA1 hippocampal pyramidal neurons. J Neurosci 29:14472–14483.

Hu H, Vervaeke K, Storm JF (2002) Two forms of electrical resonance at theta frequencies, generated by M-current, h-current and persistent Na^+ current in rat hippocampal pyramidal cells. J Physiol 545:783–805.

Hu H, Vervaeke K, Storm JF (2007) M-channels (Kv7/KCNQ channels) that regulate synaptic integration, excitability, and spike pattern of CA1 pyramidal cells are located in the perisomatic region. J Neurosci 27:1853–1867.

Hutcheon B, Yarom Y (2000) Resonance, oscillation and the intrinsic frequency preferences of neurons. Trends Neurosci 23:216–222.

Izhikevich EM (2002) Resonance and selective communication via bursts in neurons having subthreshold oscillations. Biosystems 67:95–102.

Kamondi A, Acsady L, Wang X-J, Buzsáki G (1998) Theta oscillations in somata and dendrites of hippocampal pyramidal cells in vivo: Activity-dependent phase-precession of action potentials. Hippocampus 261:244–261.

Lawrence JJ, Saraga F, Churchill JF, Statland JM, Travis KE, Skinner FK, McBain CJ (2006) Somatodendritic Kv7/KCNQ/M channels control interspike interval in hippocampal interneurons. J Neurosci 26:12325–12338.

Leão RN, Tan HM, Fisahn A (2009) Kv7/KCNQ channels control action potential phasing of pyramidal neurons during hippocampal gamma oscillations in vitro. J Neurosci 29:13353–13364.

Li M, West JW, Catterall WA, Scheuer T (1992) Functional Modulation of Brain Sodium Channels by CAMP-Dependent Phosphorylation preparations neurons. Neuron 8:1151–1159.

Lisman J (2005) The theta/gamma discrete phase code occuring during the hippocampal phase precession may be a more general brain coding scheme. Hippocampus 15:913–922.

Lubenov E V, Siapas AG (2009) Hippocampal theta oscillations are travelling waves. Nature 459.

Ma JY, Catterall W, Scheuer T (1997) Persistent Sodium Currents through Brain Sodium Channels Induced by G Protein βγ Subunits. Neuron 19:443–452.

Ma JY, Li M, Catrerall WA, Scheuer T (1994) Modulation of brain Na^+ channels by a G-protein-coupled pathway. 91:12351–12355.

Magistretti J, Alonso a (1999) Biophysical properties and slow voltage-dependent inactivation of a sustained sodium current in entorhinal cortex layer-II principal neurons: a whole-cell and single-channel study. J Gen Physiol 114:491–509.

Mantegazza M, Yu FH, Powell AJ, Clare JJ, Catterall W a, Scheuer T (2005) Molecular determinants for modulation of persistent sodium current by G-protein betagamma subunits. J Neurosci 25:3341–3349.

Marder E, Goaillard J-M (2006) Variability, compensation and homeostasis in neuron and network function. Nat Rev Neurosci 7:563–574.

Marrion N V (1997) Control of M-current. 10:483–504.

Moore SD, Madamba SG, Joels M, Siggins GR, Moore SD, Jorls M (2014) Somatostatin Augments the M-Current in Hippocampal Neurons. 239:278–280.

Moore SD, Schweitzer P (1994) Voltage-dependent effects of opioid peptides on hippocampal CA3 pyramidal neurons in vitro. J Neurosci 74:809-820.

Notomi T, Shigemoto R (2004) Immunohistochemical localization of I_h channel subunits, HCN1-4, in the rat brain. J Comp Neurol 471:241–276.

O'Keefe J, Recce ML (1993) Phase relationship between hippocampal place units and the EEG theta rhythm. Hippocampus 3:317–330.

Pape H, Driesang RB (1998) Ionic Mechanisms of Intrinsic Oscillations in Neurons of the Basolateral Amygdaloid Complex. J Neurophysiol 79:217–226.

Parri HR, Crunelli V (1998) Sodium Current in Rat and Cat Thalamocortical Neurons : Role of a Non-Inactivating Component in Tonic and Burst Firing. 18:854–867.

Peters HC, Hu H, Pongs O, Storm JF, Isbrandt D (2005) Conditional transgenic suppression of M channels in mouse brain reveals functions in neuronal excitability, resonance and behavior. Nat Neurosci 8:51–60.

Prescott S a, Ratté S, De Koninck Y, Sejnowski TJ (2008) Pyramidal neurons switch from integrators in vitro to resonators under in vivo-like conditions. J Neurophysiol 100:3030–3042.

Schweitzer P (2000) Cannabinoids Decrease the K^+ M-Current in Hippocampal CA1 Neurons. J Neurosci 20:51–58.

Schwindt PC, Crill WE (1995) Amplification of Synaptic Current by Persistent Sodium Conductance in Apical Dendrite of Neocortical Neurons. 74.

Shah MM, Migliore M, Valencia I, Cooper EC, Brown D (2008) Functional significance of axonal Kv7 channels in hippocampal pyramidal neurons. Proc Natl Acad Sci U S A 105:7869–7874.

hah MM, Mistry M, Marsh SJ, Brown D, Delmas P (2002) Molecular correlates of the M-current in cultured rat hippocampal neurons. J Physiol 544:29–37.

Stuart G (1999) Voltage-activated sodium channels amplify inhibition in neocortical pyramidal neurons. 2:144-150.

Stuart G, Sakmann B (1995) Amplification of EPSPs by axosomatic sodium channels in neocortical pyramidal neurons. Neuron 15:1065–1076.

Vervaeke K, Hu H, Graham LJ, Storm JF (2006) Contrasting effects of the persistent Na+ current on neuronal excitability and spike timing. Neuron 49:257–270.

3.4 Neuronal resonance in a network context: Impact of the high conductance state.

The data presented in this section is unpublished and is a draft manuscript written by Jorge Vera in preparation for submission to a peer-reviewed journal:

Vera J., Pereira U., Reynaert B., Bacigalupo J. and Sanhueza M. (2014) Modulation of neuronal resonance by changes in the membrane input resistance.

Recent investigations have reported that the context that a neuron faces in the intact brain is remarkably different to what has been characterized under *in vitro* conditions. In order to understand if resonant neurons are able to express their frequency preference under a naturalistic context we investigated the response of resonant behavior under *in vivo*-like conditions. Far from impair resonance, when studied under in vivo conditions, we found that resonance becomes a mechanism that allows a dynamic tuning of frequency preference according to the level of network activity.

3.4.1 Abstract

Neurons from different mammalian brain regions (including neocortex, hippocampus and amygdala) display subthreshold frequency preference in the theta range (4-12 Hz) when stimulated with oscillatory current injection, a phenomenon called neuronal resonance. It is speculated that this property may contribute to tune and to stabilize oscillatory activity in neuronal networks. Subthreshold frequency preference results from the high-pass filter effect produced by the slow activation of a hyperpolarization-

activated depolarizing current in addition to the low-pass filtering of voltage fluctuations due to the passive membrane properties (resistance and capacitance). Together, these properties determine the impedance profile of neurons, characterized by resonance frequency (f_R, frequency at impedance peak), resonance strength (Q-value, ratio between peak impedance and impedance at frequencies approaching 0) and phase shift (Φ, the lag of the oscillatory voltage response relative to the input current). In active neuronal networks membrane input resistance (R_{in}) varies in a wide range depending on synaptic bombardment (showing a 0-80% decrease from its value in a silent network). Interestingly, theoretical study of RLC circuits, which have equivalent electric properties to resonant neurons, predicts a co-variation of R_{in} and frequency preference in real neurons. We investigated this relationship on CA1 pyramidal and cortical amygdala (ACo) neurons, two populations of resonant neurons with marked differences in R_{in}. We used rat brain slices, dynamic clamp and the ZAP protocol (injection of an oscillatory current of constant amplitude and linearly increasing frequency; 0-20 Hz). Our results show that in CA1 neurons, a 50% reduction in R_{in} generated by the addition of a virtual leak conductance, increased f_R by 16%, and decreased Q-value by 9% and the phase shift at f_R, Φ_R, by 38%. On the other hand, a 50% increase in R_{in} by the addition of a virtual negative leak conductance produced the opposite effect, decreasing f_R by 20% and increasing Q-value by 9% and Φ_R by 28%. Comparable results were observed in ACo neurons using a similar stimulation protocol. We tested the modulation of frequency preference during spiking in ACo neurons. We showed that selective spiking at 2-4 Hz recorded in control conditions was shifted to 4-10 Hz after a 30% reduction in R_{in}, in agreement with our observations in subthreshold conditions. Notably, under reduced R_{in}

and moderated synaptic noise, conditions that recreate *in vivo* situation, ACo neurons preserve their spiking preference at f_R. These results show that frequency preference of resonant neurons is modulated by changes in R_{in} and suggest that in the intact brain this property may constitute a tuning mechanism to adjust frequency preference of single neurons in interplay with network activity levels.

3.4.2. Introduction

Most mammalian neurons process subthreshold oscillatory inputs resembling a low-pass filter, i.e., displaying a larger voltage response at frequencies near zero with a monotonic decrement of voltage response as frequency increases (Hutcheon and Yarom, 2000). This is a consequence of passive membrane properties (capacitance and resistance). However, neurons present in several brain regions that express the hyperpolarization-activated current, I_h, display a qualitative different subthreshold behavior. When stimulated with oscillatory inputs they respond with a larger voltage response at theta frequency range (4-12 Hz) (Hutcheon and Yarom, 2000; Izhikevich, 2002). This occurs because in most cases I_h activates at membrane potentials hyperpolarized to -70 mV and permeates a net inward current (a mixed K^+ and Na^+ current) that depolarizes the cell with the subsequent current deactivation, thus generating a feedback loop (Biel et al., 2009). Given that the activation time constant (τ) of I_h is of tens of ms, the feedback loop produces the active attenuation of membrane oscillations at frequencies below 8 Hz (corner frequency at $1/2\pi\tau$) (Hutcheon and Yarom, 2000). The interaction of this active high-pass filter with the passive low-pass filter produces a band-pass effect on voltage response with a characteristic bell-shaped impedance profile (Hutcheon and Yarom, 2000). The other membrane current with high-pass filtering properties similar to I_h is the K^+ muscarine-sensitive current, I_M. This current activates by depolarization, remains closed at resting potentials (Wang et al., 1998), and given its activation time constant, also in the range of tens of ms, it attenuates oscillatory voltage responses below 8 Hz (Hu et al., 2002; Vera et al., 2014). In addition to the opposed voltage ranges for activation of I_h and I_M, in hippocampal CA1 pyramidal

neurons their molecular correlates (HCN channels for I_h and KCNQ2/3 channels for I_M) are expressed in different cellular domains, with HCN channels at higher density in the apical dendrite distal to the soma (Notomi and Shigemoto, 2004), and KCNQ2/3 channels selectively expressed at the perisomatic region (Hu et al., 2007). Based on these evidence it has been proposed that these neurons have a spatially complementary filtering mechanism of low frequencies, covering different stratified inputs and the whole subthreshold range (Hu et al., 2009). In analogy to mechanical systems these neurons have been identified as subthreshold resonators, and their frequency of maximal voltage response as resonance frequency, f_R. Another parameter that characterizes the voltage response as a function of frequency of stimulation is the phase shift, Φ, that represents the lag of the voltage response respect to the oscillatory current input. In general, Φ is a negative number (angle) that increases in magnitude with frequency until reaching a plateau above 10-12 Hz, with resonant neurons having a lower Φ magnitude compared to non-resonant neurons. Notably, in resonant cells Φ can take positive values at low frequencies, which means that the voltage wave actually precedes the current stimulus, in agreement with an inductive electric process (Hutcheon and Yarom, 2000).

Traditionally, subthreshold resonance has been studied *in vitro* by using acute brain slices (Llinás, 1988; Puil et al., 1994; Hutcheon et al., 1996; Hu et al., 2002; Erchova et al., 2004; Pape et al., 2011; Ulrich et al., 2011; Vera et al., 2014). Under these conditions mammalian neurons typically have an input resistance (R_{in}) of 50 to 100 MΩ and a resting potential around -60 and -80 mV. In this preparation whole-cell recorded activity is characterized by a low arrival frequency of synaptic inputs, thus reflecting poor network activity. However, intracellular recordings of neurons in waking

animals show that when the brain is active, neurons constantly receive a bombardment of synaptic inputs with a contribution of both inhibition and excitation (Shu et al., 2003). This synaptic noise, as it is called, produces stochastic fluctuations of membrane potential (variance 2-6 mV) together with a 5-10 mV depolarization of average voltage with respect to *in vitro* condition. In addition, a second consequence of the opening of synaptic receptors due to synaptic bombardment is a drop in R_{in} of neurons in a wide range, reaching levels even lower than 20% of what is observed *in vitro* (Destexhe et al., 2001). Since this drop in R_{in} is in fact an increase in membrane conductance, this state of neurons has been denominated as the *high conductance state* (HCS) and describes the real situation of cortical neurons *in vivo* (Destexhe et al., 2003). The increase in conductance reduces the time and space constants of the membrane, which means that neurons integrate inputs in a narrower time window and in a more restricted membrane region, changing their modality of signal processing from an integrator to a coincidence detector mode (Prescott et al., 2008).

While the effect of changes in R_{in} on signal processing in the time domain has been characterized in detail (Bernander et al., 1991; Destexhe et al., 2003; Kumar et al., 2008; Fernandez and White, 2009), the impact of R_{in} variations on frequency-dependent processing remains unexplored.

Using a theoretical equation obtained from the resolution of a phenomenological linearized membrane circuit model for resonance and using physiological cellular values, we predicted that f_R would vary with changes in R_{in}, moving along the theta range (4-12 Hz) in an inverse relation with changes in R_{in}.

To investigate if the changes in R_{in} that occur *in vivo* modify resonant parameters in real neurons we characterized the relationship between R_{in} and resonance in hippocampal pyramidal neurons by using dynamic clamp to mimic the impact of increased synaptic conductances. Our data shows that in real neurons, a modulation of resonance parameters (f_R and Φ) is indeed generated at subthreshold potentials by changes in R_{in}. To evaluate the possibility that frequency preference at the spiking regime could also be modified, we evaluated the impact of R_{in} reduction on resonant neurons from ACo. We chose this second model of resonant neurons for this purpose as they reliably traduce frequency preference to the spiking regime in slice experiments. We confirmed that the modulation of subthreshold frequency preference by R_{in} changes is also applied to the selective firing of resonant neurons. Finally, we recreated a complete high-conductance state by including moderate levels of synaptic noise and found that ACo resonant neurons preserve selective firing under these conditions.

3.4.3. Results

RLC circuit theory predicts a modulation of resonance by input resistance changes.

To investigate the relationship between input resistance and neuronal resonance properties we used an equivalent RLC circuit and its linearized equation for impedance (see Methods). The circuit diagram is showed in Figure 25A and is composed of a capacitor and a resistance wired in parallel, which represent the cellular membrane and leak conductances, respectively, and an inductive branch including an inductor and a resistance connected in series, which represent the contribution of resonant currents (I_h, for example). Feeding this phenomenological model with parameters that represent an average resonant mammalian neuron (C = 80 μF, L =10 MH and R_L = 300 MΩ) allows to explore the shape of the impedance profile as a function of R, the parameter that represents R_{in}. As expected, the reduction of R is accompanied by a decrease in impedance magnitude: for example, peak impedance drops from 160 MΩ to 50 MΩ when R falls from 200 MΩ to 50 MΩ (Fig. 25B). In addition to this straightforward relationship, upon the same reduction in R the equivalent circuit predicts an increase in f_R from 7.2 Hz to 9.8 Hz. Interestingly, modifications of R in the range of the expected variations for R_{in} *in vivo* values (30-300 MΩ) imply that f_R would take values between 12.5 and 6.6 Hz, thus matching the range for theta frequencies (Fig. 25C).

This theoretical result suggests that real resonant neurons might vary their frequency preference by changes in R_{in}. Since previous theoretical analyses do not include non-linear dynamics of real neurons we proceeded to test our prediction on CA1 pyramidal neurons, a well known cellular model of resonant neurons.

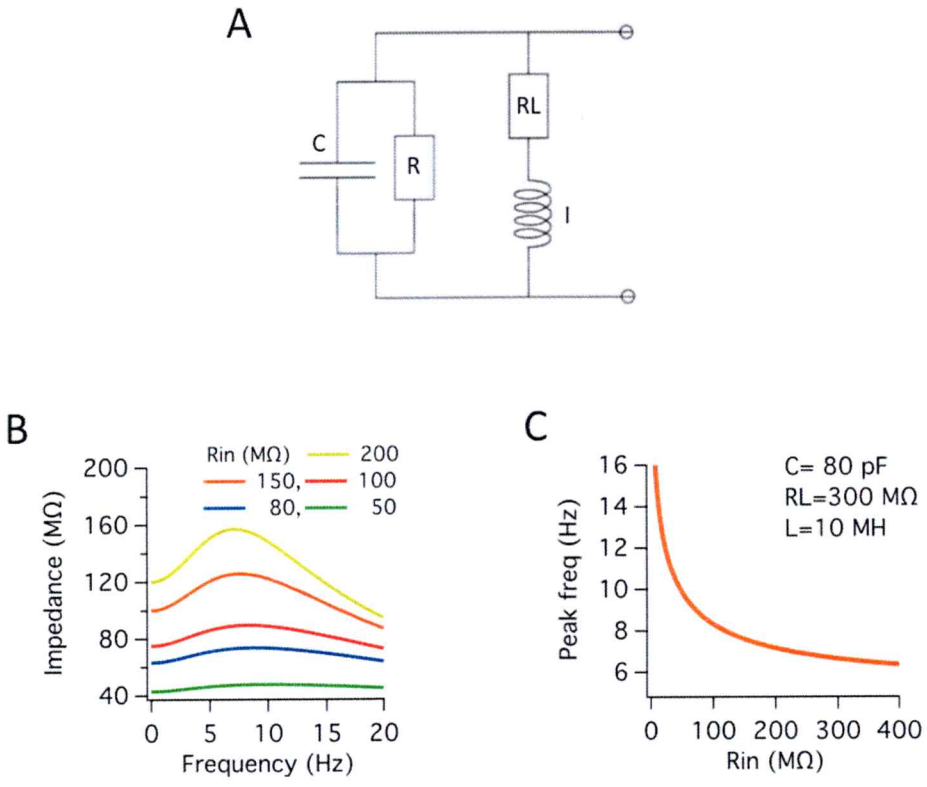

Figure 25. RLC circuit theory predicts a modulation of resonance by input resistance changes. A Diagram of an RLC circuit with equivalent properties to an average resonant neuron with a capacitor (C) and a resistance (R) wired in parallel with the inductor branch composed with an inductor (I) and a resistance (RL). B Impedance profile of the RLC circuit using parameters that reproduce neuronal resonance (C=80 pF, RL=300 MΩ and L=10 MH) and varying the value of R, the RLC equivalent for neuronal R_{in}. C Relationship between the peak frequency of the impedance profile as a function of R, while C, RL and L remain constant.

Modulation of frequency preference by changes in the membrane input resistance in real neurons.

To investigate the dependence of f_R on R_{in} in resonant neurons, we decided to use pyramidal neurons from CA1 hippocampus as a model of resonant neurons, for the following reasons: 1) They have a subthreshold R_{in} around 60-80 MΩ that corresponds to an intermediate magnitude in a mammalian brain, allowing manipulations to increase or decrease R_{in} values while maintaining biological levels of impedance. 2) These neurons have an average f_R of ~ 6 Hz, near the middle of the theta range, making it easier to detect f_R changes in both directions. 3) The mechanism that generates subthreshold resonance has been described in detail in these neurons. 4) It has been shown that the hippocampus works at theta activity during learning processes.

Our strategy to manipulate R_{in} was based on dynamic clamping, by injecting a current that simulated the presence of a leak conductance ($+G$) to reduce R_{in}, or injecting a current that mimicked a virtual negative conductance ($-G$), in order to increase R_{in} (for more details see Methods).

One difficulty that arises when studying the relationship between R_{in} and resonance is that the latter is a voltage-sensitive phenomenon, thus it is necessary to compare all conditions (control, $+G$ and $-G$) for oscillations of the membrane potential at the same voltage range. Because of this, the approach taken to do the experiments was to systematically adjust the amplitude of the sinusoidal current to produce 5-7 mV peak-to-peak oscillations in all conditions, while maintaining membrane potential centered at -80 mV with DC injection.

The criterion for determining the magnitude of the conductance (G) to be added or subtracted, was to increase input resistance by ~150% (-G) and to reduce it by 50% (+G). Figure 26A shows recordings obtained in a representative experiment. At the top of the figure is the voltage response of a neuron that was recorded in control condition and under increased (–G) or reduced R_{in} (+G). Traces below potentials are recordings of the oscillatory current (ZAP current) that was used to stimulate the neuron at each condition. Compared to control the magnitude of the current required to produce a maximum oscillation of 5 mV is lower for -G condition while it is higher for +G (note that the sum of oscillatory current and leak current is constant at the three conditions).

As predicted by the phenomenological circuit, the studied resonant neuron changed its impedance profile. Under increased R_{in} (-G = -5 nS) the impedance profile rises, increasing its peak impedance from 80 to 140 MΩ, and reducing f_R from 6.5 to 5.5 Hz (Fig. 26B) and increasing Φ (Fig. 26C). In turn, the reduction of R_{in} (+G = 15 nS) had the opposite effect, a decrease of impedance profile with a drop of peak impedance from 80 to 35 MΩ, accompanied by an increase of f_R from 6.5 to 7.5 Hz and a reduction of Φ (Figs. 26B, C). The degree of change at impedance profile under both explored conditions is also clearly observed in the plot of complex impedance (Fig. 26D). This graphic shows the real and imaginary components of complex impedance. The impedance magnitude is equal to the length of the vector from the origin to each point, whereas Φ is given by the angle between the vector and the real axis. The frequency is in a third axis orthogonal to the imaginary-real plane, and therefore is not visible. The

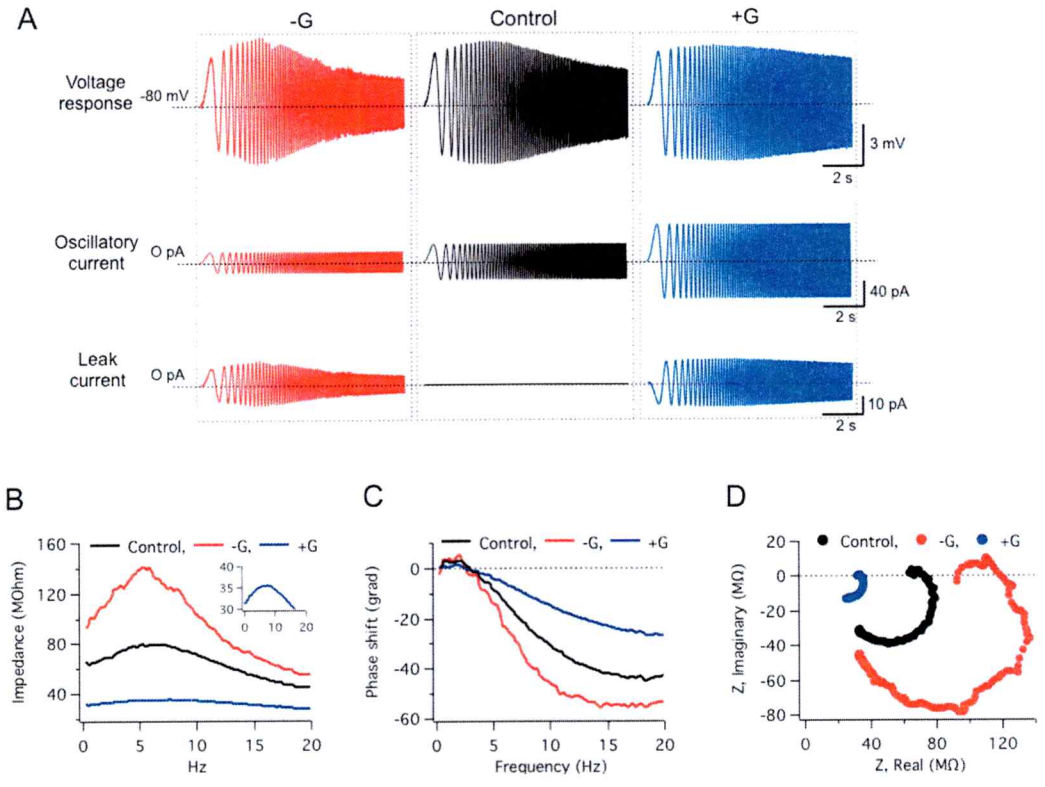

Figure 26. Exploring the effect of R_{in} changes on subthreshold resonance in a hippocampal CA1 neuron. A Voltage response of a hippocampal pyramidal neuron under ZAP stimulation in control condition (black) and after the increment of Rin using a virtual negative leak conductance of -5 nS (*-G*, red) and after the reduction of Rin using a positive leak conductance of +10 nS (*+G*, blue) by means of dynamic clamp. The dynamic current injected at each condition is shown as leak current at the bottom. The amplitude of the oscillatory current (ZAP) was adjusted in order to produce a peak-to-peak voltage response of 5-6 mV at each condition. B Impedance profiles from recordings in A. The inset shows a zoom of the impedance profile at *+G* condition to show that maintains the shape of band-pass filter. C Phase shift of the membrane potential relative to the oscillating input current from experiments in A. D Complex impedance of the experiments in A.

analysis of these plots reveals the high impact on the processing of oscillatory stimuli of changes in R_{in} as those expected to occur *in vivo*.

We repeated this experiment in a total of ten neurons for each condition with all neurons showing the same response. Figure 27A shows the summary of our results displaying the average traces for impedance profile, Φ and complex impedance when R_{in} is increased (Fig. 27A-C) and when it is reduced (Fig. 27D-F). On average, the conductances used to modify R_{in} were -6.1 ± 0.8 nS for $-G$ and 16.6 ± 2.9 nS for $+G$ conditions, respectively. The quantification of resonant parameters showed that the Q-value increased for the $-G$ condition by 9.5% (1.23 ± 0.03 to 1.34 ± 0.05, $p < 0.03$), whereas for $+G$ it falls by 8.7% (from 1.23 ± 0.03 to 1.11 ± 0.02, $p < 0.005$, Fig. 27G). For its part, for $-G$ condition f_R showed a 20% decrease (from 6.5 ± 0.4 to 5.2 ± 0.3 Hz, $p < 0.0005$), while for $+G$ it presented a 16% increase (from 6.3 ± 0.4 to 7.3 ± 0.4 Hz, $p < 0.0005$, Fig. 27H). The changes in R_{in} are reflected by the modifications of peak impedance at each condition, with an increase of 152% at $-G$ (from 89.4 ± 5.1 to 221.6 ± 89.1 MΩ, $p < 0.0005$) and a reduction of 51% at $+G$ (from 90.1 ± 10.1 to 44.1 ± 6.2 MΩ, $p < 0.005$, Fig. 27I).

To evaluate the effect of R_{in} modifications on Φ we measured its value at f_R, Φ_R. When we simulated a high R_{in} ($-G$) we observed that Φ_R increases from -14.1 ± 1.4 to -18.4 ± 2.1 deg ($p<0.005$), whereas it decreases from -13.8 ± 1.7 to -8.6 ± 0.5 deg at $+G$ condition ($p<0.005$, Fig. 27J).

To summarize our results we plotted the average impedance profile obtained at each condition, normalized with respect to their peak value to appreciate the shift in frequency preference and the change in the shape of impedance curve at $-G$ and $+G$ conditions (Fig. 28A). This plot shows that when R_{in} is reduced the increase in f_R is

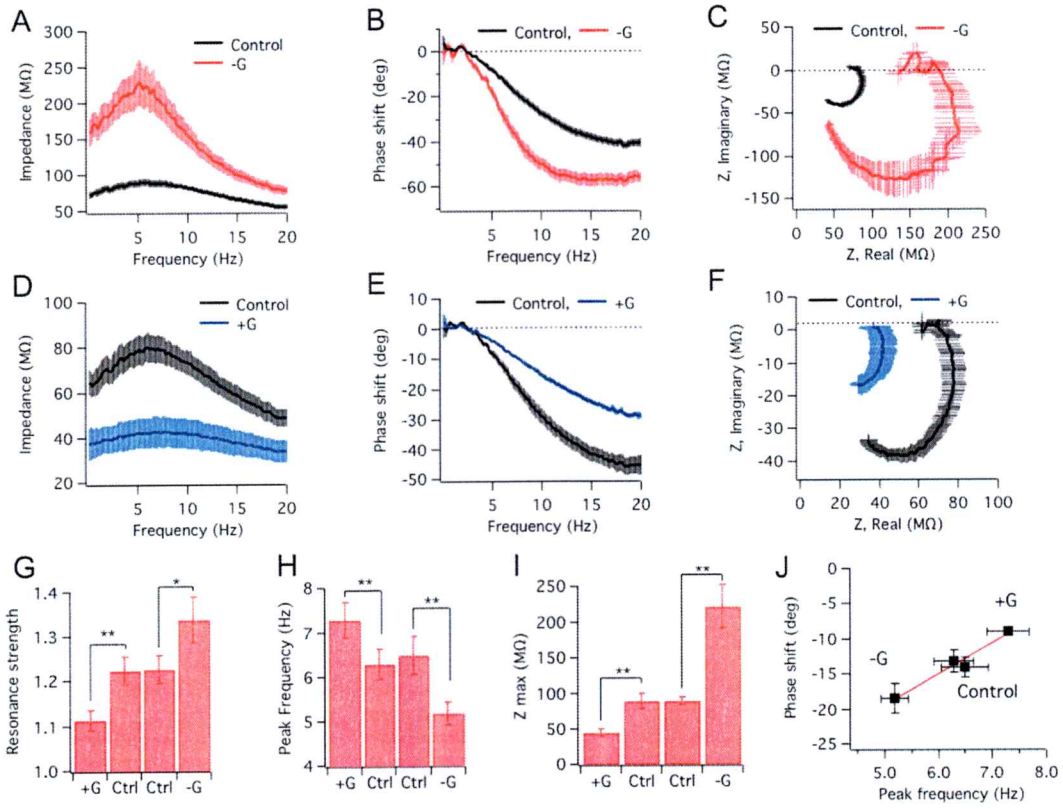

Figure 27. The virtual increase or reduction of R_{in} modulates subthreshold resonance in hippocampal CA1 neuron. Average results for experiments of increase or reduction of R_{in} by means of virtual conductances. A-C Effect of an increase in R_{in} using a virtual negative conductance ($-G$) of -6.1 ± 0.8 nS (avg ± sem) on the impedance profile (A), phase shift (B) and complex impedance (C) (n=10). D-F Effect of a reduction in R_{in} using a virtual positive conductance ($+G$) of 16.6 ± 2.9 nS (avg ± sem) on the impedance profile (D), phase shift (E) and complex impedance (F) (n=10). G-H Quantification of resonance parameters observed at $+G$ and $-G$ conditions, resonance strength (G), peak frequency (H), peak impedance (I) and phase shift at the peak frequency (J) (* $p < 0.05$, ** $p < 0.005$).

accompanied with a widening of impedance profile reflecting a reduction of frequency selectivity, i.e., of resonance strength (in agreement with Q-values showed in Fig. 27G). Since resonance strength quantifies the frequency tuning of a resonant neuron, the opposed relationship between f_R and Q-value during R_{in} changes shows that within the theta range, low f_R will be accompanied by a high strength, while high f_R by a lower strength. Therefore, besides the high dependence of f_R on R_{in} (Fig. 28B), the global influence of R_{in} on frequency preference will be determined by the actual range of values taken by Q in a specific cell type in an active network, The reduction of resonance impact (Q-value), that occurs concomitant to an increase in f_R, is negative in terms of frequency selectivity, however our results show that on average Q is still higher than 1.1 (Fig. 27G). Moreover, it is accompanied with a reduction in the phase lag of voltage response, which is favorable as it reduces the response time to the generation of coordinated network activity.

Another interesting point that arises from this investigation is the correlation between the f_R of different groups of theta-range resonant neurons and their value of R_{in}. Figure 28C shows a R_{in} vs f_R plot for resonant neurons from ACo, CA1 pyramidal neurons and stellate neurons from layer II of entorhinal cortex. For the latter cell type the data was obtained from the literature (Erchova et al., 2004). The plot shows that the relationship between R_{in} and f_R in these three resonant cell groups resembles what is observed in CA1 pyramidal neurons after varying R_{in}. Since in these three groups of cells resonance at hyperpolarized potentials is produced by the same mechanism (hyperpolarization-activated current, I_H), it is possible to explain, at least in part, their distinct f_R based on their differences in R_{in} (probably resulting from their different soma size). Interestingly,

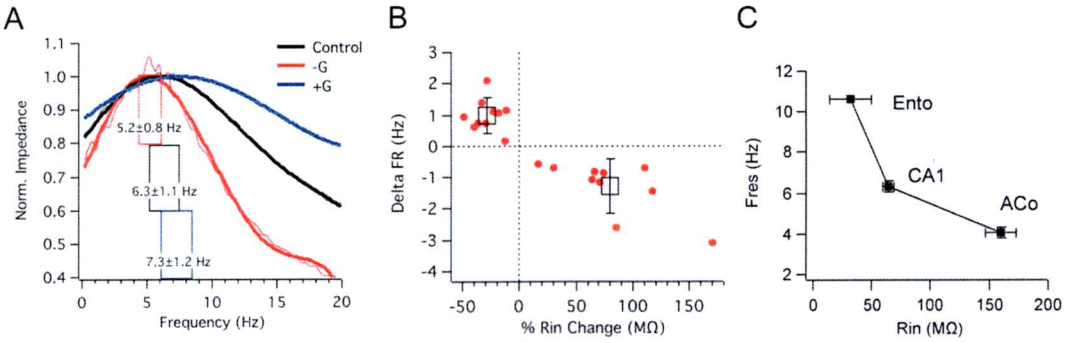

Figure 28. Resonant frequency (f_R) is inversely correlated with R_{in}: comparison between different types of neurons of the rat brain. Figures A and B summarize results obtained with dynamic current injection. A normalized average impedance profiles obtained at control, $+G$ and $-G$ conditions (shown in Figure 26). The average resonant frequency obtained in each condition is displayed. B Co-variation ratio of R_{in} and f_R (showed in Fig.26). C values of R_{in} and f_R for three mammalian resonant neurons: ACo neurons (n = 30), CA1 hippocampus (n = 20) and entorhinal cortex. Values for this later group were obtained from the literature (Erchova et al, 2004).

despite the strong relationship with f_R, the average Q-value for each cell group does not display a clear trend when comparing R_{in} and resonance strength, with ACo and hippocampal neurons having an average Q-value of 1.2 (Fig. 2C and 27G, respectively), while entorhinal neurons with a lower R_{in} (higher f_R) have a higher Q, around 1.5. This evidence suggests that there are more variables involved in the setting of resonance, as for example the density of HCN channels.

Modulation of frequency preference in the spiking regime

In Section 3.1.1 we showed that resonant neurons from layer II of ACo translate their subthreshold frequency preference to a spiking regime (Fig. 7). With the aim of investigating whether modulation of resonance by changes in R_{in} is maintained when neurons are selectively firing at their preferred frequency, we first corroborated the modulation at subthreshold levels in ACo neurons. As we did with hippocampal neurons, we injected by dynamic clamping a leak current modeled as a constant conductance (+*G* condition), to decrease input resistance by 30-50%, producing a clear reduction in the magnitude of voltage oscillations (average +*G* was 6.8 ± 0.7 nS, n = 11, Fig. 29A-B).

The comparison of impedance profiles using the ZAP protocol at -80 mV in control and +*G* condition confirmed the drop in peak impedance (from 112 to 68 MΩ) and the increase in f_R (from 2.5 ± 0.3 Hz to 3.2 ± 0.5 Hz, $p < 0.05$, t-test, n = 7, Fig. 29C-E), ratifying that the modulation also occurred in this neuronal type.

Once we corroborated the existence of the modulatory mechanism we focused in investigating the spiking regime. To facilitate the analysis and also an online observation

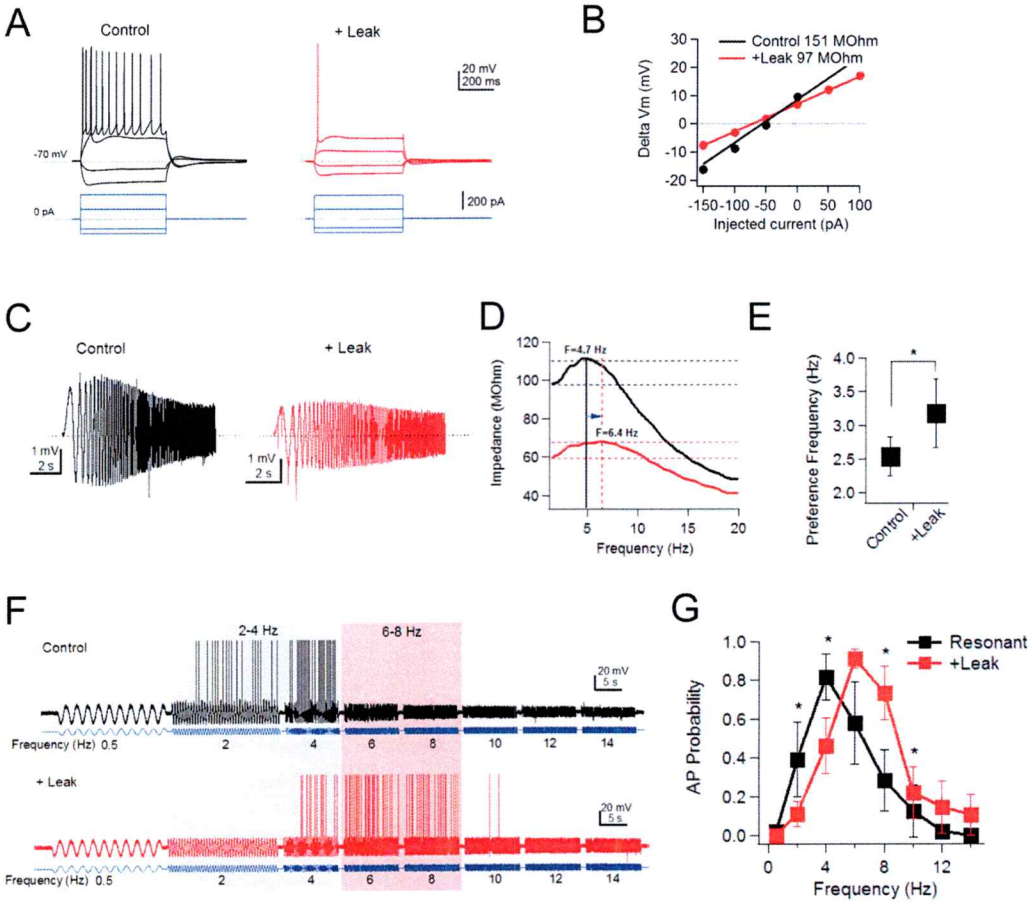

Figure 29. The modulation of subthreshold resonance by changes in R_{in} is expressed under spiking regime in ACo neurons. A voltage response of a resonant ACo neuron in control condition (black) and after adding a virtual constant conductance ($+G$) by dynamic clamping that produces a 30% drop in R_{in}. Note that in both conditions current pulses of equal magnitude (blue lines) are applied. B Current-voltage relationship of recordings in A showing the reduction of R_{in} expressed as a reduction in the slope of the curve. C Voltage response of an ACo resonant neurons under the ZAP protocol in control and $+G$ condition. In both conditions the amplitude of the stimulus was the same 10 pA. D Impedance profile from recordings in C, showing the positive shift of f_R under +G condition from 4.7 to 6.4 Hz. E Average f_R values in control and $+G$ condition in ACo resonant neurons (n = 7). F Voltage response of a resonant ACo neuron under stimulation with oscillatory current (blue) at control (black) and $+G$ (red) conditions. Stimulation protocol consisted in 10 s steps of discrete frequency at: 0.5, 2, 4, 6, 8, 10, 12 and 14 Hz (stimulation at 0.5 and 2 Hz last 20 s in order to sample more periods). Colored area show the firing frequency range at control (black) and $+G$ condition (red). G Firing probability vs frequency of stimulation curve from recordings in F. The probability was calculated by dividing the number of action potentials by the total number of cycles at each frequency step (n=7).

of the phenomenon by watching the oscilloscope, we changed the protocol of oscillatory current stimulation while maintaining the same nature of the stimuli. For this experiment the stimulation protocol consisted on an oscillatory current of constant (instead of linearly-increasing) frequency that was applied at 0.5, 2, 4, 6, ... up to 14 Hz. Neurons were depolarized to -60 mV and then the amplitude of the oscillatory current needed to see preferential firing was explored (see Methods). Figure 29F shows a representative recording of these experiments. At control condition neurons fired action potentials typically at frequencies between 2-4 Hz with no or scarce spiking activity at other frequencies. When the $+G$ condition was active neurons systematically changed their firing preference towards higher frequencies (Fig. 29F). The average result shows that the frequency for peak firing probability incremented from 4 to 6 Hz in $+G$ condition, reducing the firing probability at 4 Hz from 0.82 ± 0.12 to 0.46 ± 0.14 ($p<0.05$, n=7), and increasing at 6 Hz from 0.59 ± 0.21 to 0.91 ± 0.05 ($p=0.52$, n=7). In general, under $+G$ condition the firing probability decreased for 2-4 Hz and increased for 8-10 Hz, showing an overall shift of the firing probability curve towards higher frequencies (Fig. 29G).

These results confirm that the dependence of f_R on R_{in} is preserved during the translation of subthreshold frequency preference to a spiking regime. The implications for these observations are attractive, since they make it possible that the changes in R_{in} produced by synaptic activity *in vivo* are able to modulate the intrinsic frequency preference of resonant neurons, not only at subthreshold potentials, but also while this neurons fire action potentials selectively at their preferred frequency.

As the final step of this investigation, we decided to assess how strong is neuronal resonance for translating subthreshold frequency preference to spiking under a noisy oscillatory stimulation in order to challenge resonance in *in vivo* conditions.

Preservation of selective firing under recreated high-conductance state

It has been described both theoretically and empirically that the synaptic bombardment that neurons receive in active networks during a HCS profoundly affects their excitability, due to the reduction in membrane resistance and the incorporation of noise to membrane potential fluctuations (Bernander et al., 1991; Destexhe et al., 2003). This noise produces a qualitatively different scenario in the interaction between subthreshold oscillations and the mechanism of action potential initiation, as it incorporates a previously ignored stochastic component to the firing of action potentials, changing the traditional view of cell activity from a deterministic to a probabilistic conception (Ermentrout et al., 2008). It is possible that the effect of noise could disturb the translation of subthreshold frequency preference to spiking. To be a meaningful phenomenon *in vivo*, resonance should tolerate certain levels of synaptic noise without losing frequency selectivity, particularly for firing at the preferred frequency.

To investigate how resistant to synaptic noise is the translation of subthreshold frequency preference to spiking regime we implemented a computational model that recreates synaptic noise based on the average uncorrelated activity of a population of neurons (see Methods). It has been demonstrated that using dynamic clamp and an appropriate computational model it is possible to reproduce the effect of HCS on single neuron excitability (the increase in average membrane conductance and incorporation of

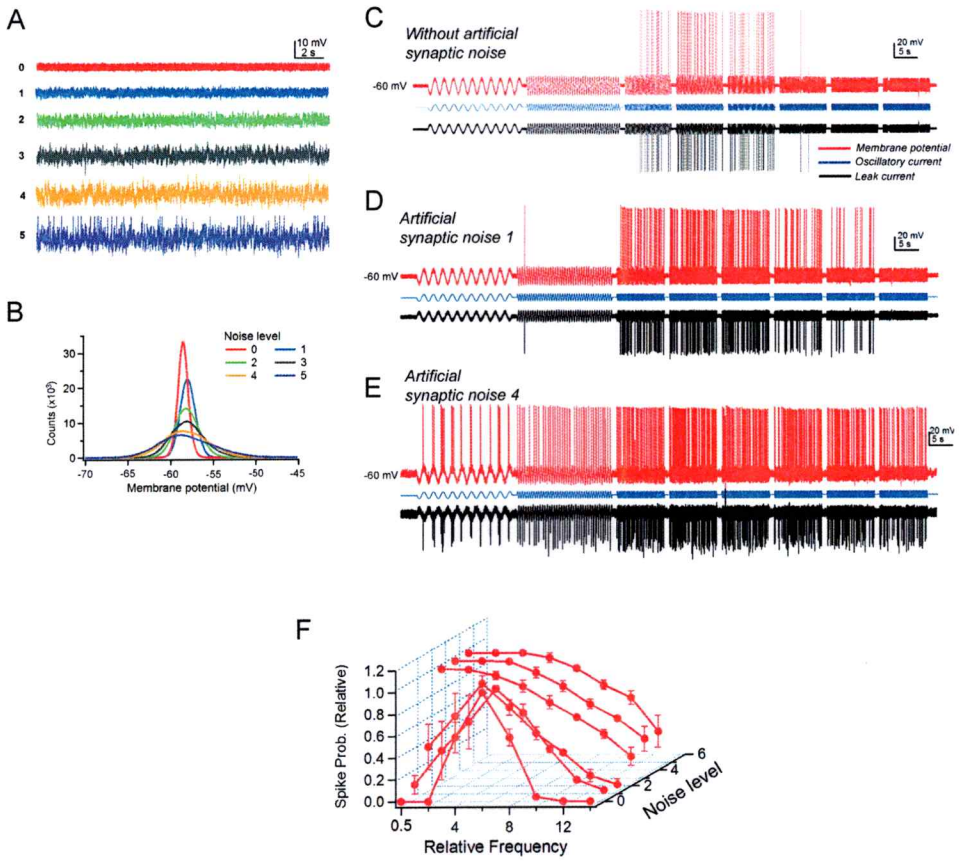

Figure 30. Resonant ACo neurons preserve their firing at preferred frequency under recreated high-conductance state. A Voltage response of a resonant ACo neuron displaying increasing level of recreated synaptic noise by means of dynamic clamp. We studied five increasing levels of synaptic noise, from moderate levels (blue and green) to exaggerate levels (yellow and violet) in addition to control condition which had zero added noise (red) (for details see main text). B Histogram showing the membrane potential distribution of traces in A. C-D Experiment directed to determine the impact of the synaptic noise on the preference of firing frequency on resonant neurons. Membrane potential is shown in red, the stimulation current in blue and the total current injected as synaptic noise in black. Frequency selectivity was studied using an oscillatory current injection (blue) at constant frequency steps at 0.5, 2, 4, 6, 8, 10, 12 and 14 Hz with 20 s (0.5-2 Hz) or 10 s (4-14 Hz) of duration. In each experiment G_{avg} was adjust to produce a consistent 30-50% drop in R_{in} and then the oscillatory current protocol was applied under control condition and with the increasing level of noise. C Voltage response in control condition (without synaptic noise). D Voltage response at the first level of noise studied. E Voltage response at the 4th level of noise studied. F Firing probability curve as a function of frequency of stimulation and synaptic noise level (n = 4). The firing probability was calculated by dividing the number of action potentials by the number of periods for each frequency step.

noise in the membrane potential, see Methods) (Destexhe et al., 2001), and thus we will use this methodology to explore the sensitivity of resonance to noise.

The computational model we developed to mimic the HCS by dynamic clamping was based on published work (Destexhe et al., 2001) and operates with two independent variables, one corresponding to an average conductance value, G_{avg} (a stationary value that does not vary over time) and a fluctuating conductance simulated according to the standard deviation of the normal distribution of noise that describe an stochastic process, σ_G (Destexhe et al., 2001).

The experiment design consisted in depolarizing the cells up to -60 mV by application of a constant DC current and then injecting sinusoidal currents of different frequencies between 0.5 and 14 Hz to generate the oscillatory regime (as in previous section). We introduced a constant G_{avg} designed to reduce R_{in} by a 30-50 % and then we explored the firing probability of the cells for different σ_G values. Since the R_{in} of each neuron is different and therefore the voltage response to a given stimulus is different, the rationale to set the maximum σ_G was to induce membrane fluctuations with a σ_{Vm} of 3-4 mV, and then exploring 4 intermediate values for σ_G. With this criterion the resultant σ_G was 56 ± 25 pS for the lowest level, and 11 ± 2.4 pS for the increment at each consecutive step (n = 7). Figure 30A shows a family of voltage responses obtained at the different noise levels (in absence of oscillatory stimulation, for clarity). The noise in the membrane potential gradually increased from zero to the maximum, condition at which most neurons fired action potentials (Fig. 28A violet trace, spikes were cut). A histogram of membrane potential traces shows the increment of the σ_{Vm} at each condition (Fig. 30B).

When inserting a constant conductance without synaptic noise (σ_G = 0 pS), neurons reached spike threshold and fired action potentials at a preferred theta frequency, typically between 4 and 8 Hz (Fig. 30C). After the incorporation of the noise component to the modeled HCS (σ_G > 0 pS) neurons began to fire spikes in a wide frequency range as the noise increases (Fig. 30D and E). To evaluate the frequency selectivity at different noise levels, we measured the firing probability at each frequency of stimulation, constructing a firing probability curve for each noise level (for details see Methods). In the absence of noise the selectivity for spiking at the 4-8 Hz is clear (Fig. 30F, n=7). As expected, the incorporation of the noise component produced a detriment in the firing frequency selectivity, expressed as a widening in the firing probability curve as the noise increases. Nevertheless, the firing selectivity is maintained for the first two levels of noise studied, showing that resonant neurons from the cortical amygdala preserve their firing selectivity at moderate noise levels similar to the levels reported *in vivo* (Destexhe et al., 2003).

3.4.4. Discussion

Since the description of resonance in mammalian brain, this intrinsic frequency preference of neurons has been considered as a stable intrinsic phenomenon, characterized by a given f_R, Q-value and Φ (Hutcheon and Yarom, 2000; Izhikevich, 2002). Aside subtle changes of resonant parameters due to their voltage dependence or after an increase in the magnitude of resonant conductances with LTP induction (Narayanan and Johnston, 2007), resonance has not been considered as a possible mechanism for rapid tuning of frequency preference. Here we show experimental data that relate natural variations of R_{in} to changes in the parameters of resonance, thus generating a new view of neuronal frequency preference as an adjustable or tunable rather than fixed phenomenon. The possible functional implication for this interdependence becomes relevant as it is known that in the intact brain the membrane R_{in} of neurons is highly modified by the opening of postsynaptic receptors under sustained synaptic activity, producing a change of R_{in} from 100 to even a 20% of the values observed *in vitro* (Destexhe et al., 2003). This new scenario is very exciting because the common biological range for somatic R_{in} in resonant neurons, which is in the order of 30 to 300 MΩ, implies that the dynamic range for resonance modulation lies particularly at theta range (4-12 Hz), a well characterized frequency range associated with a working brain (navigation, episodic memory) (Buzsáki, 2005; Hasselmo, 2005; Pape et al., 2005; Buzsáki and Moser, 2013). When neurons face a reduction in their R_{in} generated by synaptic stimulation, their f_R increases while their Q-value and Φ change in the opposite direction, responding with a reduction. This means that under intense synaptic input resonant neurons change their preference to a higher theta frequency,

decrease their resonance strength and respond with a lower phase lag. The reduction of resonance strength concomitant to increases on f_R generate a loss of frequency selectivity with higher f_R, suggesting that for all resonant cell types the f_R has an upper limit (physical constrain) above which neurons loose frequency preference. Interestingly, according to RLC theory and experimental data, the range at which f_R maintains frequency selectivity matches the theta range. Together with the increases in f_R, the reduction in response lag allows resonant neurons to respond faster to oscillatory inputs when f_R gets higher. Our experimental results show that the response lag is reduced from 6 to 3 ms with a 50% reduction in R_{in} (considering a 7 Hz stimulation). Supposing a dynamically changing frequency of network activity, which may be the case in a working brain, this inverse correlation between frequency preference and phase shift may act as a natural constrain decreasing time lag when network activity is faster, thus ensuring the maintenance of coordinated oscillatory activity.

This relationship between R_{in} and resonance implies that neurons with higher R_{in} should display a larger dynamic range for f_R modulation while maintaining a high Q value. For this reason ACo resonant neurons where chosen as the appropriate model to investigate the maintenance of frequency preference modulation under spiking regime.

It is important to have in mind that the level of modulation observed with our experimental approach should be an underestimation since we focused on the somatic filtering of oscillatory stimulation. In natural conditions the high density of I_h present in dendrites should increase resonance strength constituting a strong active filter of synaptic inputs that allow travel from dendrites to the soma. The impact of the modulation of resonance by changes in R_{in} directly in dendrites, where synaptic inputs

are processed by active properties before arrive to the somatic region, remain unexplored and is a topic that we will investigate by means of computer simulations. Another important phenomenon that arise as an attractive topic at the light of this investigation is the impact of the modulation of resonance on the processing of back propagated action potentials and their related spike time dependent plasticity (STDP). Given the high amplitude, their rhythmicity at frequency range and their localization at dendritic domain, make possible that this tuning mechanism for selective processing can drive LTP processes in a frequency-dependent manner.

Another interesting idea arises from the comparison between the different neuronal types that have resonance in theta range. It is noteworthy that ACo neurons, hippocampal pyramidal neurons and entorhinal stellate neurons display a correlation between the input resistance and the resonant frequency (Figure 28C). Being quite different cell types one from each other, this observation suggests an important role of their input resistance (and its dynamic changes in the intact brain), in the determination of the functional impact of the resonance.

Finally, since different levels of network activity are expressed as variations of neuronal conductance we propose that neuronal resonance represents a tunable mechanism to set intrinsic frequency preference and neuronal responsiveness into the theta range. This setting is dynamic and changes according to the levels of synaptic activity.

3.4.5 References

Bernander O, Douglas RJ, Martin K, Koch C (1991) Synaptic background activity influences spatiotemporal integration in single pyramidal cells. Proc Natl Acad Sci U S A 88:11569–11573.

Biel M, Wahl-schott C, Michalakis S, Zong X (2009) Hyperpolarization-Activated Cation Channels : From Genes to Function. :847–885.

Buzsáki G (2005) Theta rhythm of navigation: link between path integration and landmark navigation, episodic and semantic memory. Hippocampus 15:827–840.

áki G, Moser EI (2013) Memory, navigation and theta rhythm in the hippocampal-entorhinal system. Nat Neurosci 16:130–138.

Destexhe A, Rudolph M, Fellous JM, Sejnowski TJ (2001) Fluctuating synaptic conductances recreate in vivo-like activity in neocortical neurons. Neuroscience 107:13–24.

Destexhe A, Rudolph M, Pare D (2003) The high-conductance state of neocortical neurons in vivo. Nat Rev Neurosci 4:739–751.

Erchova I, Kreck G, Heinemann U, Herz a VM (2004) Dynamics of rat entorhinal cortex layer II and III cells: characteristics of membrane potential resonance at rest predict oscillation properties near threshold. J Physiol 560:89–110.

Ermentrout GB, Galán RF, Urban N (2008) Reliability, synchrony and noise. Trends Neurosci 31:428–434.

Fernandez FR, White J (2009) Reduction of spike afterdepolarization by increased leak conductance alters interspike interval variability. J Neurosci 29:973–986.

Hasselmo ME (2005) What is the function of hippocampal theta rhythm?--Linking behavioral data to phasic properties of field potential and unit recording data. Hippocampus 15:936–949.

Hu H, Vervaeke K, Graham LJ, Storm JF (2009) Complementary theta resonance filtering by two spatially segregated mechanisms in CA1 hippocampal pyramidal neurons. J Neurosci 29:14472–14483.

Hu H, Vervaeke K, Storm JF (2002) Two forms of electrical resonance at theta frequencies, generated by M-current, h-current and persistent Na+ current in rat hippocampal pyramidal cells. J Physiol 545:783–805.

Hu H, Vervaeke K, Storm JF (2007) M-channels (Kv7/KCNQ channels) that regulate synaptic integration, excitability, and spike pattern of CA1 pyramidal cells are located in the perisomatic region. J Neurosci 27:1853–1867.

Hutcheon B, Miura RM, Puil E (1996) Subthreshold membrane resonance in neocortical neurons. J Neurophysiol 76:683–697.

Hutcheon B, Yarom Y (2000) Resonance, oscillation and the intrinsic frequency preferences of neurons. Trends Neurosci 23:216–222.

Izhikevich EM (2002) Resonance and selective communication via bursts in neurons having subthreshold oscillations. Biosystems 67:95–102.

Kumar A, Schrader S, Aertsen A, Rotter S (2008) The high-conductance state of cortical networks. Neural Comput 20:1–43.

Llinás RR (1988) The intrinsic electrophysiological properties of mammalian neurons: insights into central nervous system function. Science 242:1654–1664.

Narayanan R, Johnston D (2007) Long-term potentiation in rat hippocampal neurons is accompanied by spatially widespread changes in intrinsic oscillatory dynamics and excitability. Neuron 56:1061–1075.

Notomi T, Shigemoto R (2004) Immunohistochemical localization of Ih channel subunits, HCN1-4, in the rat brain. J Comp Neurol 471:241–276.

Pape H, Driesang RB, Popescu AT, Paré D, Rainnie G (2011) Ionic Mechanisms of Intrinsic Oscillations in Neurons of the Basolateral Amygdaloid Complex. :217–226.

Pape H-C, Narayanan RT, Smid J, Stork O, Seidenbecher T (2005) Theta activity in neurons and networks of the amygdala related to long-term fear memory. Hippocampus 15:874–880.

Prescott S, Ratté S, De Koninck Y, Sejnowski TJ (2008) Pyramidal neurons switch from integrators in vitro to resonators under in vivo-like conditions. J Neurophysiol 100:3030–3042.

Puil E, Meiri H, Yarom Y (1994) Resonant behavior and frequency preferences of thalamic neurons. J Neurophysiol 71:575–582.

Shu Y, Hasenstaub A, Badoual M, Bal T, McCormick D (2003) Barrages of synaptic activity control the gain and sensitivity of cortical neurons. J Neurosci 23:10388–10401.

Ulrich D, Dembrow NC, Chitwood RA, Johnston D, Neurophysiol J, Wang X, Hu H, Vervaeke K, Graham LJ, Storm JF (2011) Dendritic Resonance in Rat Neocortical Pyramidal Cells Dendritic Resonance in Rat Neocortical Pyramidal Cells. :2753–2759.

Vera J, Pezzoli M, Pereira U, Bacigalupo J, Sanhueza M (2014) Electrical Resonance in the θ Frequency Range in Olfactory Amygdala Neurons. PLoS One 9:e85826.

Wang HS, Pan Z, Shi W, Brown BS, Wymore RS, Cohen IS, Dixon JE, McKinnon D (1998) KCNQ2 and KCNQ3 potassium channel subunits: molecular correlates of the M-channel. Science 282:1890–1893.

Chapter 4

DISCUSSION

In this thesis we investigated a possible role of subthreshold theta-resonance in the frequency-dependent neural processing of two brain regions involved in memory and known to develop theta waves during exploratory behavior. In this context, the key points were to evaluate if theta-resonant neurons translate their subthreshold frequency preference to a spiking regime in rat brain slices, what are the mechanisms involved in this process and finally, what is the real impact of theta-resonance under *in vivo*-like conditions.

If our aim is to understand if resonance (i.e. the intrinsic frequency preference of neurons) contributes to the selective propagation of theta-frequency activity to downstream cells and thus to the generation of the oscillatory activity observed in the active brain, it is necessary to characterize in detail the synaptic input that resonant neurons process. Since the most characterized theta-resonant neurons from mammalian brain, pyramidal neurons from CA1 hippocampus and stellate cells from layer II entorhinal cortex, belong to multisensory processing brain regions, the precise temporal

structure of their synaptic inputs is unknown. This problem is overcome at some point in the case of resonant neurons from ACo, region that is an integral part of the olfactory circuit and receives rhythmic synaptic activity from OB afferents.

Given that resonance is a resistive property it is expected that resonant neurons that have high input resistance (R_{in}) will favor the impact of resonance under *in vitro* and *in vivo*-like conditions. For this reason we decided to use resonant neurons from ACo as a model system. Since those neurons where poorly characterized we also used hippocampal CA1 pyramidal neurons as a reference, considering that they are a widely described cell type and that they present significantly lower R_{in}.

The importance and convenience of the characterization of a new group of theta-resonant cells, with the aforementioned advantages of ACo neurons, is that this may allow to shed light to the question about how conserved are theta-resonant neurons in the mammalian brain, how effective and general is the translation of subthreshold frequency preference to spiking regime and what is the underlying mechanism. Finally, a very relevant point is to assess the impact of theta-resonance under *in vivo*-like conditions for the different cell types.

Since a detailed discussion of each of the objectives was given in the different chapters included in the result section, here we will discuss the general insights that were developed after addressing the question exposed above.

4.1 How general are properties of theta-resonant neurons?

The similarities in morphology and intrinsic properties between CA1 pyramidal neurons and entorhinal stellate cells, and also in the mechanism behind theta-resonance with both

neurons expressing I_h and I_M, make attractive the idea to generalize and speculate that all theta-resonant neurons share those properties. Our study of the ionic mechanism implemented in ACo resonant neurons showed it is mainly based on I_h (Fig. 4, 5A). We also observed the presence of I_M in some neurons (Fig. 5B), but this was not a consistent characteristic across all resonant cells, in contrast to what has been described for CA1 pyramidal neurons (Halliwell and Adams, 1982; Hu et al., 2002), results that we corroborated (Fig. 21). This variability in the presence of resonant current has also been observed in stellate cells from entorhinal cortex (Boehlen et al., 2013), thus showing that the constancy in the expression of both resonant currents is representative only of CA1 pyramidal neurons.

In terms of the relative abundance of resonant neurons in their respective cortical layer we found that the ACo neurons that display strong resonance (i.e. with a $Q \geq 1.1$) where around 30%, a value that agree with the first description of these neurons presented in chapter 3.1 (Vera et al., 2014), and those recorded for the characterization of intrinsic properties and morphology presented in chapter 3.2 (Fig. 8C). Considering the 40% of neurons classified in the mixed group (M), which contains resonant neurons with $Q < 1.1$ and some misclassified non-resonant neurons, the whole proportion of resonant cells is less than a 70%. For their part, CA1 hippocampal neurons represent near 80% of layer II neurons (Amaral and Lavenex, 2007) and stellate resonant cells comprise a 65% of layer II entorhinal neurons (Klink and Alonso, 1997). In the case of stellate and CA1 neurons, the number given corresponds to neurons identified as belonging to that cell type. However, in the case of ACo neurons, that number is only based on Q value and

being possible that those resonant neurons correspond to different cell types, thus those numbers are not comparable.

Regarding their morphology and electrophysiological properties ACo neurons drastically break the idea of a general resonant cell type, showing a complete different set of features. Actually, considering the input-output curve, spike threshold and cell morphology, it was not possible to differentiate resonant from non-resonant ACo neurons (Figs. 9 and 12). Given that scenario we could not define ACo resonant neurons as a defined cell type, at least at the level that CA1 pyramidal and stellate cells do. The most remarkable difference of ACo resonant neurons is their lack of stereotyped cell morphology (Fig. 12), that in fact extends to all neurons from ACo. The absence of one archetypal cell morphology also applies to non-resonant neurons, showing that is not a particular feature of resonant cells.

Despite the fact that characterization of intrinsic and morphological properties of resonant neurons from ACo did not allow to define them as a particular cell type, they do show a differentiation from CA1 pyramidal neurons.

4.2 Resonant neurons translate their frequency preference to spiking regime using different mechanisms.

We found that resonant neurons from CA1 hippocampus and ACo are able to effectively translate their subthreshold frequency preference to a spiking regime, but using completely different mechanisms. Based on current- and voltage-clamp experiments, we propose that ACo neurons rely on I_h and I_{NaP} to filter low frequency

oscillations and reach action potential threshold at the preferred frequency (Figs. 3, 5A and 6).

In the case of hippocampal CA1 neurons we describe a complete different mechanism for selective spiking at the preferred frequency. Since these neurons have a low R_{in}, the amount of I_h recruited under moderate oscillations produces only a minor attenuation of membrane potential responses with a negligible filtering at potential near threshold. We found that these neurons have an intrinsic mechanism that controls their perithreshold behavior based on the relative contribution of I_{NaP} and I_M (Fig. 23 and 24). If I_{NaP} is larger than I_M, neurons are not selective for theta frequency stimulation and respond with higher firing probability at lower frequencies. However, if from the previous condition I_{NaP} is reduced or I_M is increased, CA1 pyramidal neurons that display non-resonant behavior can switch to an I_M-dependent resonant performance, displaying band-pass filtering properties at perithreshold potentials and thus affecting spiking probability.

These results show that these two types of resonant neurons do translate their frequency preference to spiking regime, but using completely different strategies, one based on I_h and the other on I_M.

4.3 The impact of theta-resonance under *in vivo*-like conditions and the effect of changes in R_{in}.

By means of an RLC circuit we showed that the variation in R_{in} of resonant neurons in the high-conductance state observed in an active brain should produce a modulation of neuronal resonance, changing the peak frequency, resonance strength and phase shift (Fig. 25). More important, the range of modulation matches the whole theta-frequency

range. Since in the equivalent RLC circuit the inductive branch represents any resonance-generating current, the prediction does not distinguish between the particular involved current, thus it is applicable to I_h-resonance that translate frequency selectivity to spiking in ACo neurons, and also to I_M-resonance involved in the switching perithreshold behavior of CA1 neurons. Generally speaking, the prediction of modulation of resonance applies to all forms of neuronal resonance.

We then corroborated the previous prediction for I_h-resonance of pyramidal neurons recorded at hyperpolarized potential. We confirmed the relationship between R_{in} and resonance, which indicates that the predicted modulatory phenomenon occurs in real neurons and that the range of modulation is significant, as for the RLC model.

Since this modulation occurs at expenses of a R_{in} drop, it follows that neurons with high R_{in} (as ACo neurons) will have a larger range for R_{in} variation and thus for changes in the resonant parameters, f_R, Q and Φ, compared to neurons that have lower R_{in} as CA1 neurons. For the same reason, it is expected that in ACo neurons the intrinsic frequency preference will have a higher functional impact than in hippocampal CA1 neurons.

Remarkably, the comparative approach that we used showed us that this categorization is true only at hyperpolarized potentials where I_{NaP} is not active (below -70 mV). When neurons are depolarized towards perithreshold potentials, the region of interest where the translation of frequency preference is expressed, the activation of I_{NaP} generates an amplifying effect, raising the impedance profile and its Q value. However, at least in the case of ACo and CA1 pyramidal neurons, there is an extraordinary difference in the magnitude of I_{NaP} conductance expressed at each neuron group. CA1 neurons, while

displaying lower R_{in}, have 5 times more I_{NaP} than ACo neurons, with the consequent increase of peak impedance from near 50 MΩ at -80 mV to near 200 MΩ at -65 mV (Fig. 21D, G). We speculate that the difference in R_{in} at ACo and CA1 pyramidal neurons is due to their respective neuronal size. The drop in R_{in} as a consequence of more membrane and more leak channels in larger neurons may also be accompanied by higher I_{NaP} (if considering the same channel density). In this way, we propose that I_{NaP} acts as a compensatory current for perithreshold excitability, busting impedance and increasing resonance strength in low I_{NaP} resonant neurons.

Chapter 5

CONCLUSION

Subthreshold neuronal resonance represents a mechanism of intrinsic frequency preference, which selectively translates subthreshold rhythmic fluctuations at the resonance frequency to a spiking regime. The intrinsic frequency preference is tunable according to the levels of synaptic activity; thus it can contribute to the propagation and stabilization of network rhythms.

References

Amaral D, Lavenex P (2007) Hippocampal neuroanatomy. In: The hippocampus book (Andersen P, Morris R, Amaral D, Bliss T, O'Keefe J, eds), pp 37–114. Oxford University Press.

Beck H, Yaari Y (2008) Plasticity of intrinsic neuronal properties in CNS disorders. Nat Rev Neurosci 9:357–369.

Bettencourt JC, Lillis KP, Stupin LR, White J (2008) Effects of imperfect dynamic clamp: computational and experimental results. J Neurosci Methods 169:282–289.

Boehlen A, Henneberger C, Heinemann U, Erchova I (2013) Contribution of near-threshold currents to intrinsic oscillatory activity in rat medial entorhinal cortex layer II stellate cells. J Neurophysiol 109:445–463.

Brown D (1988) M-currents: an update. Trends Neurosci 11:294–299.

Buzsáki G (2005) Theta rhythm of navigation: link between path integration and landmark navigation, episodic and semantic memory. Hippocampus 15:827–840.

Buzsáki G (2006) Rhythms of the Brain. Oxford University Press, USA.

Buzsáki G, Moser EI (2013) Memory, navigation and theta rhythm in the hippocampal-entorhinal system. Nat Neurosci 16:130–138.

Cang J, Isaacson JS (2003) In vivo whole-cell recording of odor-evoked synaptic transmission in the rat olfactory bulb. J Neurosci 23:4108–4116.

Canto CB, Wouterlood FG, Witter MP (2008) What does the anatomical organization of the entorhinal cortex tell us? Neural Plast 2008:381243.

Contreras D (2004) Electrophysiological classes of neocortical neurons. Neural Netw 17:633–646.

Creager B, Dunwiddiet T, Lynch G (1980) Paired-pulse and frequency facilitation in the CA1 region of the in vitro rat hippocampus. J Physiol:409–424.

Debanne D, Guerineau NC, Giihwiler BH, Thompson SM (1996) Paired-pulse facilitation and depression at unitary synapses in rat hippocampus: quantal fluctuation affects subsequent release. J Physiol 491:163–176.

Destexhe A, Rudolph M, Fellous JM, Sejnowski TJ (2001) Fluctuating synaptic conductances recreate in vivo-like activity in neocortical neurons. Neuroscience 107:13–24.

Destexhe A, Rudolph M, Pare D (2003) The high-conductance state of neocortical neurons in vivo. Nat Rev Neurosci 4:739–751.

Dorval AD, Christini DJ, White J (2001) Real-Time Linux Dynamic Clamp: A Fast and Flexible Way to Construct Virtual Ion Channels in Living Cells. Ann Biomed Eng 29:897–907.

Doucette W, Gire DH, Whitesell J, Carmean V, Lucero MT, Restrepo D (2011) Associative cortex features in the first olfactory brain relay station. Neuron 69:1176–1187.

Erchova I, Kreck G, Heinemann U, Herz a VM (2004) Dynamics of rat entorhinal cortex layer II and III cells: characteristics of membrane potential resonance at rest predict oscillation properties near threshold. J Physiol 560:89–110.

Ermentrout GB, Galán RF, Urban NN (2008) Reliability, synchrony and noise. Trends Neurosci 31:428–434.

Faisal A, Selen L, Wolpert DM (2008) Noise in the nervous system. Nat Rev Neurosci 9:292–303.

Fernandez FR, White J (2010) Gain control in CA1 pyramidal cells using changes in somatic conductance. J Neurosci 30:230–241.

Fyhn M, Molden S, Witter MP, Moser EI, Moser M-B (2004) Spatial representation in the entorhinal cortex. Science 305:1258–1264.

Hafting T, Fyhn M, Molden S, Moser M-B, Moser EI (2005) Microstructure of a spatial map in the entorhinal cortex. Nature 436:801–806.

Halliwell J, Adams P (1982) Voltage-clamp analysis of muscarinic excitation in hippocampal neurons. Brain Res 250:71–92.

Hasselmo ME (2005) What is the function of hippocampal theta rhythm?--Linking behavioral data to phasic properties of field potential and unit recording data. Hippocampus 15:936–949.

Hodgkin AL, Huxley AF (1952) A quantitative description of membrane current and its application to conduction and excitation in nerve. J Physiol 117:500–544.

Hu H, Vervaeke K, Graham LJ, Storm JF (2009) Complementary theta resonance filtering by two spatially segregated mechanisms in CA1 hippocampal pyramidal neurons. J Neurosci 29:14472–14483.

Hu H, Vervaeke K, Storm JF (2002) Two forms of electrical resonance at theta frequencies, generated by M-current, h-current and persistent Na^+ current in rat hippocampal pyramidal cells. J Physiol 545:783–805.

Huerta PT, Lisman JE (1995) Bidirectional synaptic plasticity induced by a single burst during cholinergic theta oscillation in CA1 in vitro. Neuron 15:1053–1063.

Hutcheon B, Yarom Y (2000) Resonance, oscillation and the intrinsic frequency preferences of neurons. Trends Neurosci 23:216–222.

Izhikevich EM (2002) Resonance and selective communication via bursts in neurons having subthreshold oscillations. Biosystems 67:95–102.

Kaczorowski C, Disterhoft J, Spruston N (2011) Stability and plasticity of intrinsic membrane properties in hippocampal CA1 pyramidal neurons: effects of internal anions. Society 3:799–818.

Kamondi A, Acsady L, Wang X-J, Buzsáki G (1998) Theta oscillations in somata and dendrites of hippocampal pyramidal cells in vivo: Activity-dependent phase-precession of action potentials. Hippocampus 261:244–261.

Kepecs A, Uchida N, Mainen ZF (2006) The sniff as a unit of olfactory processing. Chem Senses 31:167–179.

Kepecs A, Uchida N, Mainen ZF (2007) Rapid and Precise Control of Sniffing During Olfactory Discrimination in Rats. J Neurophysiol 98:205–213.

Klausberger T, Somogyi P (2008) Neuronal diversity and temporal dynamics: the unity of hippocampal circuit operations. Science 321:53–57.

Klink R, Alonso A (1997) Morphological characteristics of layer II projection neurons in the rat medial entorhinal cortex. Hippocampus 7:571–583.

Koch C (1984) Cable theory in neurons with active, linearized membranes. Biol Cybern 50:15–33.

Lisman J (2005) The theta/gamma discrete phase code occuring during the hippocampal phase precession may be a more general brain coding scheme. Hippocampus 15:913–922.

Llinás RR (1988) The intrinsic electrophysiological properties of mammalian neurons: insights into central nervous system function. Science 242:1654–1664.

Macrides F, Chorover SL (1972) Olfactory bulb units: activity correlated with inhalation cycles and odor quality. Science 175:84–87.

Macrides F, Eichenbaum H, Forbes W (1982) Temporal relationship between sniffing and the limbic rhythm during odor discrimination reversal learning. J Neurosci 2:1705–1717.

Mccormick DA (1998) Membrane properties and neurotransmitter action. In: Synaptic organization of the brain, 4th ed. (Shepherd GM, ed), pp 37–76. Oxford University Press, USA.

Narayanan R, Johnston D (2008) The h channel mediates location dependence and plasticity of intrinsic phase response in rat hippocampal neurons. J Neurosci 28:5846–5860.

Neher E (1992) Correction for liquid junction potentials in patch clamp experiments. Methods Enzymol 207:123–131.

O'Keefe J, Recce ML (1993) Phase relationship between hippocampal place units and the EEG theta rhythm. Hippocampus 3:317–330.

Penttonen M, Buzsáki G (2003) Natural logarithmic relationship between brain oscillators. 2:145–152.

Prescott S, Ratté S, De Koninck Y, Sejnowski TJ (2006) Nonlinear interaction between shunting and adaptation controls a switch between integration and coincidence detection in pyramidal neurons. J Neurosci 26:9084–9097.

Prescott S, Ratté S, De Koninck Y, Sejnowski TJ (2008) Pyramidal neurons switch from integrators in vitro to resonators under in vivo-like conditions. J Neurophysiol 100:3030–3042.

Ratté S, Hong S, De Schutter E, Prescott S a (2013) Impact of neuronal properties on network coding: roles of spike initiation dynamics and robust synchrony transfer. Neuron 78:758–772.

Richardson MJE, Brunel N, Hakim V (2008) From Subthreshold to Firing-Rate Resonance. 89:2538–2554.

Robinson RB, Siegelbaum S (2003) Hyperpolarization-activated cation currents: from molecules to physiological function. Annu Rev Physiol 65:453–480.

Sejnowski TJ (1995) Time for a New Neural Code? 376.

Shah MM, Mistry M, Marsh SJ, Brown DA, Delmas P (2002) Molecular correlates of the M-current in cultured rat hippocampal neurons. :29–37.

Somogyi P, Klausberger T (2005) Defined types of cortical interneurone structure space and spike timing in the hippocampus. J Physiol 562:9–26..

Sporns O (2011) Networks of the brain. MIT press.

Spruston N, McBain CJ (2007) Structural and functional properties of hippocampal neurons. In: The hippocampus book (Andersen P, Morris R, Amaral D, Bliss T, O'Keefe J, eds), pp 133–201. Oxford University Press.

Ulrich D (2002) Dendritic resonance in rat neocortical pyramidal cells. J Neurophysiol 87:2753–2759 Available at: http://www.ncbi.nlm.nih.gov/pubmed/12037177.

Vera J, Pezzoli M, Pereira U, Bacigalupo J, Sanhueza M (2014) Electrical Resonance in the θ Frequency Range in Olfactory Amygdala Neurons. PLoS One 9:e85826.

Vervaeke K, Hu H, Graham LJ, Storm JF (2006) Contrasting effects of the persistent Na+ current on neuronal excitability and spike timing. Neuron 49:257–270.

Von der Malsburg C, Phillips W, Singer W (2010) Dynamic coordination in the brain: From neurons to mind, 1st ed. MIT press.

Wang W-T, Wan Y-H, Zhu J-L, Lei G-S, Wang Y-Y, Zhang P, Hu S-J (2006) Theta-frequency membrane resonance and its ionic mechanisms in rat subicular pyramidal neurons. Neuroscience 140:45–55.

Wesson DW, Donahou TN, Johnson MO, Wachowiak M (2008) Sniffing behavior of mice during performance in odor-guided tasks. Chem Senses 33:581–596.

Wilson D (2001) Receptive fields in the rat piriform cortex. Chem Senses 26:577–584.

Xu J, Kang N, Jiang L, Nedergaard M, Kang J (2005) Activity-dependent long-term potentiation of intrinsic excitability in hippocampal CA1 pyramidal neurons. J Neurosci 25:1750–1760.

Supplementary figures

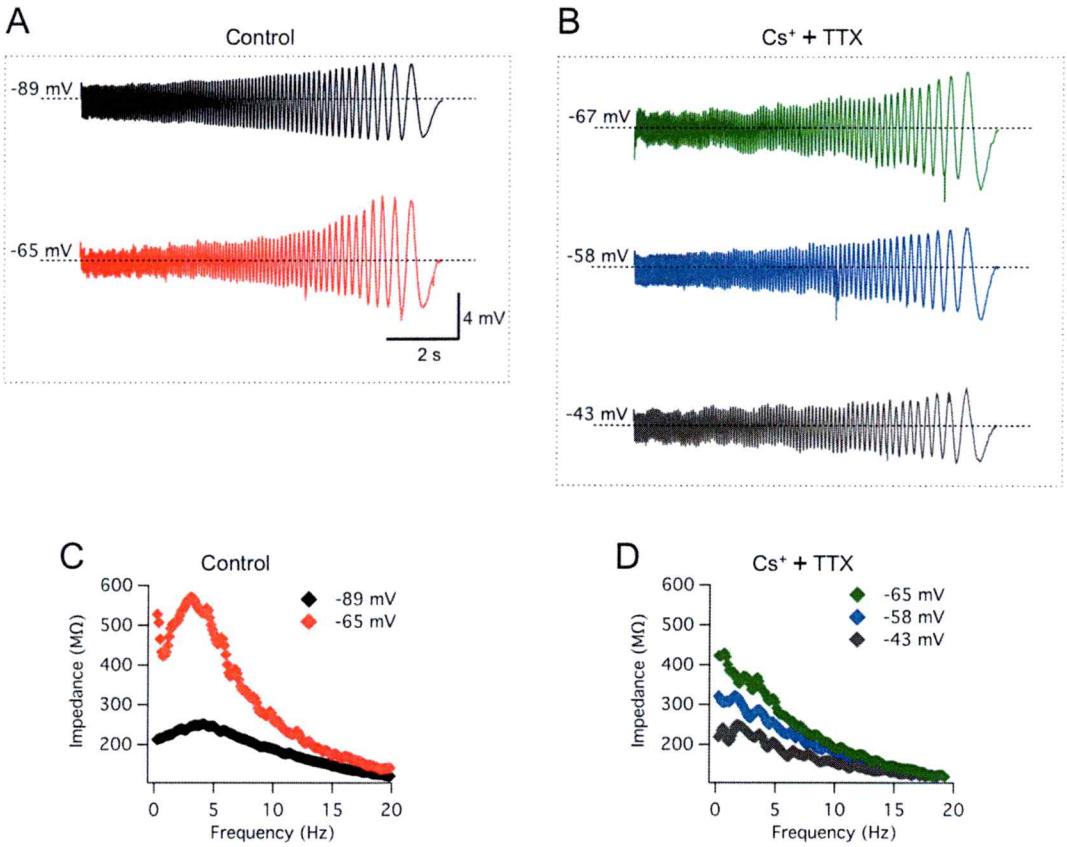

Figure S1. Blockade of Ih-resonance and spikes confirms the lack of the Im-dependent mechanism in an ACo neuron. A, ZAP-induced voltage traces at -89 and -65 mV in control conditions (Q and f_R are 1.2 at 3.7 Hz and 1.4 at 2.9 Hz, respectively). B, To evaluate the existence of Im-dependent resonance in this neuron, voltage traces were recorded in the presence of TTX (to block spikes) and Cs+ (4 mM; to eliminate Ih-dependent resonance). Subthreshold resonance was completely eliminated and it is absent even at -43 mV where I_M is supposed to be fully active (compare with Figure S2). C and D, impedance profiles for traces in A and B, respectively.

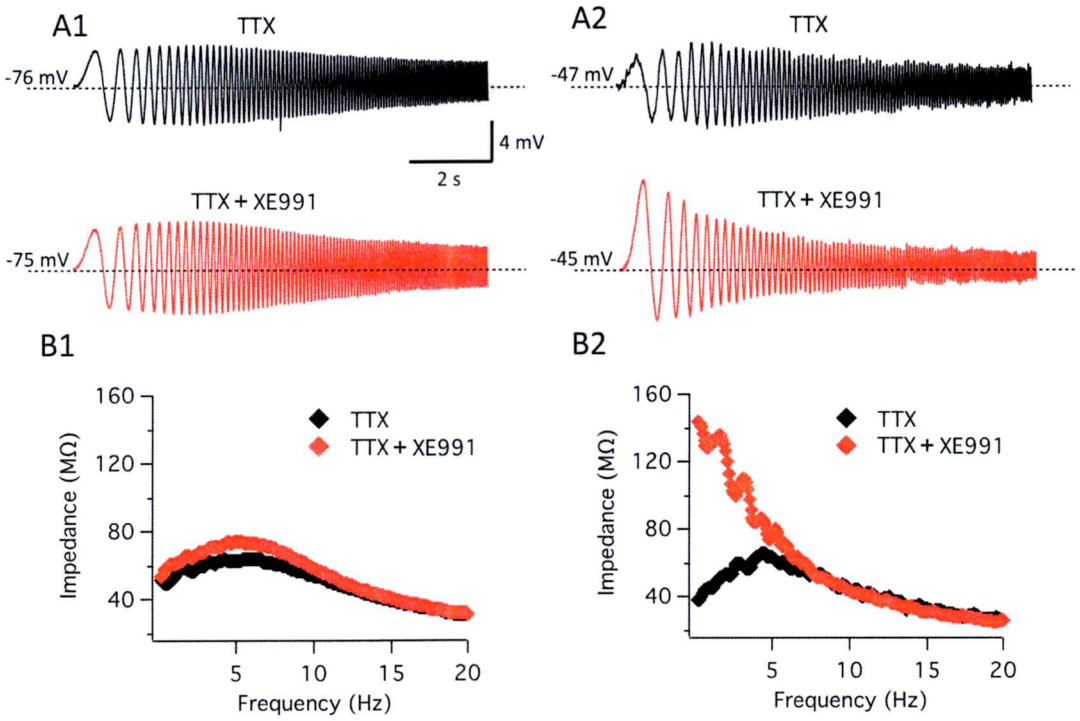

Figure S2. CA1 pyramidal neurons display at strong Im-dependent resonance at supra- threshold potentials in TTX. A, ZAP-induced voltage traces under TTX and after the application of 10 mM XE991 to block KCNQ channels, at -75 mV (A1) and at -45 mV (A2). B, impedance profiles for the recordings in (A) showing that resonance at this hyperpolarized potential is not affected by XE991 (B1). In contrast, at the suprathreshold potential (B2) application of the KCNQ blocker confirmed that resonance relies completely on Im at this voltage.

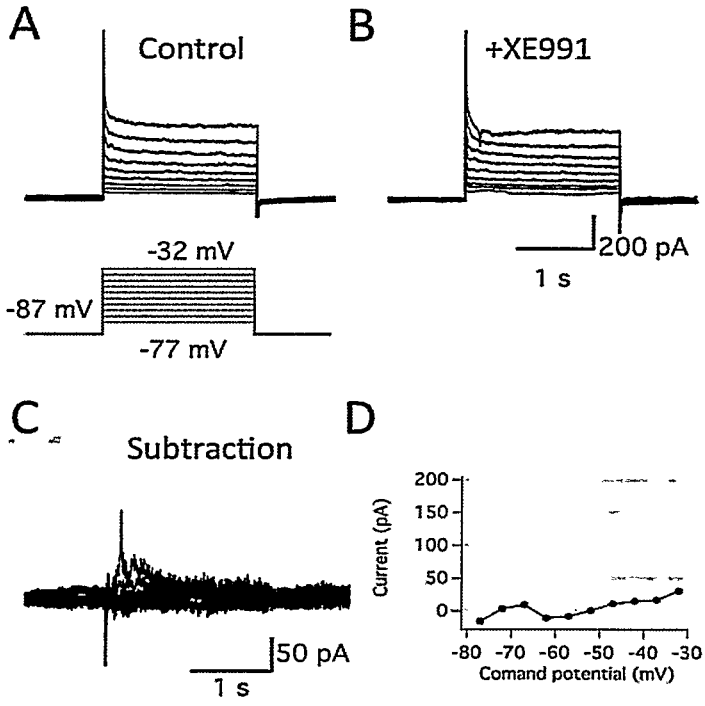

Figure S3. Protocol for I_M recording in ACo neuron gives no XE991 sensitive currents. A-B Voltage-clamp protocol consisted in a family of depolarizing voltage steps of 2 s of duration applied at control (A) and after the bath addition of 10 μM of XE991. C The subtraction of current in A and B reveal no XE991 sensitive current. D voltage vs current curve of traces isolated in C.

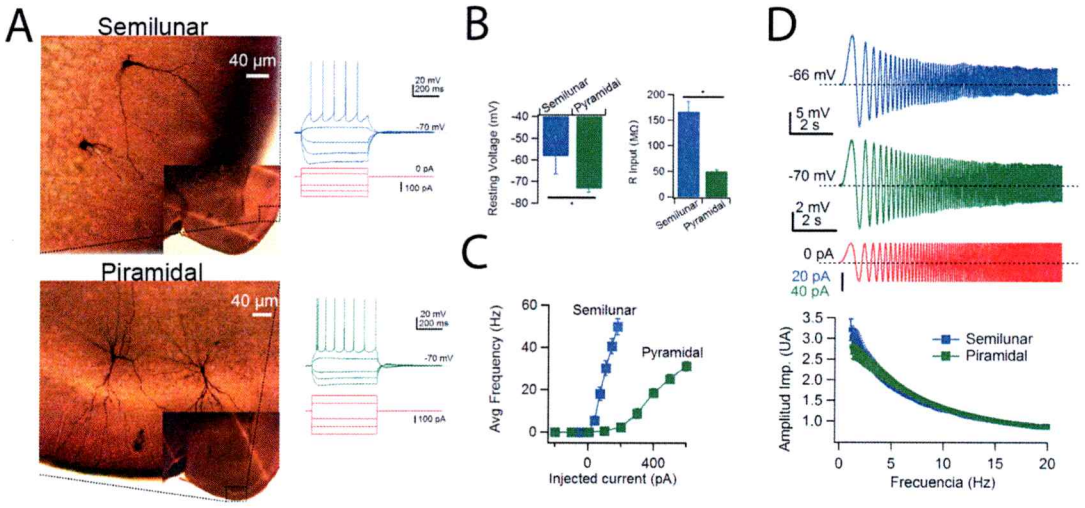

Figure S4. Exploration of resonance in confirmed semilunar and pyramidal neurons from piriform cortex. A Representative morphology of semilunar and pyramidal neurons from piriform cortex showing a typical voltage response under stimulation with squared current pulses. B-C Electrophysiological properties of each type of cell (n=10, avg ± sem). D Voltage responses under ZAP stimulation in each type of cell showing lack of frequency preference in their average impedance profile (n=10, avg ± sem).